Active Removal of Space Debris

Expanding foam application for active debris removal

Final Report

Authors: M. Andrenucci, P. Pergola, A. Ruggiero
Affiliation: University of Pisa - Aerospace Engineering Department - Italy

ACT researcher(s): J. Olympio, L. Summerer

Date: 21-02-2011

Contacts:

University of Pisa
Tel: +39-050-967211
Fax: +39-050-974094
e-mail: p.pergola@alta-space.com

Advanced Concepts Team
Tel: +31(0)715656227
Fax: +31(0)715658018
e-mail: act@esa.int

Available on the ACT website
http://www.esa.int/act

Ariadna ID: 10-6411
Ariadna study type: Standard
Contract Number: 4000101449/10/NL/CBi

TABLE OF CONTENTS

ABSTRACT

Controlling the amount of space debris is widely recognised as an important task to maintaining a sustainable space access for the decades to come. This is mainly due to the high risk of collisions that can easily invalidate both human and robotic mission. The topic is on the agenda of the Scientific and Technical Subcommittee and coordinated between space agencies in the Inter-Agency Space Debris Coordination Committee (www.iadc-online.org). Most current efforts focus on debris mitigation methods.

The Active Space Debris Removal System proposed in this study is based on an expanding foam system. The core idea of this method is to increase the area-to-mass ratio of these objects such that the atmospheric drag can cause their natural re-entry, thus "cleaning up" different regions in the near-Earth space. The drag augmentation system proposed does not require any docking system and just an uncontrolled re-entry can follow, thus it seems a short-term application free from the usual technological issues of these debris removal systems.

The drag augmentation is suggested to be performed exploiting the characteristics of the expanding foams that can nucleate almost spherical envelopes around the debris with very limited efforts of the spacecraft in charge that has the role to carry and spray the foam. Furthermore, the same method can also be conceived as a preventive system to be directly embedded in future space artificial satellites. The key technological aspect is the specific foam kind that has to be able, amongst other aspects, to significantly expand its original volume and has to be as light as possible.

This approach is demonstrated to be able to deorbit any kind of debris, but it has been proven to be particularly advantageous to deorbit up to 1 *ton* debris within 25 *years* from 900 *km*, of course the worst case. The actual scenario performance heavily depends on the specific foam considered and its characteristics. This study provides an approach to the drag augmentation methods identifying the foam ball radius assuring the best compromise between deorbiting time and impact probability for each debris. A brief review of the state of the art of foam technology for space and ground based applications is presented to frame the scenario into realistic perspectives. From this, a low order foam expansion model is developed and implemented in order to provide the relevant foam characteristics to the mission analysis section.

In this study, conservative assumptions, rather close to the state of the art of ground based foams, have been considered. Polymeric foams are chosen as the most suitable candidate to implement the proposed method. The expansion of this kind of foam is modelled considering the internal-external pressure difference and foam viscosity. The time evolution of the radius in a single-bubble model is derived and implemented for a set of external pressures up to vacuum conditions. The main outcome of this investigation are the foam expansion model and its density.

Assuming a density of 1 kg/m^3, the mission analysis section is implemented. A 5 *kW* Hall effect thruster is supposed to realize the transfers among different debris. Three debris lists covering a broad range of possible masses and initial altitudes are considered as set of targets to remove. The removal order is defined according to the minimum estimated low thrust velocity change to move from a debris to another in the list. In order to avoid assuming a precise mission starting date, a medium atmospheric density model is here used. It is a static model intended to be representative for long deorbiting times, like the ones resulting from many of the considered debris, where many solar cycles are completed. In this way the active removal missions designed are able to deorbit about 3 *tons* per year corresponding to several space debris.

Together with the mission analysis, also the system configuration of the spacecraft in charge is addressed with special emphasis to the foam nucleating and ejection system. The spacecraft is sized according to the performance of a medium class launcher (like Soyuz) into a Sun-synchronous orbit. Its initial mass is close to 5 *tons* where approximately 1 *ton* is allocated for the on board equipment. This dry mass is a-posteriori verified by a rough mass and power budget for all the main subsystems. The remaining mass is allocated for the electric thruster propellant and for the foam in different proportion according with the specific mission.

Some foam nucleating options are proposed both based on a single and on multiple spacecrafts. A decision matrix is implemented in order to select the most suitable candidate among these. A foam ejection nozzle is considered as the baseline solution and it is roughly sized according to existing static mixers.

Some assumptions are applied in order to obtain preliminary results about the plausibility and reliability of the proposed approach. These are mainly about debris mass, acceptable deorbiting time, suitable foam characteristics and reasonable general mission architecture. Finally, also the main hazards related with this scenario are outlined in order to sketch a rough estimation of the complete mission.

KEYWORDS: Space Debris, Expanding Foam, Passive Deorbiting Methods, Drag Augmentation Device

1 INTRODUCTION

Space debris are one of the main threats for an affordable and safe space exploration and exploitation. Space debris are mostly concentrated in the near-Earth space region, in particular in the Low Earth Orbit (LEO) and Geostationary Earth Orbit (GEO) regions. This waste is composed of spent boost stages, collision fragments, ISS construction material, human discards and so on [1].

Between 1957 and 2008, approximately 4600 launches have placed some 6000 satellites into orbit. Among these, about 400 were launched beyond Earth into interplanetary trajectories, but of the remaining ones only about 800 are operational. This means that roughly 85% of space objects belong to the uncontrolled satellite class, namely dead spacecrafts. To these, also launcher upper stages have to be added in order to have a rough idea of the large debris population. Furthermore, adding also smaller debris caused by explosions, fragmentations, collisions, accidental discharge and similar events, the whole debris population comprises millions of objects [2]. Space debris are not uniformly distributed on the whole space, indeed they move into the more common launch-target regions, in particular in the LEO and GEO regions, as shown in Fig. 1.

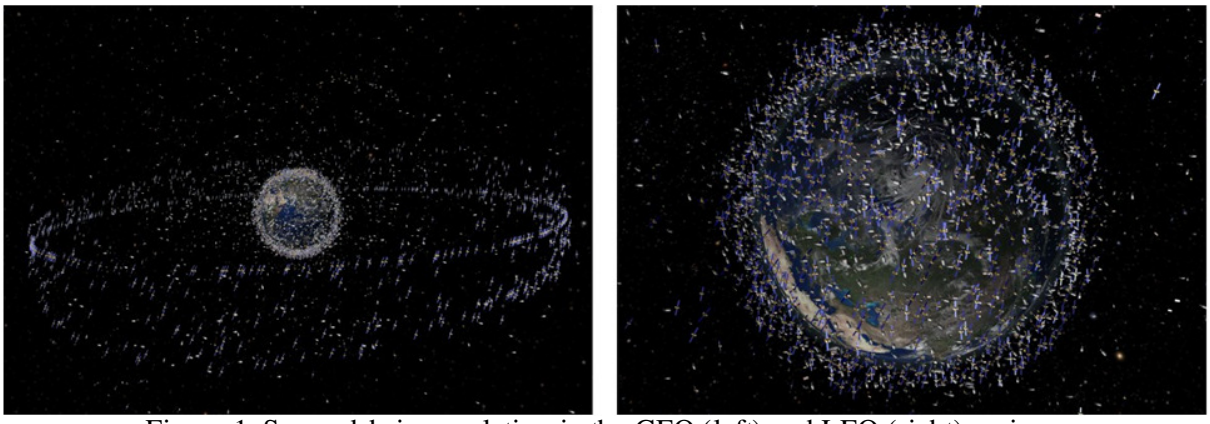

Figure 1: Space debris population in the GEO (left) and LEO (right) regions.

Taking into account also very small objects, there are, besides paint flakes (particles with size below 1e-4 *m*), at least three non-fragmentation debris sources deserving particular attention [3]. These sources put in space small particles, but due to the high relative velocities, the threat they represent in case of a possible impact, although not catastrophic, is however not negligible:

- More than 1000 solid rocket motors release micrometre-sized dust and *mm-/cm*-sized slag particles of aluminium oxide (Al_2O_3).
- At the end of operational life of the Russian RORSATs mission (Radar Ocean Reconnaissance Satellites) in the 1980s, droplets of coolant liquid (a low-melting sodium potassium alloy), used in the nuclear reactor cores, were released into space.
- Finally, also the release of thin copper wires from radio communication experiment during the MIDAS missions in the 1960s contributes to the increasing of these very small, but hazardous, particles [4].

It is worth stressing that these objects are too small to be deorbited with the conceived foam-based method assessed in this study.

It is estimated that approximately 50% of all traceable objects are due to in-orbit explosions or collisions [4]. Moreover, only statistical break-up models are available for these events and the

actual debris resulting from such an event can cover a quite spread region. The threat represented by these objects is further increased by their high velocities. Up to 52000 *km/h* can be reached and at this velocity even a nail could cause significant damages, even catastrophic, to operation satellites.

To give an idea of the threat represented by space debris, it is sufficient to think that the ISS has to perform occasionally collision avoidance manoeuvres and over 80 windows of the Space Shuttle had been replaced during the program lifetime.

1.1 Active Debris Removal

Recent studies demonstrated that the problem of space debris is slowly becoming more and more important for future use of the outer space [5]. Many simulations suggest that the number of objects in orbit might grow, even when no further objects are added to space, due to collisions caused by fragments generated by other collisions [5,6,7]. This *collisional cascading* may potentially lead to a chain reaction situation, with no further possibility of human intervention and with a substantial increase of the hazard level for space operations [8].

This feedback collision effect has been highlighted for the first time in 1978 by Kessler and Cour-Palais [9] and has become popular as *Kessler syndrome* even without ever having had a strict definition. Recently, Kessler itself has concluded that there is little doubt that the so called *Kessler syndrome* is a significant source of future debris, stressing at the same time that, even if the growth of orbital debris has slowed, still we are not capable of preventing the growth in the debris population from random collisions [10].

Figure 2 [11] shows the catalogued population of object in space in the last 54 *years*. It can be noticed the high presence of fragmentation debris, compared to the number of spacecrafts or rocket bodies. In fact, several studies found that "derelict spacecraft and orbital stages now outnumber active spacecrafts by more than 5 to 1" [8].

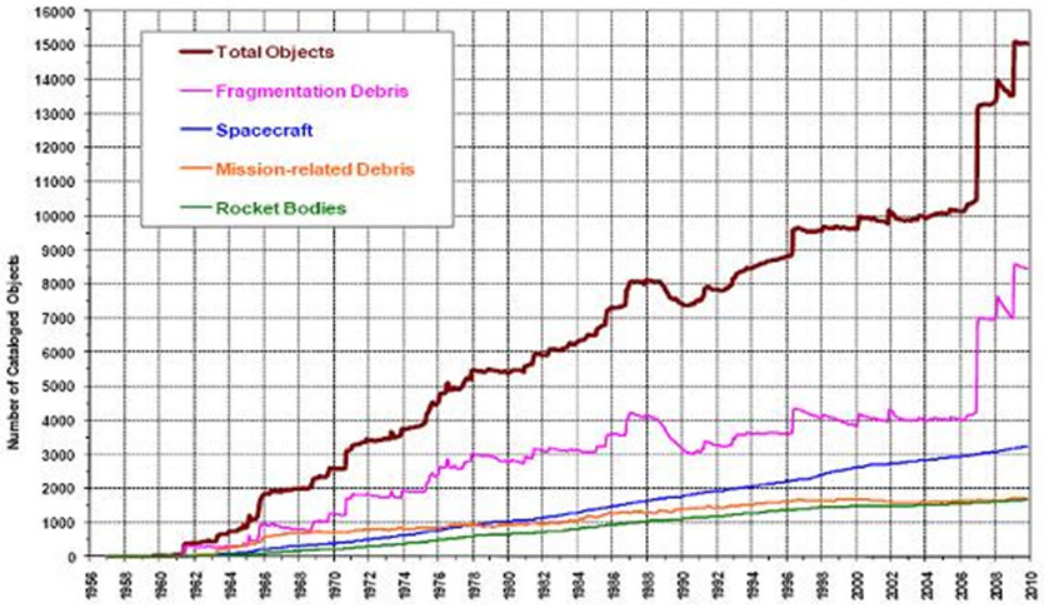

Figure 2: Number of catalogued manmade objects in space over the last 54 years [11].

It is possible to classify the growth evolution into three main phases [11]:

- 1960-1996 during which the growth is almost linear at a rate of 260 debris per years,
- 1996-2006 during which the growth is still almost linear, probably due to implementation of debris mitigation guidelines,
- 2006-2010 during which two impact events created more than 1250 debris per year.

At this point even an almost full compliance with IADC (Inter-Agency Space Debris Coordinating Committee) Guidelines [12] should not be sufficient forcing space agencies to agree about the retrieval of a number of objects that are already in orbit. In order to solve this problem, a number of active debris removal concepts have been described, such as: electromagnetic methods, momentum exchange methods, remote methods, capture methods and modification of material properties or change of material state [13].

In order to face this situation, a good understanding of the orbital debris problem is binding. As a matter of fact, the distribution of the present debris in terms of mass and spatial density is an important factor to decide in which way their removal should be addressed. In order to estimate the population of debris, i.e. their position and physical characteristics, and to have an idea of the future environment, several modelling program were implemented in the 1970s [12]. The EVOLVE modelling series [12] is the first of its kind exploiting Monte Carlo processing to estimate future fragmentations. Furthermore, EVOLVE models include also useful classification for type of impact: intact-on-intact, intact-on-fragment, fragment-on-fragment.

Another model, implemented in the end of 80s, was the NASA90 [12] able to derive curve fits of debris environment. The principal characteristic of this model is that it can be implemented with semi-analytical relations, see Sec. 2. The last NASA series are LEGEND[12] and ORDEM [12]. The ORDEM96, besides implementing curve fit methods, is the first model able to characterize the debris population by altitude, eccentricity, inclination, and size.

The spatial density distribution for relevant debris is shown in Fig. 3 [14] at altitudes between LEO and GEO. It is possible to divide the spatial density in percentages. More than 70% of the objects, in fact, are in LEO, about 20% are in intermediate highly eccentric and Medium Earth Orbits (MEO from 12846 *km* to 33786 *km*) and less than 10% are in near-geostationary orbits [8]. It is estimated that the peak of spatial density of objects is in LEO, from 500 up to 2000 *km* of altitude. A second smaller peak is recognizable in the GEO region around 36000 *km* altitude.

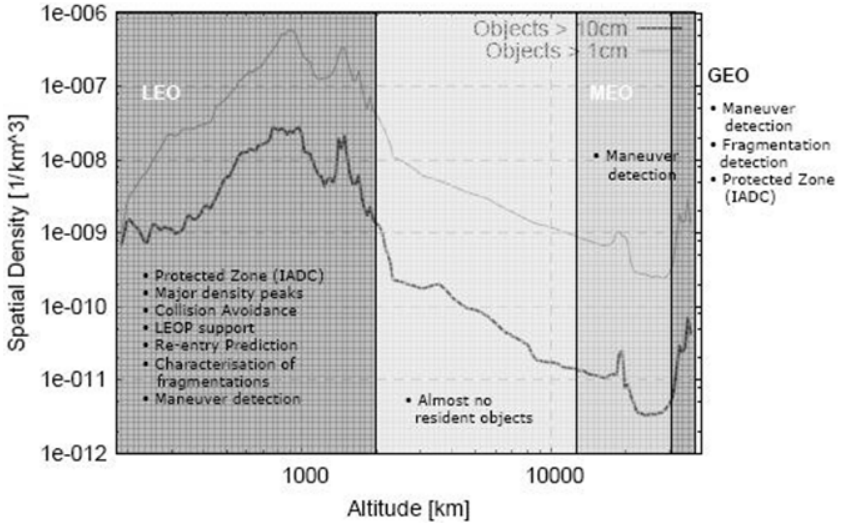

Figure 3: Debris spatial density at different altitudes [14].

More in detail, as we can notice in Fig. 3, there are two significant peaks in LEO at altitudes of 800-1000 *km*, and around 1400 *km*. Furthermore, peaks in the latitude distribution can be observed between 65 and 82 *deg* [2]. In the LEO region, the probability of collision with traceable debris, according to NASA ORDEM model, is 8e-3 per year for a satellite with 10 m^2 cross-section. This relatively high probability is due to the high debris density and their significant average velocities.

The probability of collisions in GEO, instead, is smaller, between 3e-6 and 3e-7. This smaller probability is due to the limited number of the debris, their large spatial distribution and the lower average relative velocities. In GEO there are many critical and commercial payloads, generally larger and more expensive than LEO satellites. This region is much harder to access than the LEO one and there are not energy dissipating orbital perturbations, like atmospheric drag. For this reason, there is a high priority to remove debris in GEO. It is since now worth mentioning, however, that the proposed method rely on the drag augmentation idea, thus it can not be applied in the GEO region.

An object can be tracked only if its size is larger than a given threshold. In order to define this threshold it is possible to classify space debris in three categories: small, medium and large. Debris less than 5 *mm* are catalogued as small and are considered non-traceable, debris between 5 *mm* and 10 *cm* are medium, again non-traceable and debris larger than 10 *cm* are catalogued as large. The large debris are usually traceable [11]. In Tab. 1 the number and the dangerousness of space debris tracked in LEO is summarized [11]:

Size	Number in orbit	Traceable	Lethal to Operational Spacecraft	Produces lethal fragment after impact
Small	Millions	No	(Usually) Not	No
Medium	~ 500000	No	Usually	Maybe
Large	~ 21000	Yes	(Almost) Always	Yes (1e2-1e4)

Table 1 : Number and dangerousness for categories of debris according to their size[11].

The hazard of catastrophic impacts depends not only from the debris size, but also by many other factors, like the average velocity or the relative size. To evaluate if a possible collision might result catastrophic or not, it is possible to consider the parameter EMS, the energy mass ratio[14,7,8]:

$$EMS = \frac{M_p v_{imp}^2}{M_t} \tag{1}$$

Here M_p is the mass of the debris, M_t the one of the target and v_{imp} is the impact velocity. When $EMS \geq 40\ kJ/kg$ the collision is considered a catastrophic event.

It is clear that an impact with a large debris creates a great number of other debris. With this regard, there are at least two significant examples to be mentioned. The Chinese *Fengyun 1C* satellite was destroyed in an ASAT test on January 11, 2007, generating about 2500 fragments of which 2300 were still orbiting 2 years later [8]. Moreover on February 10, 2009 the collision between *Iridium 33* and *Cosmos 2251* generated more than 1200 objects in a large area of LEO [8].

As previously said, according to the Kessler syndrome, the number of debris is doomed to grow. This occurs especially in the LEO region, which has the highest spatial density of debris objects, if no active measures are taken. By an analysis of catastrophic collision probability, Bastida and Krag picked up some regions as the more interesting candidates for active removal missions [7]:

- At $h=1000\pm100$ *km,* $i=82\pm1$ *deg* there are 290 objects that need to be removed, this is the region with the largest probability of catastrophic collisions.
- At $h=800\pm100$ *km,* $i=99\pm1$ *deg* there are 140 dangerous objects.
- At $h=850\pm100$ *km,* $i=71\pm1$ *deg* instead, there are 40 debris which have a high cross section and a high mass.

In this catastrophic scenario, it is clear that active removal is a necessary way to control and reduce debris growth, in order to permit easier future space activities.

1.2 Foam-Based Method

The problem of the active debris removal of space debris has to be approached facing with the enormous quantity of debris and with their various nature in terms of size, shape and kind (e.g. upper stages, telecommunication satellites, and so on). Any approach can be intuitively classified into one of the three following different strategies of debris removal:

- *One-to-one*: each debris, regardless of its size, has to be targeted and removed. Thus, a deorbiting platform has to be developed, manufactured and launched for each single debris to deorbit.
- *One-to-many*: the chosen strategy is autonomously capable to target and remove several debris. These could be of just one kind or of multiple kinds and sizes.
- *One-to-any*: the chosen method affects any object in a given orbit. To this category belong those methods that rely on global physical factors or uncontrollable deorbiting strategies.

Each one of these three strategies can be supported presenting their pros and cons but, as a matter of fact, the second one represents the most viable option. Indeed, a strategy aimed to target each one of the millions of debris represents a huge task in terms of time and technical requirements. By means of this kind of approach only the larger/heavier debris can be targeted in order to avoid having more costs than benefits. On the other hand, a strategy whose main effect is to decrease the lifetime of any orbiting object could be even more dangerous for all manmade spacecrafts, than for debris themselves. In this case there would be hundreds of active satellites forced to realize displacement manoeuvres to avoid the effects of one of these global affecting methods.

Therefore, the conceived debris removal system has been identified within the one-to-many category. In this category already several methods have been proposed. The main ones are: electromagnetic methods, capture with net-like systems, momentum exchange methods, ground based methods, modification of material properties or change of material state.

The proposed scenario belongs to the field of the momentum exchange methods, and in particular it can be thought as a drag augmentation system. The proposed system tends to define a reliable and easy way to perform this drag augmentation. The core idea is to develop a platform able to realize a foam ball around a target debris that enlarges its area-to-mass ratio such that the atmospheric drag can exert a significant influence to decelerate the debris. In this way, debris that would have orbited for hundreds of years, will re-entry in a prescribed time. The most remarkable advantages of this method are:

- A docking mechanism is not required, thus all the technological issues related and all the potential hazards deriving from the docking with a non-cooperative debris do not apply.
- The resulting foam structure does not require any control during the re-entry. Since the foam will ideally expand isotropically in the space (vacuum and microgravity conditions) [15,16], resulting in a spherical form presenting always the same cross section, an uncontrolled re-entry (no thruster and a limited ground segment) can take place.
- The resulting foam structure around the debris is much sturdier than any tether, sail or net-based structure.
- The momentum exchange is given only by the drag force decelerating the debris until it burns completely up in the atmosphere.
- There are no potential hazards related to ground based systems, e.g. lasers passing through the atmosphere (although other kind of hazards might exist, see Sec. 11).

The reliability of a foam-based strategy relies on the absence of control during the deorbiting time and the absence of any potential impact damage. The resulting object can be thought as a ball that offers always the same cross section; it contains in itself the target debris and can be nucleated also at a distance from the deorbiting platform. Furthermore, as already stressed, the absence of any docking system and close approaches reduce the key technology to the specific foam employed.

If compared to other drag augmentation methods, a foam ball offers several advantages. First of all, it is not exposed to impact damages that could prejudice the goal of the whole mission. For instance, let us think to a sail: it realizes the same drag augmentation (and, from a purely area-to-mass ratio point of view, also more advantageous), but it is very likely that it will impact something during the re-entry that can tear the sail off, thus compromising the mission. Moreover, another significant advantage is that an almost spherical form does not require any particular attitude control, while a sail-shaped object works at its best only in some configurations that should be actively maintained. As drawbacks of this method, instead, a difficult foam nucleation, incomplete attaching or not complete expansion in vacuum have to be mentioned; phenomena that could limit the foam-based method performance.

By way of example, for this methods' potential, it is possible to choose an arbitrary upper limit for the deorbiting time. Accordingly with the IADC Guidelines it can be assumed that, after the foaming process, the debris have to re-enter within 25 *years*. Although this is the prescribed time since end of operations recommended to be considered for future space objects, for an active debris removal mission, this period is here evaluated since the mission takes care of specific debris. Figure 4 shows, on a logarithmic scale, the deorbiting time as a function of the area-to-mass ratio for different values of the initial altitude.

The atmospheric model, however required to compute this deorbiting time, is based on average values as described by the *Medium Density* model in Sec. 2.2.

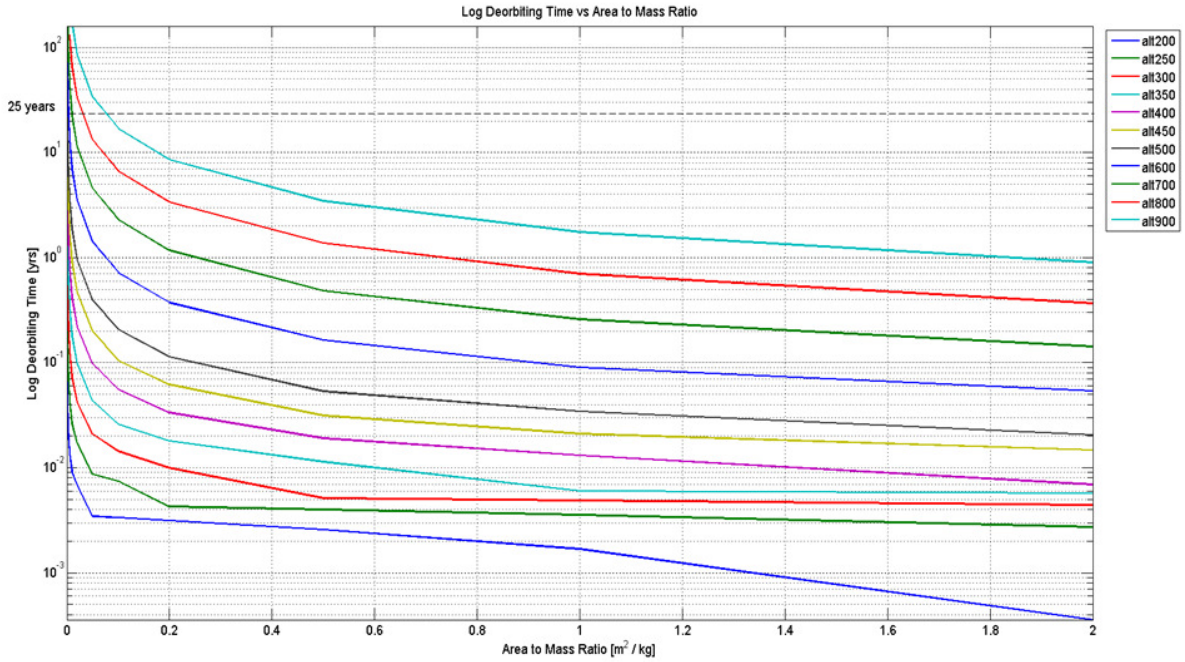

Figure 4: Deorbiting time (logarithmic scale) vs. area-to-mass ratio for different initial altitude values.

From Fig. 4, it results that an area-to-mass ratio larger than 0.07 is required at 900 *km* of altitude (see the close up of Fig. 5). For lower values, regardless of the specific debris mass and area, the re-entry time exceeds this threshold.

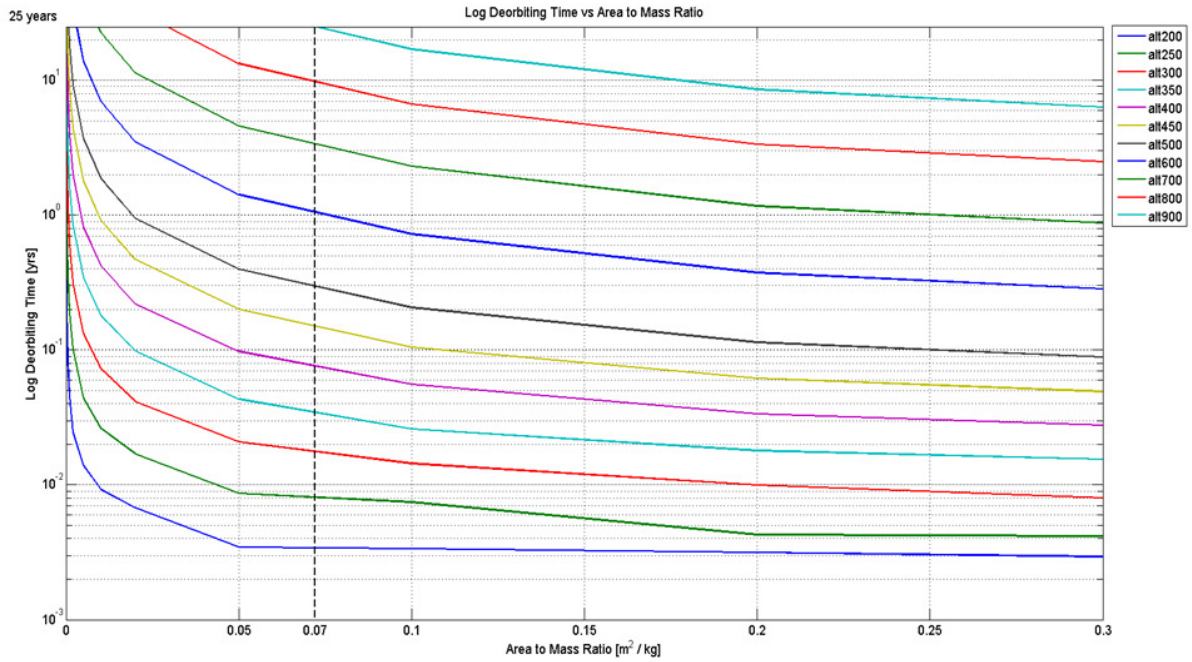

Figure 5: Close up of the deorbiting time [1e-3, 25 *years*] vs. area-to-mass ratio [0, 0.3].

Nevertheless, the value of the area-to-mass ratio is not enough meaningful as it can result in extremely high areas depending on the debris mass. For instance, let us think to a typical upper

stage of a launcher, it weights some 800 *kg*, thus an area-to-mass ratio equal to 1.5 would mean that we have to produce a foam ball cross section of 1200 m^2, i.e. a radius of 20 *m*, value here considered not really realistic.

For this reason, it is interesting to observe the actual area value for different masses and for several area-to-mass values. This is represented in Fig. 6, where an upper limit of about 314 m^2, which means 10 *m* radius, has been assumed. This value represents a sort of assumption and it reflects the idea to design a realistic methodology even in quite conservative cases. Higher area values could still be realized (and the general performance of the scenario would be better) but could require too much time to nucleate, and so they may be considered not suitable.

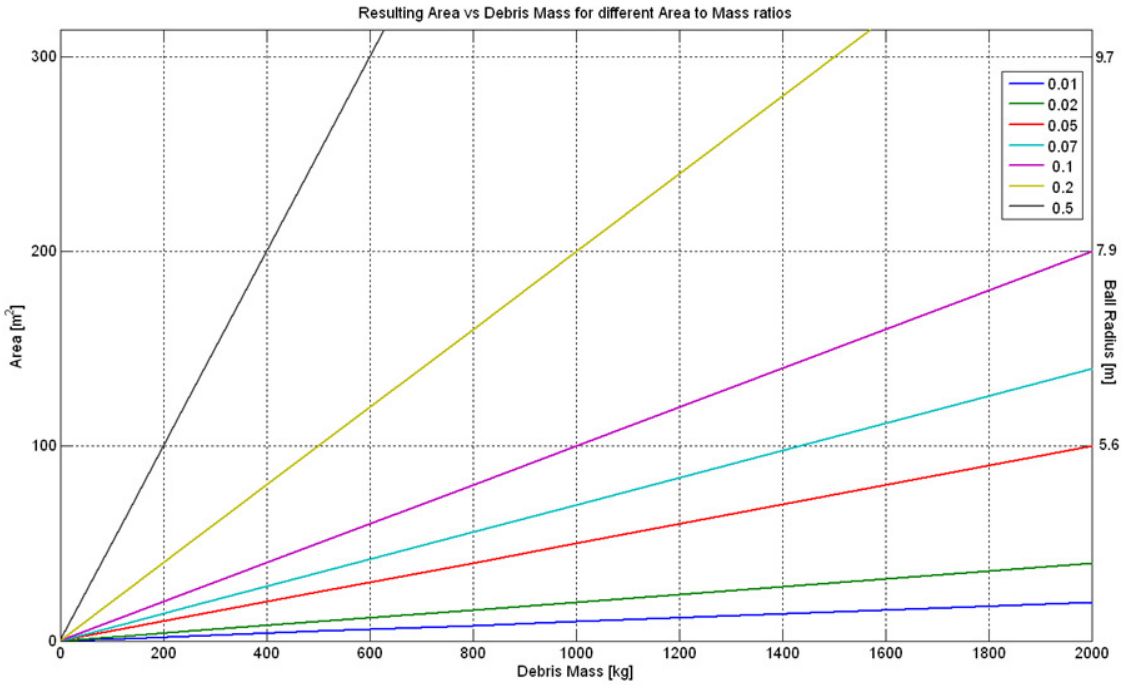

Figure 6: Debris mass vs. area for several area-to-mass ratio values.

As we are assuming that the foam will produce a ball-like structure, a given area represents a fixed value of the radius of this ball, represented in the rightmost vertical axis of Figure 6. Moreover, we stress that, also considering these reduced characteristics, appealing performances can be achieved by this methodology.

Thus, also the upper limit on the area can be estimated. Once this specific area-to-mass ratio has been fixed, Fig. 6 gives the maximum area that we have to produce such that a massive (2000 *kg*) debris re-entry within 25 *years* from 900 *km* of altitude. This value is 140 m^2, corresponding to 6.7 *m* of ball radius. Considering, by way of example, the same value for the area-to-mass ratio (0.07), a 1000 *kg* debris with an initial orbital altitude of 800 *km*, should deorbit within 10 *years* with a foam ball area of 70 m^2 and then 4.7 *m* of foam ball radius. For the same debris, considering a deorbiting time of 25 *years*, a smaller value for the area-to-mass ratio can be assumed (0.03) and thus a smaller foam ball area (30 m^2) and radius (3.1 *m*).

Better results in terms of re-entry time can be, however, obtained in the case of small mass debris. Indeed, in these cases, higher area-to-mass values can be targeted, resulting in shorter deorbiting times. For instance, considering the same 6.7 *m* sphere, 300 *kg* debris can be deorbited in approximately 3 *years*, as an area-to-mass value up to 0.5 can be achieved. It is worth saying that

this analysis has been carried out neglecting the mass of the foam and that more conservative results are shown in Sec. 4.

1.3 Mission Scenario

The above described method can be thought as composed of different phases. Actually these are the complete mission scenario phases:

a) *Launch*: The platform in charge of targeting and deorbiting the debris has to be launched into an initial orbit. The most suitable choice for the launch orbit of the spacecraft is the one of a specific debris, see Sec. 10. The platform has just to perform the final approach manoeuvre to reach the first target debris.

b) *Target Debris Interception*: This phase consists in a set of orbital manoeuvres aimed at the acquisition of the same orbital elements of the target debris, i.e. debris rendezvous.

c) *Foaming process*: In this phase the target debris has been reached and the actual foaming process takes place. During this stage the foam has to:

1. be ejected from the platform and reach the target debris (see Sec. 9)
2. stick to the debris surface
3. grow in volume (see Sec. 6)
4. cover the targeted debris

d) *Debris Deorbiting*: The debris is now contained within the foam and the natural deorbiting of the system begins.

e) *Targeting of next debris*: The platform can now target another debris operating its (electric) thrusters to reach a new interception orbit.

f) *Platform self-disposal*: Once the platform has completed its mission, the thrusters can be finally used to lower the orbit perigee to deorbit the spacecraft within the 25 *years* limit, as stated by the IADC guidelines.

Figure 7 shows the most important phases of the mission: target debris interception, the foaming process and debris deorbiting.

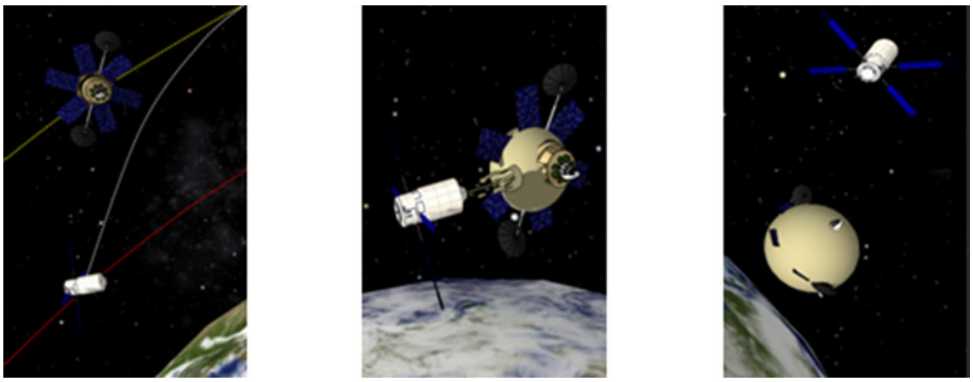

Figure 7: Representation of the proposed method: target debris interception (left), foaming process (center), debris deorbiting (right).

2 SPACE ENVIRONMENT MODELS

Before starting the analysis of the proposed foam-based method, it is mandatory to provide methodologies to compute the behaviour of the deorbiting object. In particular, in this chapter some models, required to assess the deorbiting time and the impact probability, are provided. Since the specific atmospheric model is of fundamental importance to estimate the deorbiting time, the specific one here considered has been chosen as it offers the chance to model different density regimes, from low to high. Moreover, considering only the atmospheric drag, it is clear that the larger the foamed debris, the better this scenario behaves. This does not hold anymore if also the impact probability is considered. The NASA90 impact probability model is here chosen, among several options (see Sec. 2.3), as it can be easily implemented without relying on specific libraries. Furthermore, also the numerical methodology by which the deorbiting time is computed through the work is given.

2.1 Deorbiting Time Estimation

The estimation of the decay time for a generic orbiting body is a challenging problem due to the huge number of unknown quantities related to its orbit, shape and the actual atmospheric density. In order to obtain a fast and realistic assessment of the deorbiting times, some perturbation effects acting on the body may be neglected while the most important ones can be averaged over one or more orbital revolutions [17].

More in detail, let us consider the instantaneous acceleration vector of a generic body on an elliptical orbit around the Earth as the sum of the acceleration given by Newton gravity law [17] plus a perturbation component. This latter part changes along the orbit due to the different contributions of the various terms composing this acceleration as Sun and Moon third body acceleration, atmospheric drag, Earth non spherical gravitational field, solar radiation pressure and thruster acceleration [17]. As the typical orbital altitude of the objects we are targeting is between 500 *km* and 1000 *km*, it is possible to assume that the perturbation mainly affecting the body is the atmospheric drag, which can be expressed as [17]:

$$\vec{a}_{drag} = -\frac{1}{2}\rho C_d \frac{A}{m} V^2 \frac{\vec{V}}{\left|\vec{V}\right|} \tag{2}$$

where ρ is the atmospheric density value, C_d a dimensionless number reflecting the object configuration sensitivity to drag force, A and m respectively the object cross-sectional area and mass and V its relative velocity vector with respect to Earth atmosphere.

Considering a direct method, as the one described by P.H. Cowell in the early 20th century [18], the integration of this acceleration value for a very long time, as the one needed by an object to reach high density atmospheric layer burning out, could be very expensive in terms of computation time. An alternative for the solution of this problem is the implementation of the Encke's method [18] based on the assumption that the integrated variables are small and so it is expected to be the integration error. This method needs however a very careful rectification to avoid numerical instabilities or large loss of precision [19], thus nowadays it tends to be avoided. An additional valid alternative to model the perturbation effects is represented by the Gauss form of the Lagrange

Planetary Equations [20]. These equations model the time evolution of the classical orbital parameters (semi-major axis a, eccentricity e, inclination i, right ascension of the ascending node Ω, argument of pericenter ω and M_0 [$M_0 = M\text{-}n(t\text{-}t_0)$]) under the influence of a non-conservative perturbation. These read:

$$\begin{aligned}
\frac{da}{dt} &= \frac{2a^2}{h}\left\{e\sin(\nu)a_r + \frac{p}{r}a_\theta\right\} \\
\frac{de}{dt} &= \frac{1}{h}\left\{p\sin(\nu)a_r + \left((p+r)\cos(\nu)+re\right)a_\theta\right\} \\
\frac{di}{dt} &= \frac{r\cos(\omega+\nu)}{h}a_h \\
\frac{d\Omega}{dt} &= \frac{r\sin(\omega+\nu)}{h\sin(i)}a_h \\
\frac{d\omega}{dt} &= \frac{1}{he}\left\{-p\cos(\nu)a_r + (p+r)\sin(\nu)a_\theta\right\} - \frac{r\sin(\omega+\nu)\cos(i)}{h\sin(i)}a_h \\
\frac{dM_0}{dt} &= \frac{1}{na^2e}\left\{\left(p\cos(\nu)-2er\right)a_r - (p-r)\sin(\nu)a_\theta\right\}
\end{aligned} \tag{3}$$

where n is the orbital mean motion, p the semilatus rectum, and h the orbital angular momentum while the three different accelerations a_r, a_θ and a_h are respectively the perturbation acceleration along the radial direction, along the normal to the radius vector in the direction of motion (orthoradial) and along the angular momentum vector direction [20]. The three directions here described identify the radial, transverse and normal (*RSW*) reference frame in which Eqs.(3) are expressed [17].

Once again, the accurate numerical integration of these equations entails the same issues of the Cowell method but, averaging the resulting time derivative of the orbital elements over one or more orbital revolutions, it is possible to implement a fast and reliable technique for the estimation of deorbiting time.

In order to combine the first of Eqs.(3) with the atmospheric drag expression of Eq.(2), a transformation from the *RSW* reference frame to the tangential, normal, omega orbital frame (*NTW*) [17] is now necessary. This system is identified by the *T* axis, tangential to the orbit and aligned with the velocity vector, the *N* axis, normal to the velocity vector in the orbital plane, and the *W* axis, normal to the orbital plane.

After this reference frame change, the atmospheric drag, acting along the tangential direction, is considered the only non-zero acceleration component. Simplifying Eqs.(3), it is possible to find that inclination and right ascension of the ascending node (RAAN) do not change in time. Semi-major axis and eccentricity are, instead, the only two elements experiencing its secular influence (the argument of pericenter relation is periodic). Focusing on the semi-major axis change, the first of Eqs.(3), under these assumptions, reads [21]:

$$\frac{da}{dt} = -\rho\frac{C_d A}{m}V^2\left(\frac{\sqrt{1+e^2+2e\cos(\nu)}}{n\sqrt{1-e^2}}\right) \tag{4}$$

where C_d, ρ, A and m are the same symbols introduced in Eq.(2).

By means of some simple substitutions for the relative velocity and the true anomaly rate of change, it is now possible to obtain an expression for the instantaneous semi-major axis change due to the atmospheric drag with respect to true anomaly:

$$\frac{da}{d\nu} = -\rho \frac{C_d A a^2 \left(1+e^2+2e\cos(\nu)\right)^{3/2}}{m\left(1+e\cos(\nu)\right)^2} \tag{5}$$

then, since $\frac{da}{dE} = \frac{da}{d\nu}\frac{d\nu}{dE}$, this equation can be rewritten as [21]:

$$\frac{da}{dE} = -\rho \frac{C_d A a^2 \left(1+e\cos(E)\right)^{3/2}}{m\sqrt{\left(1-e\cos(E)\right)}} \tag{6}$$

where E is the eccentric anomaly. With a similar procedure, it is possible to obtain the instantaneous rate of change of eccentricity with respect to the eccentric anomaly [21].

$$\frac{de}{dE} = -\rho \frac{C_d A a}{m} \frac{\sqrt{1+e\cos(E)}}{\sqrt{1-e\cos(E)}}\left(1-e^2\right) \tag{7}$$

The simultaneous integration of Eqs. (6) and (7) has to be carried out numerically. This has been done through the adaptive Lobatto quadrature of the atmospheric force over the eccentric anomaly [22]. This quadrature is based on a four-points Gauss-Lobatto formula, i.e. a quadrature rule approximating a definite integral, by means of a weighted sum of function values at specified points within the domain of integration. Accordingly, a specific model for the atmospheric density variation with the orbital altitude, as described in the following section, is required for these integrations.

2.2 Atmospheric Models

A huge number of different atmospheric models is nowadays available for the characterization of the atmospheric density variation with orbital altitude. The development of these methods mainly relies on two approaches: the coupling into a single relation of conservation laws and atmospheric components models, and the exploitation of in-situ measurements and satellites observational data [17]. Figure 8 shows a schematic survey of some of the models developed over the years together with their source and development basis.

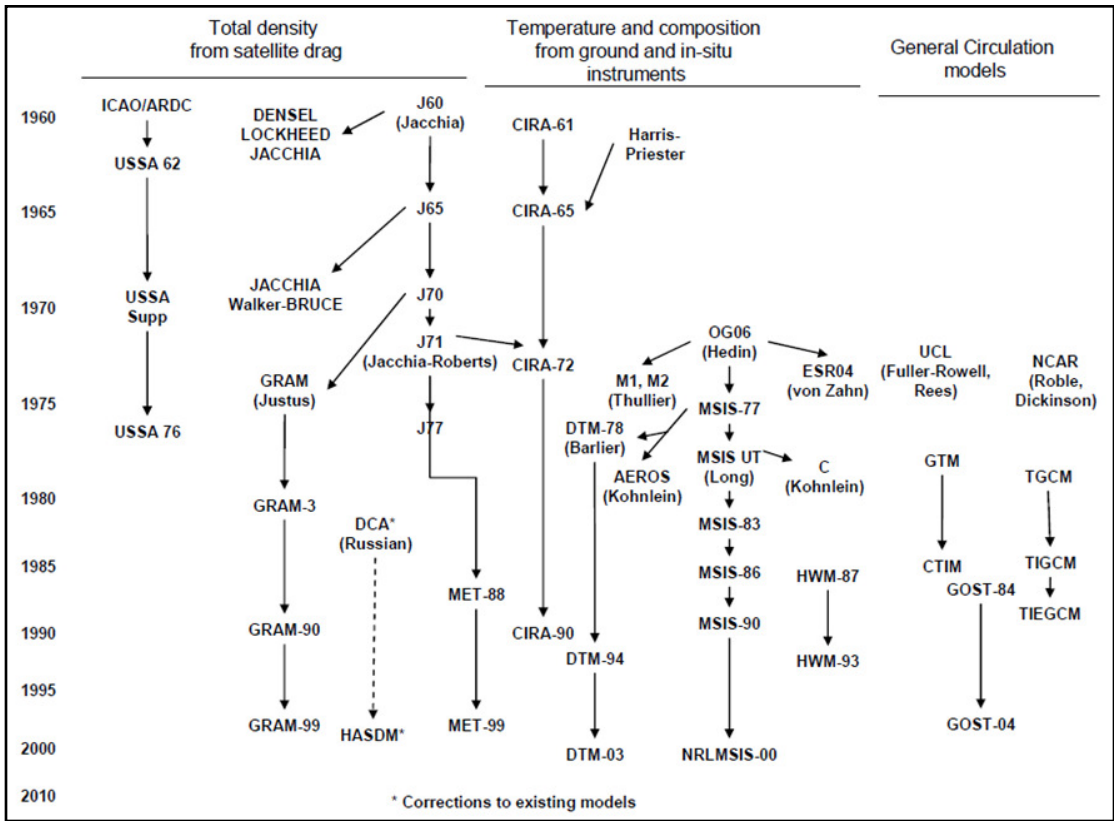

Figure 8: Atmospheric models evolution over the years with relative origin and derivation [23].

Nowadays, the most used models are: Standard Atmosphere (USSA76), Jacchia-Roberts with its various versions (J71, J77, GRAM-99), COSPAR International Reference Atmosphere (CIRA90) and Mass Spectrometer Incoherent Scatter (NRLMSIS-90) [23].

Some of these models present a static description of the atmosphere, with the density obtained as a function of the only orbital altitude, while many others, like the Jacchia-Roberts model, are time-varying models with much higher computational requirements. These demanding calculations are due to the uncertainties related to the forecasted solar activity and the relatively high effect of this on the atmospheric density at different altitudes.

Since our preliminary analysis does not assume a specific mission scenario, neither in terms of beginning of the mission nor in terms of mission duration, it is more reasonable to assume a simple static model for the atmospheric density. One of the simplest static models is the Harris-Priester model [24, 17], which relies on a number of tables listing reference density values obtained from observational data within a complete solar cycle. Table 2 shows the values of the atmospheric density, in the minimum and maximum density case, used in our analyses for the implementation of the Harris-Priester model.

Altitude (*km*)	**Minimum Density (kg/m^3)**	**Maximum Density (kg/m^3)**	**Altitude (*km*)**	**Minimum Density (kg/m^3)**	**Maximum Density (kg/m^3)**
100	4,97E-07	4,97E-07	**420**	1,56E-12	5,68E-12
120	2,49E-08	2,49E-08	**440**	1,09E-12	4,36E-12
130	8,38E-09	8,71E-09	**460**	7,70E-13	3,36E-12
140	3,90E-09	4,06E-09	**480**	5,47E-13	2,61E-12

150	2,12E-09	2,22E-09	**500**	3,92E-13	2,04E-12
160	1,26E-09	1,34E-09	**520**	2,82E-13	1,61E-12
170	8,01E-10	8,76E-10	**540**	2,04E-13	1,27E-12
180	5,28E-10	6,01E-10	**560**	1,49E-13	1,01E-12
190	3,62E-10	4,30E-10	**580**	1,09E-13	8,00E-13
200	2,56E-10	3,16E-10	**600**	8,07E-14	6,39E-13
210	1,84E-10	2,40E-10	**620**	6,01E-14	5,12E-13
220	1,34E-10	1,85E-10	**640**	4,52E-14	4,12E-13
230	9,95E-11	1,46E-10	**660**	3,43E-14	3,33E-13
240	7,49E-11	1,16E-10	**680**	2,62E-14	2,69E-13
250	5,71E-11	9,31E-11	**700**	2,04E-14	2,19E-13
260	4,40E-11	7,56E-11	**720**	1,61E-14	1,78E-13
280	2,70E-11	5,10E-11	**760**	1,04E-14	1,19E-13
290	2,14E-11	4,23E-11	**780**	8,50E-15	9,78E-14
300	1,71E-11	3,53E-11	**800**	7,07E-15	8,06E-14
320	1,10E-11	2,51E-11	**840**	4,68E-15	5,74E-14
340	7,21E-12	1,82E-11	**880**	3,20E-15	4,21E-14
360	4,82E-12	1,34E-11	**920**	2,21E-15	3,13E-14
380	3,27E-12	9,96E-12	**960**	1,56E-15	2,36E-14
400	2,25E-12	7,49E-12	**1000**	1,15E-15	1,81E-14

Table 2: Data used for the implementation of the Harris-Priester atmospheric model [24].

According to [23], any atmospheric model has 10-15% of inherent accuracy, and a medium density model (as the CIRA-86 at mean atmospheric conditions, very close to the Harris-Priester model used in this study) has a root mean square accuracy of the order of ±10% [25]. This small lack in accuracy is well compensated by its high computational speed and, despite its limitations with respect to short and long period variations of density, this model has been selected to describe three different phases of the solar cycle, resulting in *Minimum Density*, *Medium Density* and *Maximum Density* scenarios. The medium one has been obtained as an average between the minimum and the maximum densities of Table 2.

In the following, these three different density scenarios have been used to assess the optimal foam ball radius (see Sec. 4) for the DISCOS list but, under the hypothesis of periodic and regular cyclical change of the solar flux [17], the best option for the starting of an active debris removal mission is a high solar flux period. Starting the removal mission during this period, indeed, the deorbiting phase of the foamed debris immediately starts at the highest possible rate. Then, over the years, the change in the solar flux should decrease this deorbiting speed but the time spent in orbit during maximum density and minimum density would always at least be equal. Actually, if the deorbiting time is not an integer multiple of the solar flux cycle, maximum density periods would outnumber minimum density ones. For this reason, the Harris-Priester medium density model, as the one used in [26] for first order estimations, should be considered as a more realistic, and possibly conservative, case.

As an example, the atmospheric density values predicted by this model have been also compared with a different static model, the Standard Atmosphere USSA76 [27], as shown in Fig. 9. This latter model always gives smaller atmospheric density values for orbital altitude above 370 *km*. Below this threshold the atmospheric density is rather high and the small time period spent by deorbiting objects below this altitude is a very small fraction of the whole deorbiting time. Thus, the resulting final orbital lifetimes should actually be less conservative than the ones provided by our model.

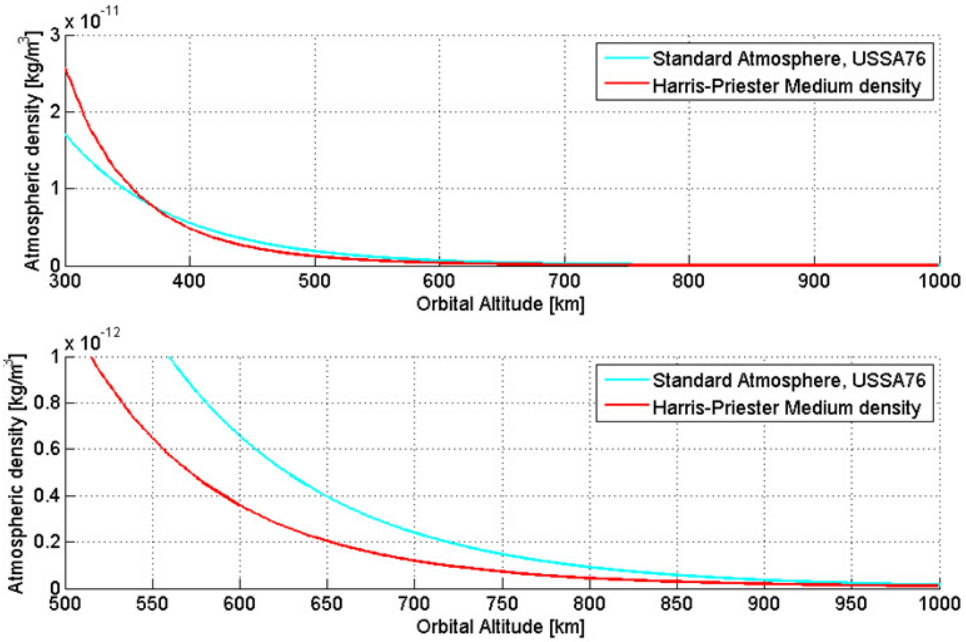

Figure 9: Comparison between the Harris-Priester model and the Standard Atmosphere USSA76 model. Below: a close up of the upper plot between 500 and 1000 *km* where the Harris-Priester model is more conservative.

For the sake of completeness, the lifetime values provided by the method described in Sec. 2.1 have been also compared with the plots, generated with the SatLife program, provided by [39]. These plots show two curves for a set of three ballistic coefficients. One of the curves, representing a deorbiting operation started during a solar minimum "when there will be a low level of decay" always predict, for altitudes below 700 *km*, orbital lifetimes longer than the others. Indeed, the curve corresponding to deorbitation begun at the start of a solar maximum "when the satellite will decay most rapidly for several years" provides shorter orbital lifetimes. The lifetime values predicted by our approach always lie between the two curves, thus it is reasonable to assume that the computed lifetimes represent reasonable assessments of the actual debris deorbiting time. By way of example, considering an object with a ballistic coefficient ($m\ A^{-1}\ Cd^{-1}$) of 200 starting from 500 *km* of altitude, our method predicts an orbital lifetime of 6.8 *years*, while the plots provide ~3 *years* (Orbit starting at solar maximum) and 7 years (Orbit starting at solar minimum) of lifetime. In this case, actually, we are closer to the most conservative case. For an object with a ballistic coefficient of 20 starting from 600 *km* of altitude, our code provides 2.65 *years* of lifetime as compared with ~1.5 to ~5 *years* given by the reference plot.

2.3 Space Debris Models

The assessment of impact probability for orbiting objects due to the proposed method and for the foam balls themselves is a binding task for the estimation both of hazards and risks related to the method (see Sec. 11) and of a suitable foam ball size (see Sec. 4). We only focus in the following on possible space debris impacts, neglecting those due to micrometeoroids. This is a rather reasonable assumption, since below 2000 *km* the orbital debris environment represents the major threat for space flight if compared with the meteoroid environment [28].

In order to obtain a representative estimation of potential impacts, over the years many space debris flux models have been implemented and refined, using data obtained from the post-flight analysis of spacecrafts as well as from observational data [29]. Some space debris environment models, together with their main characteristics, are listed below:

- NASA90 model (see Sec. 2.4) provides a simple and very fast debris flux calculation for orbital altitudes below 1000 *km*, but it does not take into account the existence of a large number of particles on eccentric orbits. Since this model has been the first more or less detailed description of the debris environment, it can not be really considered up to date [28]. In spite that, it remains one of the most valid options for preliminary analyses and impact probability estimations.
- ORDEM96 model, also known as NASA96, model is the successor of the NASA90 model. This model, unlike NASA90 model, basically identifies six different inclination domains and for each orbit performs a numerical collision analysis obtaining the spatial debris density around the target. Then the sum of the various contributions needs to be numerically converted to obtain the fluxes on the specific target orbit [30].
- ORDEM 2000 model is an evolution of the ORDEM96 model and it is suited for orbit regions between 200 and 2000 *km* of altitude. It relies on a completely different approach compared to the NASA90 and ORDEM96 (NASA96) models. It is based, indeed, on observational data and analytical techniques to obtain the debris population probability distribution functions. These functions then, from the debris environment, provide the presumed space debris flux [12].
- The MASTER 2001 model provides the debris population distribution, both for the past and the future, starting from the numerical modelling of all known fragmentation events as well as the generation of debris particles. The propagation of the particle orbits allows the flux calculation also considering the asymmetry induced by the particle orbits argument of perigee [31].
- The MASTER 2005 model is the successor of MASTER 2001 with some more refined and more updated features. Both the breakup and fragmentation models have been improved together with the update of some reference data as the reference population [31].

As already pointed out, since our analysis requires a fast and preliminary assessment of the space debris flux and the consequent impact probability, we identified the NASA90 model as the best one for our purposes. It is briefly described in the next section.

2.4 The NASA90 Model

The NASA90 model computes the debris flux F versus the impactor diameter d by means of an analytical formulation. The flux F is defined as the cumulative number of impacts on a spacecraft in circular orbit per square meter and year on the surface of an object randomly rotating around its centre of mass [32]. This value is obtained as function of the minimum impactor diameter d, the considered orbit altitude and inclination (h, i), the mission epoch and the solar radio flux S. It is obtained by means of [32]:

$$F(d,h,i,t,s) = H(d)\Phi(h,S)\Psi(i)\left[F_1(d)\,g_1(t,p) + F_2(d)\,g_2(t,p)\right] \tag{8}$$

In this equation, the first two terms may be obtained by means of:

$$\begin{aligned} H(d) &= \sqrt{10^{\exp\left[-(\log d - 0.78)^2 / 0.406\right]}} \\ \Phi(h,S) &= \Phi_1(h,S)\left(1+\Phi_1(h,S)\right)^{-1} \\ \Phi_1(h,S) &= 10^{(h/200 - S/140 - 1.5)} \end{aligned} \tag{9}$$

with d measured in *cm*, h in *km* and S in 10^4 *Jy*.

The terms in the square brackets also depend on the mission date, t, expressed in years, on the expected annual growth rate of mass in orbit, p, assumed by default equal to 0.05 [32] and on the growth rate of fragments, q, conservatively assumed 0.04 [32] for t>2011. These terms can be obtained by means of:

$$\begin{aligned} F_1(d) &= 1.22 \cdot 10^{-5} d^{-5/2} \\ F_2(d) &= 8.1 \cdot 10^{10} (d+700)^{-6} \\ g_1(t,q) &= (1+q)^{t-1988} \\ g_2(t,p) &= 1 + p(t-1988) \end{aligned} \tag{10}$$

The remaining term Ψ is the discrete inclination dependent function tabulated in Table 3 [32].

i (deg)	**≥28.5**	**30**	**40**	**50**	**60**	**70**	**80**	**90**	**100**	**≥120**
Ψ	0.91	0.92	0.96	1.02	1.09	1.26	1.71	1.37	1.78	1.18

Table 3: NASA90 inclination dependent function Ψ

The exact value of the Ψ term in Eq.(8) is obtained by the linear interpolation with respect to the orbital inclination.

The NASA90 model is exploited in Sec. 4 to obtain the foam ball impact probability as function of the foam ball size. The impact probability, of course, increases with the ball radius, thus increasing the risk of random collisions and the cascade effect. On the other hand, decreasing the ball radius, the deorbiting lifetime increases thus increasing the permanence in orbit and, accordingly, also the risk of additional collisions. The ball radius, indeed, is estimated considering the minimum of the curve given by the sum of these two contributions (see Sec. 4).

3 SPACE DEBRIS POPULATION

In general, the space debris environment, differently from the meteoroid one, is composed of man-made objects. Due to their origin, most of these debris have the following general properties [32]:

- their flight direction is almost parallel to Earth surface,
- different altitudes and inclinations suffer of different impact probabilities (see Sec. 2),
- the debris environment is in continuous time evolution (actually increasing in number),
- many of them have almost circular orbits.

This last characteristic is mainly due to the atmospheric drag that tends to decrease the orbital semi-major axis and reduces the orbital eccentricity [17].

The most hazardous debris are not simply the largest ones, but the risk they represent also heavily depends from their specific orbit and their orbital lifetime. Of course, the longer their lifetime, the larger the impact probability, thus the larger is the risk of further growth in the debris orbital population. Moreover, there are specific orbits, like Sun-synchronous Orbits (SSO) and GEO, more crowded than others, thus an uncontrolled object into one of these regions represents a significant threat for any operative satellite, eventually producing further debris. Of course, the lower the altitude of these objects, the later their removal should be addressed and the same holds for the ones with smaller cross-sectional areas. These two situations are the ones limiting the hazards from random collisions due to their generally short lifetimes.

The goal of this section is to present the set of debris lists considered in this study in order to assess the performance of the deorbiting scenario proposed. In the following, besides introducing the three debris lists here considered, also a possible ranking of their dangerousness, according to the previous considerations on impact probability and lifetime is presented. Finally, this section aims also to identify a suitable set of target debris for the proposed foam-based active debris removal system, intended as a class with a given range of physical characteristics and particularly hazardous orbits.

3.1 Space Debris Lists

Space debris lists rarely are open database and the exact number and nature of tracked objects is often covered by military intelligence. Space agencies and few other organizations worldwide have access to these lists and often reduced versions can be provided for research and educational purposes. In this study three lists are considered:

- ***Filtered DISCOS list***: This list is based on the ESA's DISCOS database. The Database and Information System Characterizing Objects in Space (DISCOS) is a reference source for launches, orbits and general mission descriptions of more than 33500 tracked objects [33]. The whole database includes more than 7.4 million orbit records in total, based on the US NORAD database. Furthermore, in the same database, the US Space Surveillance Network (SSN) constantly uploads orbital data of many tracked but unclassified objects. DISCOS can

be used by means of both standard database queries and automatic generation reports (ESA Register of Space Objects, ESA GEO Log, ESA Fragmentation Events Log) [33].

Based on this list, the ESA/ESOC orbital debris section, provided a filtered catalogue of space debris for this study. The list is composed of only 59 objects. These objects are the result of some sequential filters applied to the whole DISCOS list. It has been chosen, in this case, to query the database according to:

- latest orbital element, considering only objects with perigee altitude above 700 *km* and apogee altitude below 900 *km* (at November 2010). Furthermore, also the eccentricity has been limited to 0.001 and no filter on inclination has been applied.
- physical properties, considering only objects with an average cross sectional area larger than 1 m^2 and debris mass larger than 500 *kg*.
- launch date, considering only objects launched before 2000 and rocket bodies (regardless of the launch date).

Only one of the 78 *Iridium* satellites has been considered and it is worth saying that, as described in Sec. 10, this choice could lead to unfavourable results. Indeed, it gives an underperforming mission scenario as time and propellant mass required to move from one debris to the next depend on the distribution of debris considered. The exclusion of many satellites, one close the other, increases these figures, reducing the number of debris deorbited per year and accordingly the average mass.

The whole list of these objects resulting from the DISCOS database is summarized in Tab. 4. Here the average cross section (AREA, m^2), mass (MASS, *kg*), semi-major axis (SMA, *km*), eccentricity (ECC, -), inclination (INC, *deg*), right ascension of the ascending node (RAAN, *deg*), argument of perigee (ARGP, *deg*) are given. From these values also the area-to-mass ratio (A/M m^2/kg) and orbital altitude (ALT, *km*) are computed and shown in the two rightmost columns of Tab. 4.

AREA	MASS	SMA	ECC	INC	RAAN	ARGP	A/M	ALT
22,2521	661,05	7154,85946	0,000249	86,4002	334,7577	72,5434	0,033662	776,7225
6,4859	1753,22	7158,4684	0,0007	35,0457	93,339	188,8342	0,003699	780,3314
8,0062	693,76	7132,15619	0,000872	35,0427	196,5135	326,2027	0,01154	754,0192
6,4859	1994,05	7120,48238	0,000641	34,9942	105,1042	282,2124	0,003253	742,3454
3,7825	743,31	7089,46689	0,000906	74,0129	142,1734	278,2267	0,005089	711,3299
1,7732	743,31	7102,45595	0,000602	74,0374	305,1536	177,5348	0,002386	724,319
12,9182	1421,21	7129,12209	0,000881	74,0767	2,84	56,7027	0,00909	750,9851
5,8996	1486,62	7261,10941	0,000933	81,2613	226,1147	289,782	0,003968	882,9724
2,77587	508,42	7158,67772	0,000939	98,5047	74,4704	161,1933	0,00546	780,5407
21,1594	2279,48	7129,3094	0,000346	108,0085	183,1643	267,7558	0,009283	751,1724
1,7732	743,31	7158,92934	0,000998	74,0455	122,2159	299,3001	0,002386	780,7923
12,9182	1421,21	7156,56622	0,000471	74,0551	8,3423	358,0394	0,00909	778,4292
1,7732	743,31	7165,55188	0,000995	74,0376	166,856	289,8727	0,002386	787,4149
3,5466	744,3	7175,16019	0,000727	98,5979	82,246	309,454	0,004765	797,0232
7,0929	1923,69	7080,63475	0,000341	98,1922	320,4069	136,1987	0,003687	702,4978
3,0905	629,34	7146,7651	0,000212	108,0318	10,604	274,154	0,004911	768,6281
21,6139	2120,91	7221,95546	0,000277	70,9998	192,1498	132,006	0,010191	843,8185
33,4262	8225,97	7217,13615	0,000946	71,0023	167,7342	242,4867	0,004063	838,9992
3,0493	733,4	7265,16506	0,000844	99,0179	212,3947	267,3074	0,004158	887,0281

17,58611	3221,01	7228,00744	0,000799	70,9218	338,4874	157,6445	0,00546	849,8704
33,4262	8225,97	7215,39914	0,000349	71,0041	314,263	128,5404	0,004063	837,2621
17,58611	3221,01	7222,68014	0,000429	70,9958	211,4363	124,6571	0,00546	844,5431
12,9182	1421,21	7143,90393	0,000576	74,0401	280,8718	250,4652	0,00909	765,7669
3,5466	815,66	7182,83394	0,000649	98,9174	85,5927	10,4535	0,004348	804,6969
16,5395	2244,8	7256,72996	0,00084	98,9994	256,6304	316,0426	0,007368	878,593
17,58611	3221,01	7229,36405	0,000842	70,8729	213,2285	203,1169	0,00546	851,2271
33,4262	8225,97	7221,31003	0,000627	71,0215	357,6447	283,2526	0,004063	843,173
22,2825	1764,12	7139,28542	0,000396	98,6952	228,2633	94,3321	0,012631	761,1484
2,1508	796,83	7193,01723	9,09E-05	98,468	211,7472	85,0151	0,002699	814,8802
33,4262	8225,97	7220,63975	5,09E-05	70,9649	12,445	73,0759	0,004063	842,5028
12,9182	1421,21	7160,03654	0,000608	74,0281	136,4772	224,1406	0,00909	781,8995
19,2788	2493,56	7162,38209	8,02E-05	98,5614	327,4721	80,7174	0,007731	784,2451
22,2825	1764,12	7148,40033	0,000806	98,4919	201,9816	35,1036	0,012631	770,2633
13,1132	2724,48	7169,99695	0,000145	98,58	259,3383	93,1622	0,004813	791,86
2,2611	1337,96	7197,15246	0,000134	98,3664	239,0998	84,8661	0,00169	819,0155
5,6413	891,97	7183,28969	0,000277	98,5852	195,2318	234,6183	0,006325	805,1527
6,8852	1020,81	7229,83347	0,001	98,8347	332,7928	11,0207	0,006745	851,6965
17,58611	3221,01	7226,19747	0,000792	71,0523	123,9866	24,8603	0,00546	848,0605
5,8424	970	7180,54034	0,000137	98,6303	81,7095	60,1862	0,006023	802,4033
29,0095	5190	7080,65191	0,000159	98,1991	327,2526	88,5102	0,005589	702,5149
33,4262	8225,97	7222,26371	0,00049	70,996	70,2115	253,8401	0,004063	844,1267
17,31557	3171,46	7229,619	0,000951	70,8338	188,2764	247,1589	0,00546	851,482
25,8299	2730,43	7203,27215	0,000151	98,6503	322,7285	56,6433	0,00946	825,1352
33,4262	8225,97	7218,69021	0,000691	71,0088	195,6698	1,6454	0,004063	840,5532
12,9182	1421,21	7152,46853	0,000455	74,0476	218,0031	101,4606	0,00909	774,3315
1,7732	743,31	7094,93346	0,000337	73,9975	279,7907	222,186	0,002386	716,7965
3,5466	815,66	7220,21811	0,000769	98,7481	344,313	119,0486	0,004348	842,0811
3,5466	815,66	7219,75071	0,000905	98,6298	310,827	11,8542	0,004348	841,6137
20,4977	2468,78	7174,47048	0,00019	98,4242	206,1816	49,156	0,008303	796,3335
21,6535	1764,12	7163,54531	0,000237	98,2294	242,1384	229,9351	0,012274	785,4083
5,4363	2775,02	7189,29095	0,000162	98,3049	266,8646	15,2104	0,001959	811,154
13,2927	1969	7080,65387	0,000094	98,2044	320,8825	52,078	0,006751	702,5169
14,9503	924	7177,17291	0,000765	39,576	89,0772	42,5467	0,01618	799,0359
35,1642	9000	7224,09133	0,000465	70,9958	221,5831	330,6496	0,003907	845,9543
2,2038	913,78	7197,60968	0,000391	98,4454	214,3049	21,7428	0,002412	819,4727
10,8063	1450	7154,86166	0,000513	98,1809	239,3917	162,9587	0,007453	776,7247
6,1981	1154	7216,51768	0,00096	98,4725	335,7153	340,3165	0,005371	838,3807
6,8852	1060,46	7224,55882	0,000949	98,8741	333,4819	359,7762	0,006493	846,4218
35,1642	9000	7223,62627	0,00016	70,9774	180,7202	254,8075	0,003907	845,4893

Table 4: Orbital elements and physical properties of debris of the filtered DISCOS list.

It is worth noting that the cross sectional area of some objects was not available. For these (the ones with the red AREA value in Tab. 4), it has been computed weighing the average area of all objects with the object mass with respect to the average list mass.

A further filter on this list can be easily imposed ranking the objects according to their mass. As shown in Fig. 10, imposing a filter at 5000 *kg* allows to discharge only 9 objects, but it limits the actual maximum mass to slightly more than 3000 *kg*. In this way the heavier objects are not considered as we are assuming that dedicated missions or different approaches could be implemented. It is interesting to observe that these heavier objects actually are launcher stages, a class of space junk deserving particular attention. Finally, it is

worth stressing that these objects are not the most dangerous ones as they are enough large and well tracked. Indeed, an operational satellite can always foresee a collision avoidance manoeuvre or design a non-interception trajectory with the tank. Thus, it is reasonable to assume that a foam-based method is actually not the best choice for such debris given their high mass and well known nature that can lead to more tailored solutions for their removal.

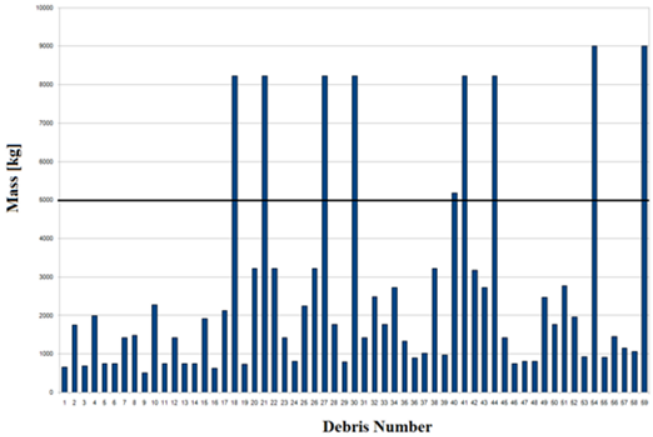

Figure 10: Mass distribution of the DISCOS list. The black horizontal line shows the additional filter applied at 5 *tons*.

- ***Proprietary SSO list:*** While the first list aims to have a broad coverage of relatively large space debris on the LEO region, the second one is based on more stringent filters in terms of orbital parameters.

  According to [7], there are at least three critical regions (see Sec. 1) to be cleaned up before others. The region here considered is the one around SSO orbits. This region contains already several uncontrolled objects and it is still today one of the most important regions for commercial and scientific purposes. Accordingly, we will focus on the Sun-synchronous region limiting the orbital parameters of the objects as follows [7]:

  - Orbital altitude between 600 and 900 *km*
  - Inclination between 97 and 100 *deg*
  - Eccentricity smaller than 0.035

  Besides these constraints, only objects with masses larger than 1 *kg* are considered. In this way, the object list results composed of 140 objects (covered by non-disclosure agreement) with masses up to 8225 *kg*. It is worth stressing, one more time, that the heaviest objects are launcher tank. These, although lighter than the ones found in the DISCOS list, are here considered. On the contrary, the lightest objects of this list are small CubeSats (4 objects) and also these are kept into account.

  This list is more crowded than the previous one in terms of number of objects and also the mass distribution is broader. It is worth recalling, at this point, that the initial debris mass heavily influences the foamed area-to-mass ratio, thus the heavier the object, the larger the foam mass required to deorbit it. In the considered list, half of the objects has a mass smaller than 500 *kg*, the 21.4% is in the range of 500-1000 *kg* and the remaining are mostly concentrated in 1500-2000 *kg* with just 12 objects above 2000 *kg*. This analysis is summarized in Fig. 11.

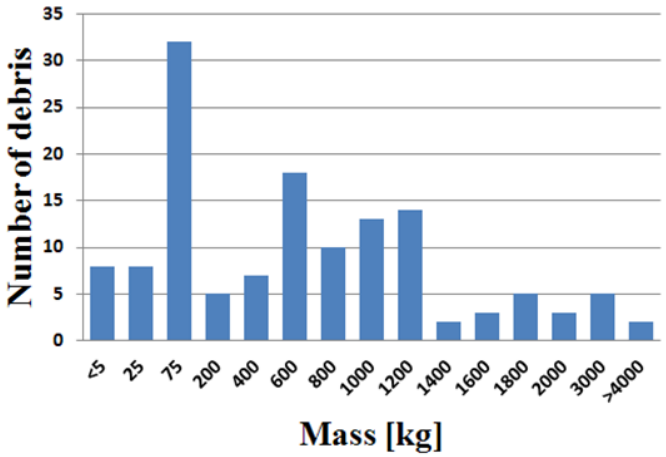

Figure 11: Mass distribution of the proprietary SSO list.

From these considerations, it seems that, in this SSO region, the active deorbiting system proposed should address masses below 1000 *kg* as in this case the total number of objects would be significantly reduced, thus decreasing the number of possible impacts causing a cascade of debris.

- ***UCS Active Object list:*** In order to have an even broader description of the real space debris environment, the last list here considered as set of targets, is based on currently tracked objects. The Union of Concerned Scientists (UCS) [34] makes available a list of hundreds of tracked objects (downloaded at November 2010). These objects are mainly active spacecrafts, but some wise filters can be applied in order to have a list of possible candidate debris.

  The list contains the object launch date and its expected lifetime. The first filter here applied is to consider an object as debris if it is still in the UCS list after the end of its lifetime. This assumes that no mission extension has been foreseen for the given object. Furthermore, in this way only objects large enough to be tracked are taken into account. Further filters on the whole list are imposed in terms of mass and orbital parameters:

  - The debris mass has been arbitrarily limited to 2000 *kg*. The dry mass of the UCS objects has been considered when available, otherwise the launch mass (much more conservative situation) is assumed.
  - The orbital altitude has been limited to 1000 *km*, in order to focus again on the LEO region, the more crowded one. No filters on eccentricity and inclination have been assumed.

  In this way the full UCS list [34] returns 237 objects, covering a possible future scenario of debris objects in LEO.

  Instead providing a full table of these objects, Fig. 12 shows the mass, altitude, inclination and eccentricity of these. It is worth stressing that these objects are not, at least today, space debris and the list can change according to future update of the UCS database.

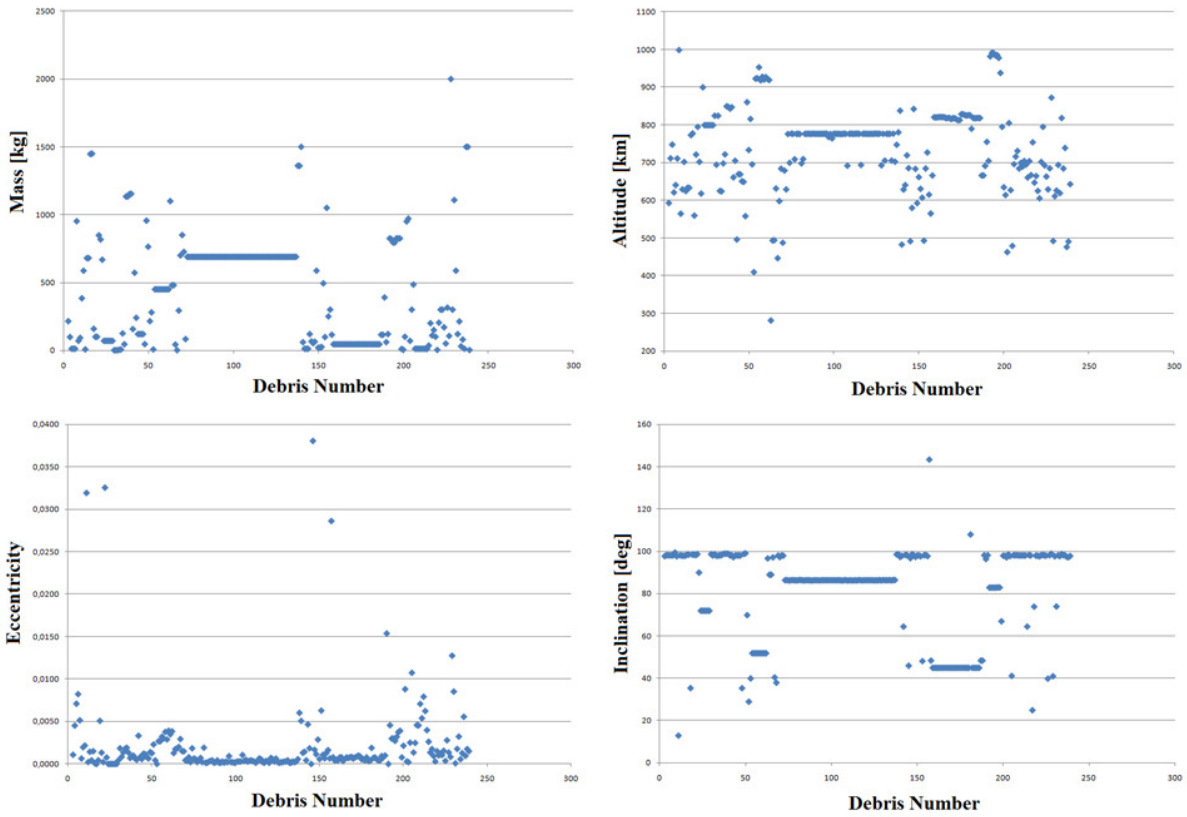

Figure 12: Physical and orbital characteristics of possible future debris according to the UCS list.

In Fig. 12, the long horizontal plateau at approximately 670 *kg* (at an altitude of 777 *km*) is due to the whole *Iridium* satellite series. The smaller one, around 45 *kg* (at approximately 820 *km*), corresponds to the 28 satellites of the *ORBCOMM-FM* series and the last one, very small, around 450 *kg* (at 920 *km*) is due to the *Globstar FM* satellites (9 in this list). The eccentricity plot shows that these orbits are almost circular, as more than the 80% of debris has an eccentricity below 0.003. Finally, the inclination plot shows that the orbits are mainly crowded into highly inclined orbits, around 80 and 100 *deg*, i.e. the Sun-synchronous region (already well described by the previous list). It is worth stressing since now that the presence of few debris out from this range causes a very large mission ΔV in order to change inclination and reach just these few debris. This means that considering dedicated missions, for instance operating at different inclination ranges, would significantly reduce the time required moving from a given debris to the next and accordingly the propellant mass required.

3.2 Impact Probability

The lists so far described can be analysed according to the dangerousness of each object. The specific debris hazard is measured considering a figure including its mass, area, orbit and expected lifetime.

One of the fundamental parameter to take into account, dealing with the dangerousness of space debris, is their impact probability. In general, most of the space objects, both active and inactive, are tracked (e.g. by NORAD). For these objects the impact probability is derived on statistical basis

[30,31]. However, many small size objects can not be tracked increasing the impact probability of active satellites. The impact probability is particularly crucial for telecommunication satellites; principally located in the GEO belt. These objects are quite large and well tracked, thus the new space operation rules oblige these objects to move into disposal orbits at the end of their operative life. Accordingly, since the present active debris method is assessed for regions different from the GEO one, also small size impactors are taken into account to be conservative.

Although the NASA90 model described in Sec. 2.4 is mostly used in the following analyses for the assessment of foam balls impact probabilities, in this section the impact probability is computed by means of the NASA Debris Assessment Software (DAS 2.0) code, due to its higher reliability and the up to date values available [37]. The code relies on "fast" propagation routines ("PROP3D" and "GEOPROP") for the debris environment, and re-entry survivability. The software models include Earth atmosphere and non-uniform gravity field, solar and lunar influences and solar radiation pressure. The solar flux value (used for atmospheric drag calculations) is derived, according to the user supplied starting date, from an integrated database based on standard data published by the National Oceanic and Atmospheric Administration. The solar cycle is computed fitting all the historical values, while the debris environment is based on the NASA's ORDEM2000 model [38], see Sec. 2.3.

The impact probability at a given altitude is computed assuming average values of impact flux [37] at different altitudes, with a step altitude of 25 *km*, considering three impact debris sizes: 10, 50, 100 *cm*. The average number of impacts per year, considering a time span of 90 *years* starting from 01/01/2010, is estimated for 1 m^2 of debris cross section, so that it has to be scaled considering the actual debris area. The DAS output for these input data is shown in Fig. 13.

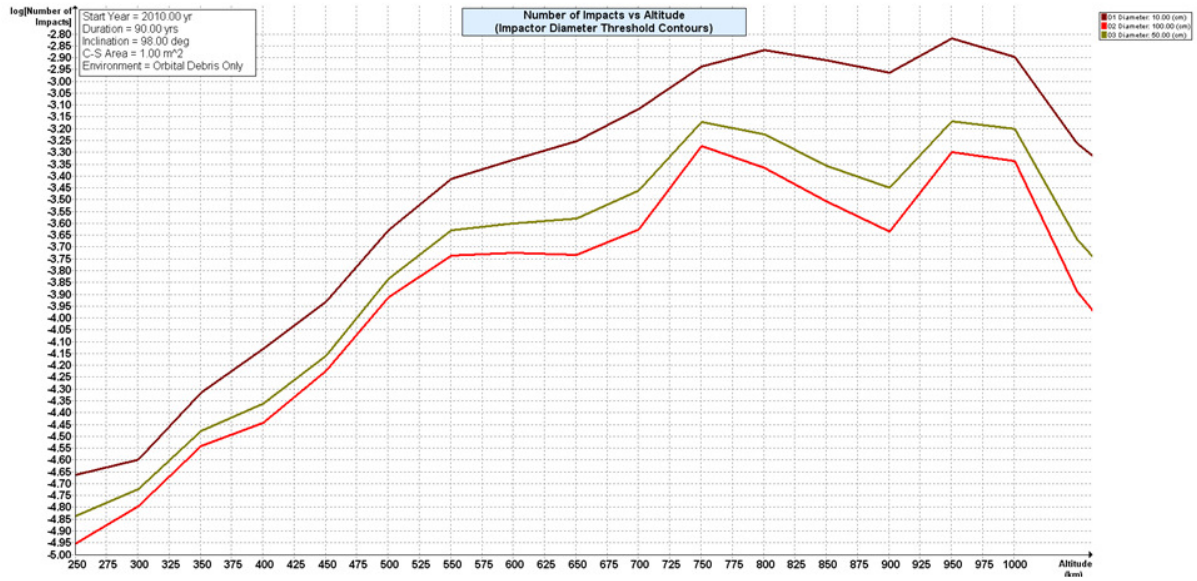

Figure 13: Number of impacts vs. altitude for different sizes of impacting debris.

It is worth noting that these probabilities are computed at 98 *deg* inclination, but the trends are very similar also for different inclinations. Besides the number of impacts, DAS provides also the impact probability per year per unitary cross sectional area. These two data sets, for all the three debris sizes considered, are summarized in Tab. 5 for all the relevant altitudes in the three lists.

Altitude (*km*)	Log Impact Probability (10*cm*)	Log Impact Probability (50*cm*)	Log Impact Probability (100*cm*)	Log Impact Number (10*cm*)	Log Impact Number (50*cm*)	Log Impact Number (100*cm*)
1000	-4,864	-5,154	-5,294	-2,910	-3,200	-3,340
975	-4,814	-5,134	-5,274	-2,860	-3,180	-3,320
950	-4,774	-5,124	-5,254	-2,820	-3,170	-3,300
925	-4,844	-5,264	-5,414	-2,890	-3,310	-3,460
900	-4,924	-5,404	-5,584	-2,970	-3,450	-3,630
875	-4,884	-5,354	-5,524	-2,930	-3,400	-3,570
850	-4,864	-5,304	-5,464	-2,910	-3,350	-3,510
825	-4,834	-5,244	-5,394	-2,880	-3,290	-3,440
800	-4,824	-5,174	-5,324	-2,870	-3,220	-3,370
775	-4,854	-5,144	-5,264	-2,900	-3,190	-3,310
750	-4,894	-5,124	-5,224	-2,940	-3,170	-3,270
725	-4,974	-5,254	-5,404	-3,020	-3,300	-3,450
700	-5,064	-5,414	-5,574	-3,110	-3,460	-3,620
675	-5,134	-5,474	-5,624	-3,180	-3,520	-3,670
650	-5,204	-5,534	-5,684	-3,250	-3,580	-3,730
625	-5,234	-5,534	-5,684	-3,280	-3,580	-3,730
600	-5,284	-5,554	-5,674	-3,330	-3,600	-3,720
575	-5,324	-5,554	-5,674	-3,370	-3,600	-3,720
550	-5,364	-5,584	-5,694	-3,410	-3,630	-3,740
525	-5,474	-5,694	-5,794	-3,520	-3,740	-3,840
500	-5,584	-5,794	-5,864	-3,630	-3,840	-3,910
475	-5,734	-5,944	-6,024	-3,780	-3,990	-4,070
450	-5,884	-6,114	-6,174	-3,930	-4,160	-4,220
425	-5,984	-6,204	-6,294	-4,030	-4,250	-4,340
400	-6,084	-6,314	-6,404	-4,130	-4,360	-4,450
375	-6,184	-6,364	-6,444	-4,230	-4,410	-4,490
350	-6,274	-6,434	-6,494	-4,320	-4,480	-4,540
325	-6,404	-6,554	-6,624	-4,450	-4,600	-4,670
300	-6,554	-6,684	-6,754	-4,600	-4,730	-4,800
275	-6,584	-6,744	-6,834	-4,630	-4,790	-4,880
250	-6,614	-6,794	-6,904	-4,660	-4,840	-4,950

Table 5: Impact probability and impact number for 1 m^2 of debris cross section.

The actual orbital altitude of each debris in the mentioned lists has been compared to these probabilities and the objects ranked according to the product of the corresponding probability for their actual cross sectional area.

Focusing, by way of example, on the SSO region, debris can be ranked according to their area, area-to-mass ratio and total (given by the sum of the impact probabilities with all the three sizes) impact probability, see Fig. 14. Here, on the x axis the debris index number is plotted.

Figure 14: From the upper plot, area, area-to-mass and impact probability for SSO debris list.

The larger the area-to-mass ratio, the shorter the re-entry time, thus the smaller is the probability to determine an accidental impact with another object. The larger the object, the higher the impact probability, and accordingly more hazardous is the object. The higher the impact probability and, of course, riskier the object, the higher the probability that it should be one of the first targets to be deorbited.

As it was expected, the impact probability with smaller impactors is several orders of magnitude larger than the same probability with larger impactors. The model used to compute this probability is not able to appreciate the difference for impacts with objects with a diameter larger than 100 *cm*. For the SSO objects, the initial conditions considered are in a quite close range, thus the largest objects are the ones with the higher danger level. Nevertheless, it is worth noting that an explicit relation between impact probability and area-to-mass ratio, that affects the orbit lifetime, does not exist.

At this point we need a single parameter taking into account all of these factors and considering also the natural lifetime of the debris. We consider here the impact probability factor [12] R as the product:

$$R = A \times N \times L \times P \tag{11}$$

where N is the orbital debris flux (related to the initial orbital altitude by Tab. 5) for 1 m^2 of cross sectional area, A is the object cross sectional area, P the orbital period and L the expected number of revolutions. L can be roughly assessed by means of [39]:

$$L = -H / \Delta a_{rev} \tag{12}$$

where H is the atmospheric scale height [39]. The resulting lifetime L is given in number of revolutions, thus to be transformed in a time it is multiplied by the orbital period.

Δa_{rev} is the semi-major axis change per revolution due to the atmospheric drag. It can be computed by means of quadrature of the atmospheric force over the true anomaly and it turns out that modified Bessel functions are required to obtain this averaging [39]. For nearly circular orbits (like the ones in SSO and in general for many orbital debris orbits made circular by the atmospheric drag effect), it can be expressed as:

$$\Delta a_{rev} = -2\pi (C_d A / m) \rho a^2 \tag{13}$$

Here C_d is assumed constant and equal to 2.2 for all debris. The variation of orbital altitude is assumed caused only by the atmospheric drag. Δa_{rev} should be considered changing during the re-entry; however, as done for the atmospheric density, it has been assumed uniquely determined by the initial debris altitude. This means that the lifetime estimation, given by LxP, is conservatively computed assuming that the debris lives all the time at its initial altitude. Thus, resulting values are not the real deorbiting times of objects; rather they are indexes taking into account the area-to-mass ratio role in the debris danger level ranking. It is now possible to rank all debris lists, associating to each object the corresponding R value. This is presented in Fig. 15 where the R value has been normalized with its maximum.

For the UCS list, however, the actual cross sectional area for each object could not be used, due to the lack of this parameter in the list. In order to overcome this problem, a statistical approach has been used. According to [39] a rough estimation of volume, dimension, area and moment of inertia of a generic spacecraft can be computed by its mass. This approach is based on statistical analyses on a number of spacecrafts and has to be considered as a relation providing an order of magnitude of the object area. In this way the cross sectional area can be computed as:

$$A = (0.25 m^{1/3})^2 \tag{14}$$

where m is the object initial mass in kg and A is expressed in m^2.

Figure 15: From the upper plot: DISCOS, SSO and UCS lists ranked according to the normalized *R* value of each debris. The higher the *R* value, the more hazardous is the debris.

It is worth noting that, while in the first plot of Fig. 15 the missing data correspond to the filtered (due to their mass larger than 5 *tons*) objects of the original DISCOS list (see Tab. 4), in the second and third plots of Fig. 15, there are no empty spaces but just very small values of *R* that can not be appreciated in the plot scale.

Just as comparison, it is possible to superimpose this sorting with the one where only the product *AxN* is considered. This comparison highlights the different risks resulting from a long term(*R*) and

a short term (*AxN*) analysis. This comparison is shown in Fig. 16. It is clear that the two sortings are not the same and, in particular high cross-sectional area objects do not usually have a proportionally larger mass with respect to small debris, thus their lifetime can be much smaller than middle size objects with small masses, that turn out to be the most dangerous ones. This is particularly clear for the DISCOS and UCS lists where the more dangerous objects (the ones with the highest *R* value) do not coincide with the ones with the larger *AxN* value. For the SSO list, instead, the same object takes the maximum in both cases.

Figure 16: From the upper plot: DISCOS, SSO and UCS lists ranked according to the normalized *R* and *AxN* value of each debris. High *AxN* values might be coupled with short lifetimes, making the corresponding debris not the most hazardous ones.

Furthermore, it is worth to observe that the *R* value for heavy objects might be smaller than the sum of the same value of several objects giving the same total mass. This means that removing several light debris would actually be a more effective strategy rather than removing just one heavy object. Nevertheless, in the following analysis (see Sec. 10), besides the number of objects deorbited per year, also the deorbited mass is considered.

The objects with the first two larger *R* values in the DISCOS list have a mass of approximately 3000 *kg*, and area-to-mass ratio around 0.005 lying at 850 *km* altitude. Most probably they both belong to the same satellite class (information not available). In the SSO list, instead, the object with the maximum *R* and *AxN* is the same. It has a very large mass, more than 8200 *kg*, with an area-to-mass ratio of 0.004 and its orbital altitude is around 810 *km*. Finally, in the UCS list (where the same plateaus observed in Fig. 12 are visible), there is a whole group of objects with significantly larger *R* values. These have a mass around 820 *kg* and an area-to-mass ratio (computed by means of Eq.(14)) close to 0.006 and move on almost circular orbits around 980 *km*.

It is worth noting that, in order to have the lists covering a broad range of scenarios, the heaviest debris are eliminated only from the DISCOS and UCS list, while they are kept in the SSO list, where objects up to 8200 *kg* are present. This kind of objects assumes significantly higher values of *R*, but for these, as already stressed, ad-hoc mission should be conceived.

3.3 Suitable Target Debris

Although the preliminary mission analysis, to assess the performance of the foam-based debris removal system, is carried out in Sec. 10 on the whole lists; the aim of this section is to identify a suitable range of objects for the proposed application. These suitable targets should be the most hazardous ones (according to the *R* classification), not too heavy (otherwise single-object missions should be considered) and moving into the more crowded regions (e.g. SSO).

Before pursuing this goal, all the objects of the three lists can be gathered together to identify the regions covered by these objects. As shown in Fig. 17, the UCS list is the only list somehow representing debris below 700 and above 900 *km*. The other two lists populate this region, with a broad range of mass values. In the right plot of Fig. 17, a close up of the region between 450 and 1000 *km* is shown with a mass limit at 5000 *kg*. In this way only 11 debris (from the DISCOS and SSO lists) are excluded, the heaviest ones requiring specific missions. Here the first zone (shadowed by a blue ellipse in Fig. 17) is composed of objects up to 3 *tons* and spans the range 450-700 *km* altitude. The second zone is the most crowed one (and the same should be also considering the actual space debris population, assuming the three lists enough representatives), highlighted by the pink ellipse in Fig. 17. It is composed of objects from 1 up to 5000 *kg* moving between 700 and 900 *km*. In this zone the UCS list contains object with masses up to about 2 *tons*, while the DISCOS list contains medium-large objects. The SSO list, specifically suited for this region, spans all the mass range.

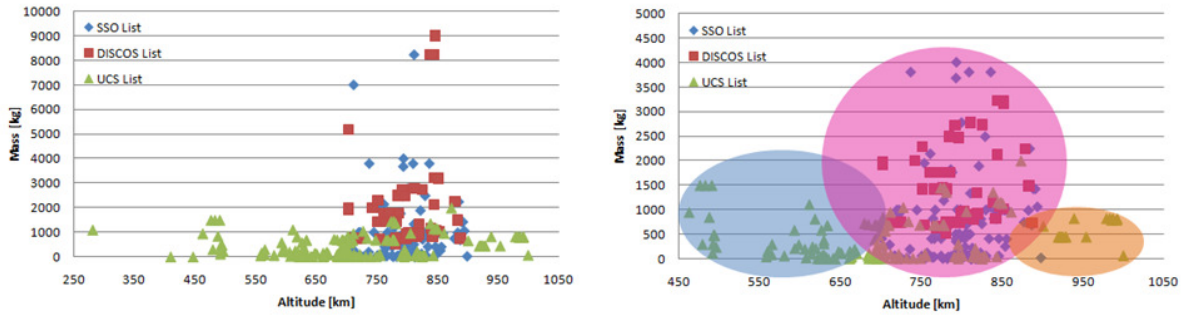

Figure 17: Altitude distribution of the three lists. Close-up on the right (450-1050 *km*) with the three main regions highlighted with shadowed ellipses.

Finally, the last zone of Fig. 17, the orange one, is composed of objects up to 1 *ton* moving above 900 *km* altitude. This region is not really populated and it is composed only of objects in the UCS list.

The comparison of Fig. 17 motivates to explore, in particular, the performance in the SSO region (where the SSO list seems the most appropriate). The comparison also shows that the lower LEO region is represented only by the UCS list, thus its analysis gives an idea of the performance of the method in the whole 250-1000 *km* region. At this point, it is clear that the suitable debris target should lie, as already stressed by [7], in the SSO region.

A second analysis can be done gathering all the objects and ranking them with respect to their area-to-mass ratio and *R* value. From the leftmost plot of Fig. 18, it is clear that the great majority of objects has an area-to-mass ratio lower than 0.03 (that would result, at an average altitude around 800 *km* in 20 *years* of lifetime). Approximately one half of debris in the DISCOS list have area-to-mass ratios below 0.005, due to the filters imposed on area and mass. On the contrary, objects in the UCS list cover the whole range, thus also higher values.

The rightmost plot of Fig. 18, indeed, shows the *R* value of all the objects with respect to their orbital altitude. A general increasing (exponential) trend of this value with the altitude is clearly visible and it is caused by the increasing orbit lifetime. All the three lists contain some of the most hazardous objects that are grouped in the region 800-1000 *km*, but the UCS and SSO lists are the only ones containing also the less hazardous objects.

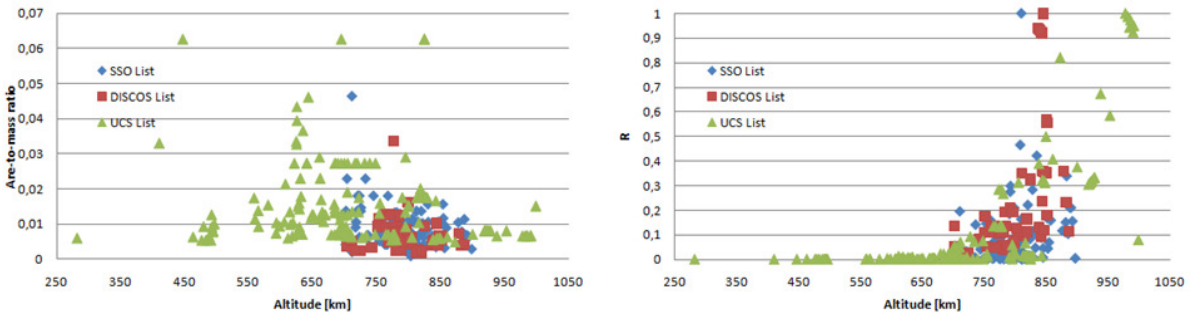

Figure 18: Area-to-mass ratio (left) and *R* impact probability (right) with respect to orbital altitude for the three lists.

The last comparison is here made ranking the hazardousness of all objects (represented by the *R* value) with respect to their mass, as shown in Fig. 19. Here in the left plot all objects are shown and no regular pattern can be actually recognized. The DISCOS list, due to the filters imposed, is the

only one that presents a general increasing of the *R* value with the mass, while the UCS list (more crowded and spatially more distributed) does not show any pattern. This actually means that, as expected, the heaviest objects are not the most hazardous ones, but there are combinations of area-to-mass ratio, orbital altitude, lifetime, cross sectional area, mass and impact probability that make medium size objects orbiting at medium-high altitudes the major space debris threat. On the right plot of Fig. 19, a close up, limiting again the mass to 5 *tons*, of the left plot is shown.

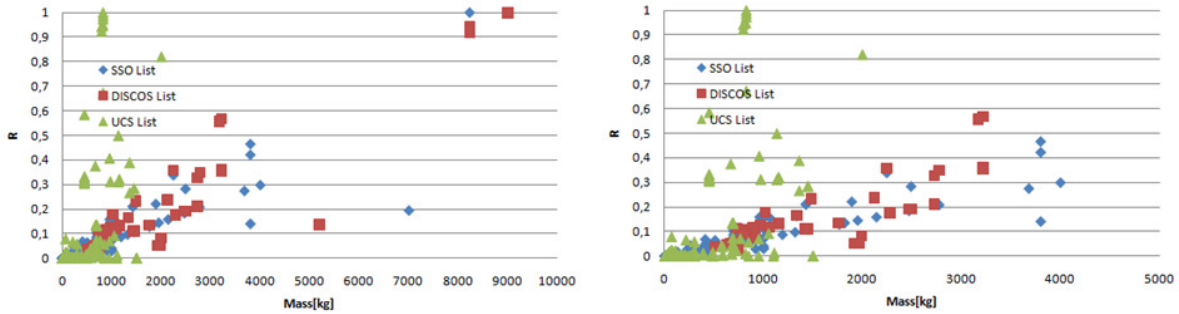

Figure 19: Impact probability of the objects of the three lists with respect to orbital altitude. Close-up on the right.

From these last plots; it is clear that there are two groups of very hazardous debris. The heaviest ones that are, however, not suitable targets for the considered application as they would require too much foam (a rough idea of the foam mass with respect to the object mass or area-to-mass ratio is given in Sec. 1). Equally hazardous, but more realistic for the foam-based method, targets are 1 *ton* debris moving around 1000 *km*, these are contained in the UCS list and are the most hazardous ones in the mass range considered. Slightly less hazardous, but equally suitable targets for the proposed methods, are 3-4 *tons* objects around 850 *km*. These are enclosed both into the DISCOS and SSO lists and can be considered as the preferred targets since they move into a very crowded region (see. Fig. 17).

4 OPTIMUM FOAM BALL RADIUS

One of the main advantages of the proposed method lies in the possibility to tailor the foam ball on target debris orbit and characteristics. Indeed, the foam ball size has to be identified during the early phases of the mission definition, according to the specific targeted debris and the mission schedule. In this section we will consider both the time needed to deorbit the debris with the foam-based deorbiting method, and the impact probability of the foam ball with respect to other debris, to estimate the optimum foam ball radius (see Sec. 2).

One of the major drawbacks of considering large radius values is represented by the proportional growth of the mass of ejected foam with the foam volume, i.e. with the cube of the radius. Since the area exposed to the atmospheric drag, under the hypothesis on perfect sphere, only increases with the radius squared, the expected area-to-mass ratio of the foamed debris does not show an unlimited growth.

Considering a foam density value ρ_F, after the expansion phase, of 1 kg/m^3 (see Sec. 7) and a range of debris mass from 50 to 9000 kg, the obtainable area-to-mass ratio is given by:

$$\frac{A}{m} = \frac{\pi r^2}{\frac{4}{3}\rho_F \pi r^3 + m_D} \tag{15}$$

where r is the foam ball radius and m_D the initial mass of the debris. Figure 20 shows the area-to-mass ratio of the debris after the foaming process for different values of the initial debris mass for a range of foam ball radius from 1 to 15 m. The red dots on each line highlight the maximum ratio for the considered ranges of mass (50-9000 kg) and radius (1-15 m).

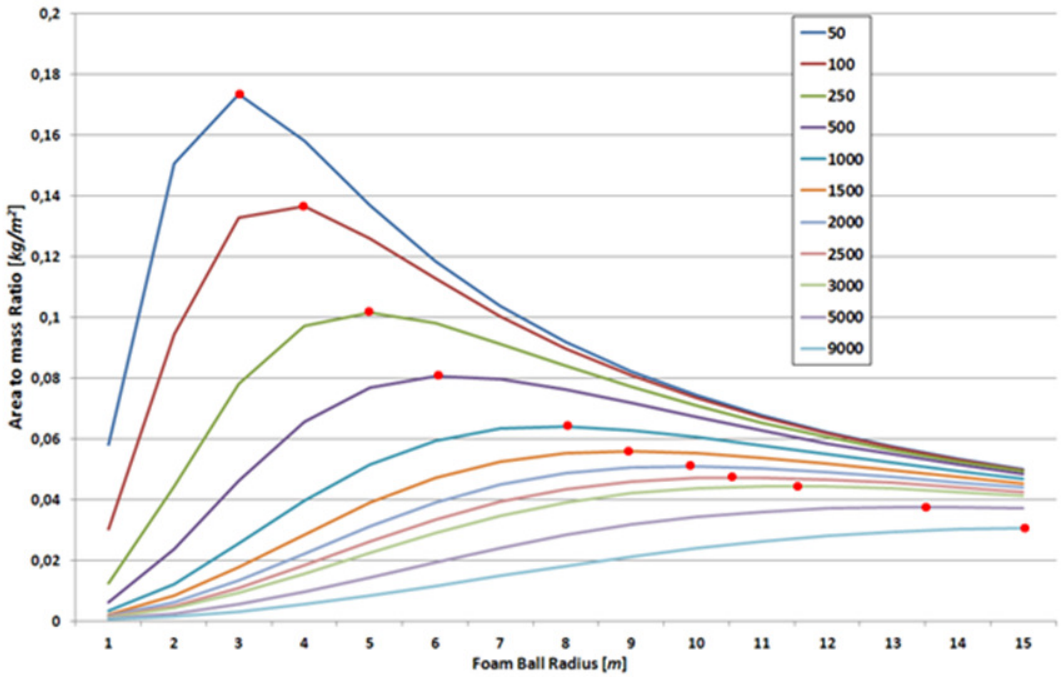

Figure 20: Area-to-mass ratio vs. foam ball radius for different values of the initial debris mass.

The cyan line in Fig. 20, corresponding to an initial debris mass of 9000 *kg*, presents a maximum point outside the considered range but we still considered 15 *m* a reasonable upper threshold for the radius.

Curves maxima can be also obtained analytically by taking the first derivative of Eq.(15) with respect to the radius and expressing the optimum radius as function of debris mass. It reads:

$$r_{opt} = \sqrt[3]{\frac{3}{2}\frac{m_D}{\pi\rho_F}} \tag{16}$$

Equation (16) thus provides the relation between the ball radius resulting in the maximum area-to-mass ratio and the debris size for a given value of foam density. This relation is plotted in Fig. 21 considering masses from 50 to 9000 *kg*.

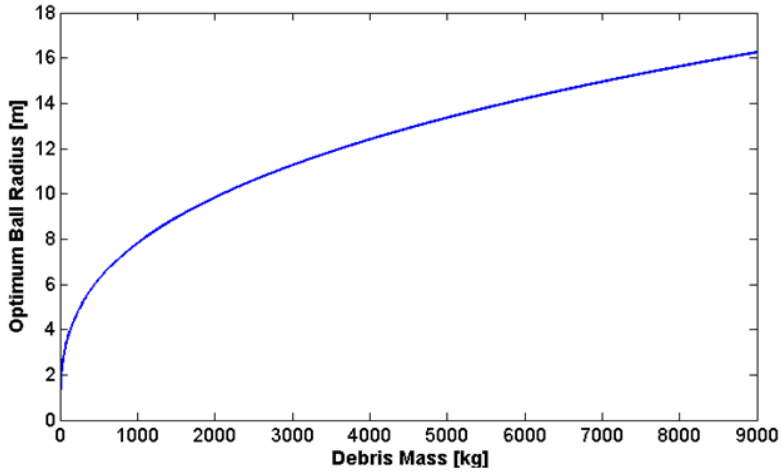

Figure 21: Debris mass vs. optimum foam ball radius.

It is worth mentioning that we are not considering the initial volume of the debris itself so the resulting values obtained in this analysis have to be considered conservative. Moreover, this general trend depends not only on the initial debris mass but it is strongly affected by the assumed foam density value. Considering the density value so far used, see Sec. 7, this method seems effective for those debris with mass smaller than 1000 *kg*, but this value can be increased even by two or three times considering smaller foam density values.

Results of this analysis still do not take into account the impact probability increase associated with these large exposed areas. For this reason, the obtained values only represent an upper limit for the foam ball radius that will be better assessed in the next section considering the debris flux and the resulting impact probability by means of the NASA90 model described in Sec. 2.3.

4.1 Foam balls impact probability

The identification of the optimum foam ball size for each debris starts from the assessment of the deorbiting time of the debris and the corresponding impact probability for different values of the drag exposed area. The obtained curves show two opposite trends for growing values of the foam ball radius. The deorbiting time is computed by means of the method described in Sec. 2.1 for

different solar activity conditions. The impact probability is then obtained combining Eq.(11) with the debris flux value obtained by means of the NASA90 model, described in Sec. 2.3, for minimum impactor diameter of 10 *cm*.

By way of example, Fig. 22 shows the impact probability (left) and deorbiting time (right) values interpolated by means of a third order polynomial among the exposed area values. The two curves are obtained considering, for the object of the DISCOS list with the highest impact probability (index number 26), a variable quantity of foam which results in different exposed areas, volumes and then masses.

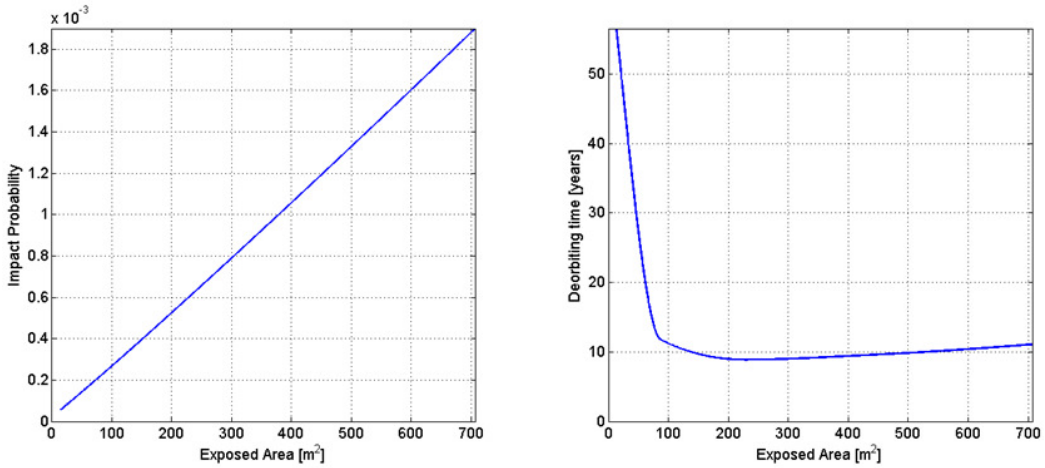

Figure 22: Impact probability (left) and deorbiting time (right) vs. atmospheric drag exposed area values.

For the purposes of an Active Debris Removal mission, the primary aim is a fast and safe debris deorbiting. This entails that both a time and an impact probability constraint should be satisfied. This is a typical constrained minimum problem where the aim is to find the foam ball area that minimizes a given performance index satisfying both requirements that can be treated as constraints:

$$\begin{gathered} \min J\left(A,\mathrm{p}\right) \\ s.t. \\ \begin{cases} P\left(A,\mathrm{p}\right) < P_{threshold} \\ T\left(A,\mathrm{p}\right) < T_{threshold} \end{cases} \end{gathered} \tag{17}$$

where J is the objective function (e.g. deorbiting time), A the foam ball exposed area and p the remaining parameters of the problem (e.g. initial debris altitude, solar activity, etc.). The last two relations ensure that the time (T) and impact probability (P) requirements have to be always satisfied if there is a non-empty admissible domain for the solution of the minimum problem.

The constraints values are given by the guidelines followed by the national space agencies for spacecrafts post-mission disposal. The deorbiting time constraint is then identified with the 25 *years* limit stated by the IADC guidelines (see Sec. 1), while the impact probability constraint is taken considering the NASA requirements [12] for the probability of accidental collisions with space objects larger than 10 *cm* in diameter: 0.001.

The size of the admissible region obviously depends on the physical characteristics of target debris and, in some cases, the deorbiting time and impact probability requirements can definitely preclude the existence of such region and accordingly the solution of the problem of Eq.(17).

Considering the deorbiting time as the objective function, it is possible to associate two Lagrange multipliers, α and β, to the constraints on T and P in order to define an augmented performance index: $\bar{J} = T + \alpha P + \beta T$. Furthermore two (positive) slack variables, p^2 and t^2, are introduced in order to turn the two inequalities of Eq.(17) into equalities. The minimum of the augmented objective function, accordingly, can be obtained solving the following system:

$$\begin{aligned} &\alpha \frac{\partial P(A)}{\partial A} + (1+\beta)\frac{\partial T(A)}{\partial A} = 0 \\ &P(A) + p^2 - 0.001 = 0 \\ &T(A) + t^2 - 25 = 0 \\ &2\alpha p = 0 \\ &2\beta t = 0 \end{aligned} \tag{18}$$

where the first equation is the derivative of the augmented performance index with respect to foam ball area (the independent variable), the second and third are the results of the partial derivatives of $\bar{J}$ with respect to the Lagrange multipliers and the last two equations result from the derivatives with respect to slack variables.

System (18), contains all possible situations that can take place in the minimization problem of Eq.(17), i.e.:

- $\alpha=\beta=0$; $\bar{J}$ corresponds to J, i.e. the minimum of the deorbiting time is not controlled by the constrains (the solution is in the allows region).
- $\alpha=t=0$; the minimum of the augmented performance index corresponds to the minimum of the deorbiting time that equals the time limit constraint (the solution is on the boundary of the deorbiting time of the feasible region).
- $p=\beta=0$; the minimum of the augmented performance index gives a foam ball area providing the maximum allowable impact probability (the solution is on the boundary of the impact probability of the feasible region).
- $p=t=0$; the foam ball area value obtained solving the system represents both a limit time and impact probability constraint (the deorbiting time boundary and the impact probability one correspond and the solution is in that point).

It is clear that only some of these cases may provide valid solutions. Nonetheless, considering the characteristics of the debris listed in Sec. 3.1, most of the debris of the DISCOS list exhibit an empty admissible domain for the solution of the minimum problem. By way of example, two debris (n°16 and 4) of the DISCOS list have been considered and the corresponding foam ball area versus deorbiting time and impact probability plots are given in Fig. 23.

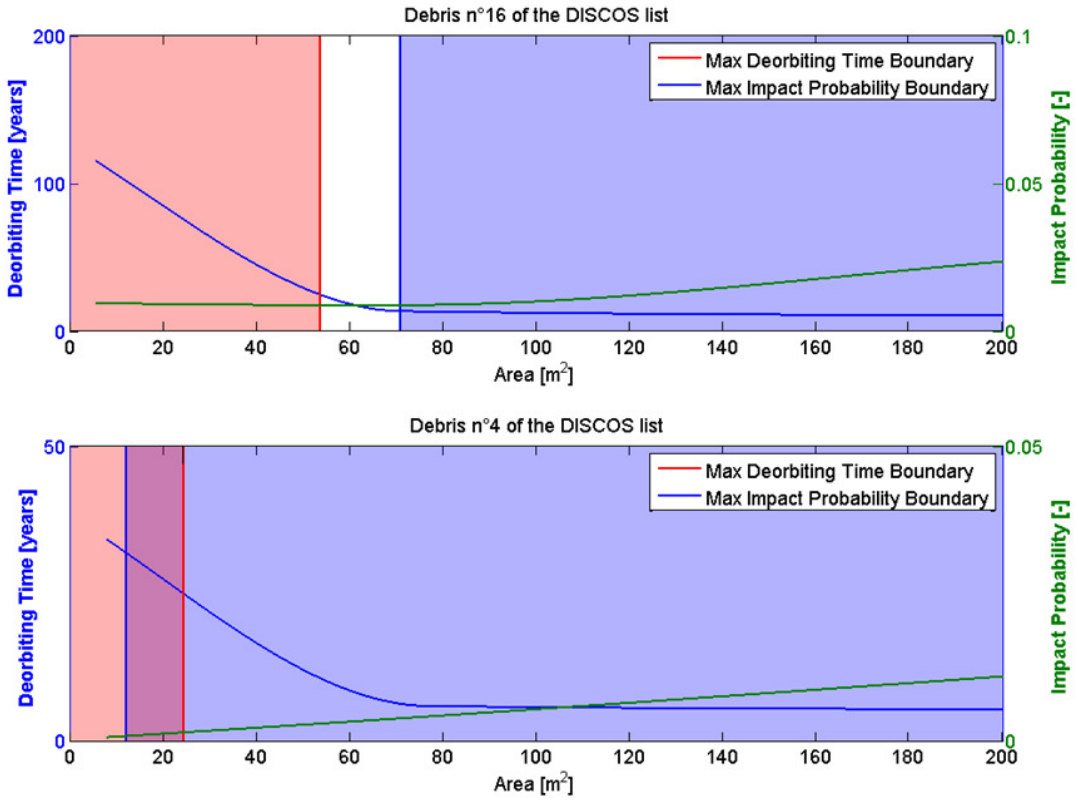

Figure 23: Foam ball area vs. deorbiting time and impact probability for debris n°16 and 4 of the DISCOS list. In the lower plot, the forbidden region is overshadowed.

Plots of Fig. 23 show the forbidden region given by the constraints on the impact probability (blue region) and the deorbiting time (red region). The upper plot of Fig. 23 clearly shows a non-empty admissible domain for the solution of the minimum problem (white region), where the system of Eqs.(18) provides a valid solution. On the contrary, from the lower plot of Fig. 23, it is clear that debris n°4 of the DISCOS list can not deorbit within the 25 *years* limit satisfying also the impact probability constraint, i.e. there is no admissible domain for the solution of the minimum problem since the forbidden regions overlap.

Since the behaviour shown for debris n°4 of the DISCOS list is rather representative for the whole list (35/50), this method is not here adopted although it represents the classical way to handle constrained minimization problems. For the sake of completeness, in the other two lists, this region superposition occurs only for 3 out of 237 debris for the UCS list and for 11 out of 140 debris for the SSO list.

A completely different approach, which is actually a trade between the two criterions, is here followed. It is based on the assumptions that the two former requirements represent guidelines rather than constraints. This method allows a large number of valid results as it aims at the identification of the minimum of a weighted sum:

$$\min\left[\alpha P(A,\mathrm{p})+\beta T(A,\mathrm{p})\right] \tag{19}$$

where, in this case, α and β represent non-dimensionalizing parameters for the two quantities (T and P). These two parameters, indeed, are obtained as the inverse of the maximum allowable impact probability ($\alpha = 1/P_{threshold}$) and of the time limit ($\beta = 1/T_{threshold}$). For the actual computations, however, the deorbiting time threshold has been assumed as 5 *years*, considered as a very desirable

goal. It is worth stressing that all the above considerations are still valid since the allowed region just tends to be shirked down decreasing the deorbiting time threshold.

The two resulting non-dimensional curves have been summed up to obtain a total curve as shown in Eq.(19), which exhibits a minimum for the optimal value of the drag-exposed area, see Fig. 24.

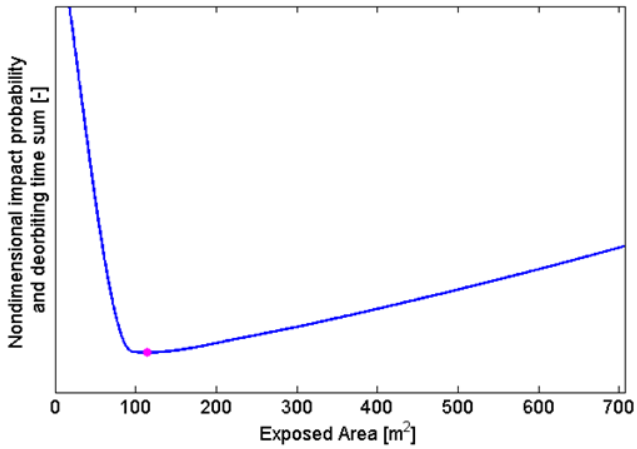

Figure 24: Sum curve of the impact probability and deorbiting time vs. atmospheric drag exposed area values. The red dot highlights the minimum. Ticks on the Y axis have been omitted since they actually have no physical meaning.

Thus, the optimal ball size is obtained as the best compromise between deorbiting time and impact probability for each debris considered for which a plot like the one of Fig. 24 has been drawn. Of course, this value is not only function of debris orbital elements and physics characteristics, but also the atmospheric conditions play a primary role in the assessment of these values. In this approach, the two requirements are a-posteriori considered to verify if the foam ball area value obtained satisfies the two criteria.

Finally, it is worth mentioning that comparing the results of the first method (for those debris allowing the application of the method) with the one just described, the maximum, minimum and average difference between the predicted deorbiting times are 1.3, 0 and 0.32 *years*. The maximum, minimum and average differences between these new foam ball radii and the old ones are -0.32, 0 and -0.15 *m*.

4.2 Results and performance

Figures 25-27 show the optimum foam ball radius for the DISCOS debris, their deorbiting time before and after the foaming process (in the following defined as “foamed deorbiting time”) and the ratio of these two values for three different solar activity and atmospheric density conditions. All these three conditions can be modelled with the Harris-Priester atmospheric model (see Sec. 2.2) and correspond to minimum, medium and maximum solar activity conditions. Since in the DISCOS list used for this analysis is catalogued by increasing mass, the radius values show an increasing tendency in each of the optimum foam ball radius plots. Each plot also presents a horizontal red line at 10 *m*, assumed (see Sec. 1) as a reasonable upper threshold for the ball radii (see Fig. 6).

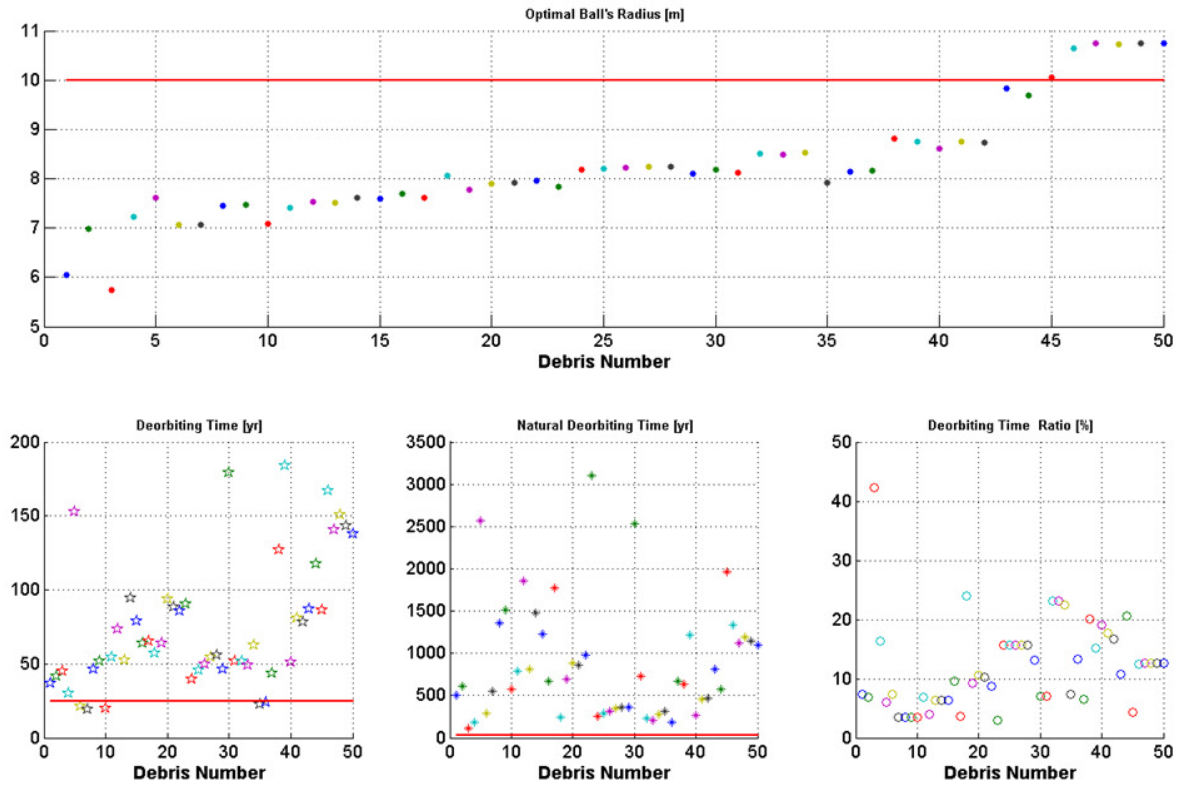

Figure 25: Optimum foam ball radius, natural deorbiting time, foamed deorbiting time and their ratio for the DISCOS list in the minimum density scenario.

It is clear from plots in Fig. 25 that results obtainable with this method, considering a scenario with constant minimum atmospheric density, are actually not encouraging. The foam ball radii span from 5.7 to 10.8 *m*, providing deorbiting time values from 19 up to 180 *years*. It is still important to note that, even if the debris deorbiting time does not cope with the desirable goal value (5 *years*) or with the limit provided by IADC Guidelines (25 *years*), the ratios between the deorbiting time after and before the foaming process lie between 3.3 and 42 percentage points. Thus, even in a so unrealistic scenario, this method provides an enhancement of the deorbiting time up to 30 times the natural deorbiting time of debris. Indeed, the assumption that the atmospheric density remains at its minimum is rather unrealistic as it depends on the solar cycle with a period close to 11 *years*.

It is then important to remark that for this method, as for any other method based on drag augmentation, it is more realistic to assume that an active debris removal mission should have to be started during a medium or even a high atmospheric density period (see Sec. 2.2). Under this consideration, the results related to the medium atmospheric density case, presented in Fig. 26, deserve much more attention since they represent a more realistic application scenario.

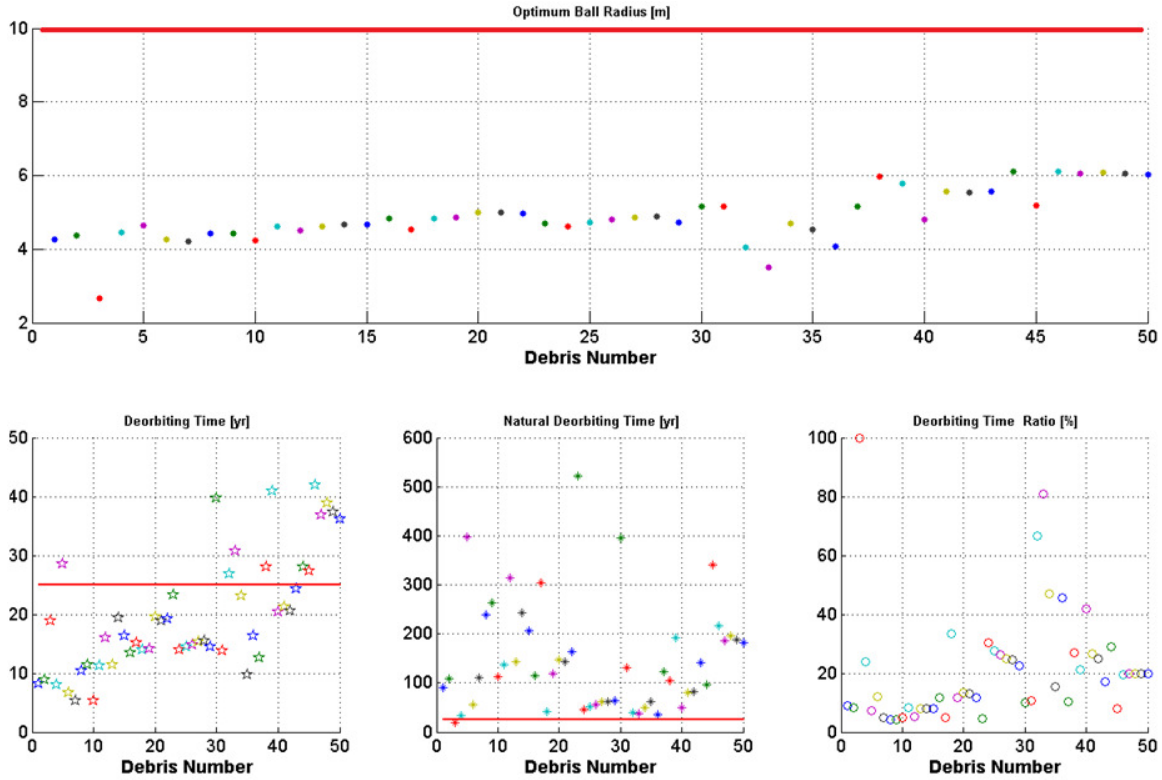

Figure 26: Optimum foam ball radius, natural deorbiting time, foamed deorbiting time and their ratio for the DISCOS list in the medium density scenario.

In the upper plot of Fig. 26 the optimal foam ball radii for DISCOS debris, span from slightly more than 2 *m* up to about 6 *m* with most of the deorbiting time values lower than 25 *years* and an average deorbiting time ratio smaller than 20%. Also in this case some of debris do not succeed in deorbiting within the prescribed time limit, but it is worth noting that the radius value could still be increased (see Fig. 21) and that the deorbiting time is enhanced up to 25 times the natural deorbiting time. The anomalous behaviour of debris n°3, the one which shows a deorbiting time ratio of 100%, is due to the original area-to-mass of the object that already grants a deorbiting time of less than 25 *years* in a medium atmospheric density scenario.

The same analysis has been carried out also for the high density model, as shown in Fig. 27.

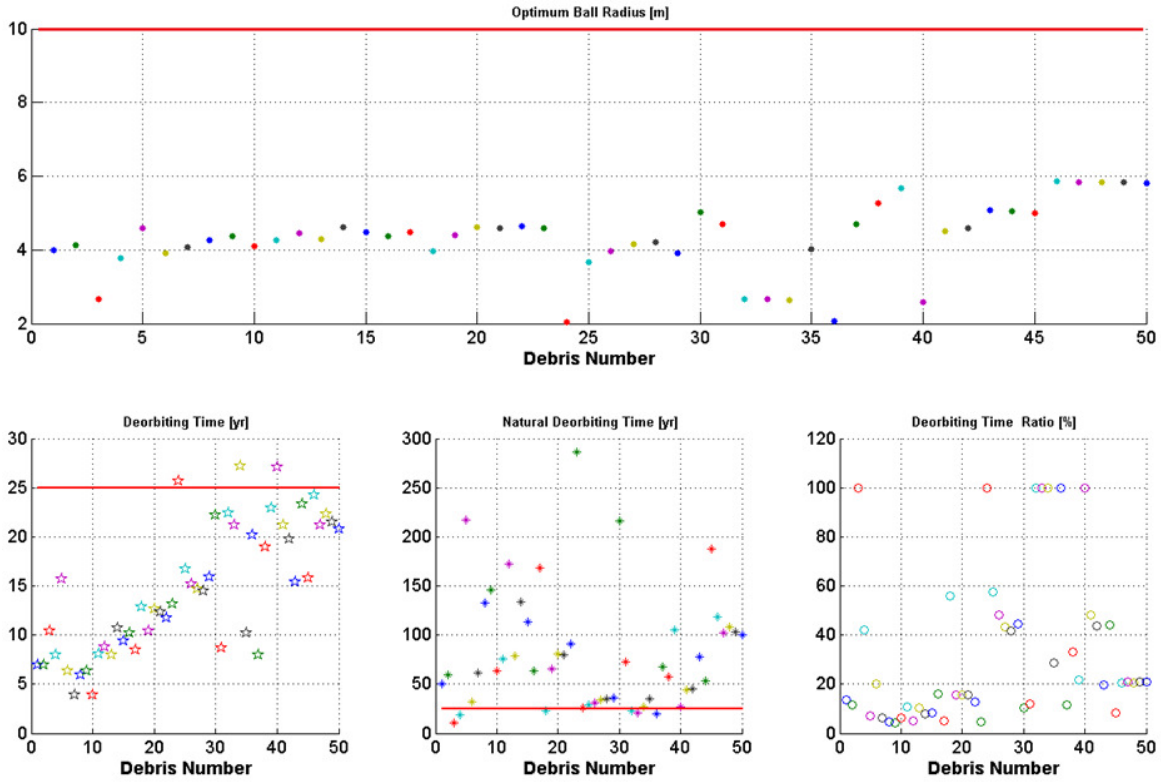

Figure 27: Optimum foam ball radius, natural deorbiting time, foamed deorbiting time and their ratio for the DISCOS list in the maximum density scenario.

A mission scenario with this maximum atmospheric density model provides, of course, much better results both in terms of foam ball radius (slightly smaller than the previous ones) and deorbiting time for each debris but, on the other hand, the average deorbiting time ratio turns out to be 30%. This difference is quite obvious since the natural deorbiting time values run into a high decrease and a drag augmentation method becomes not so essential. Also in this case those debris with a large area-to-mass ratio do not get significant advantages from the utilization of this method.

Figure 28 shows the impact probability for each foamed object of the DISCOS debris respectively in the minimum, medium and maximum atmospheric density regimes. These values are obtained by means of the NASA 90 formulation described in Sec. 2.4 for the optimum foam ball radius values. Also in this case, we can observe an increasing tendency in the impact probability plot due to debris list sorting. Indeed, heavy objects tends to have longer deorbiting times and, consequently, higher impact probability.

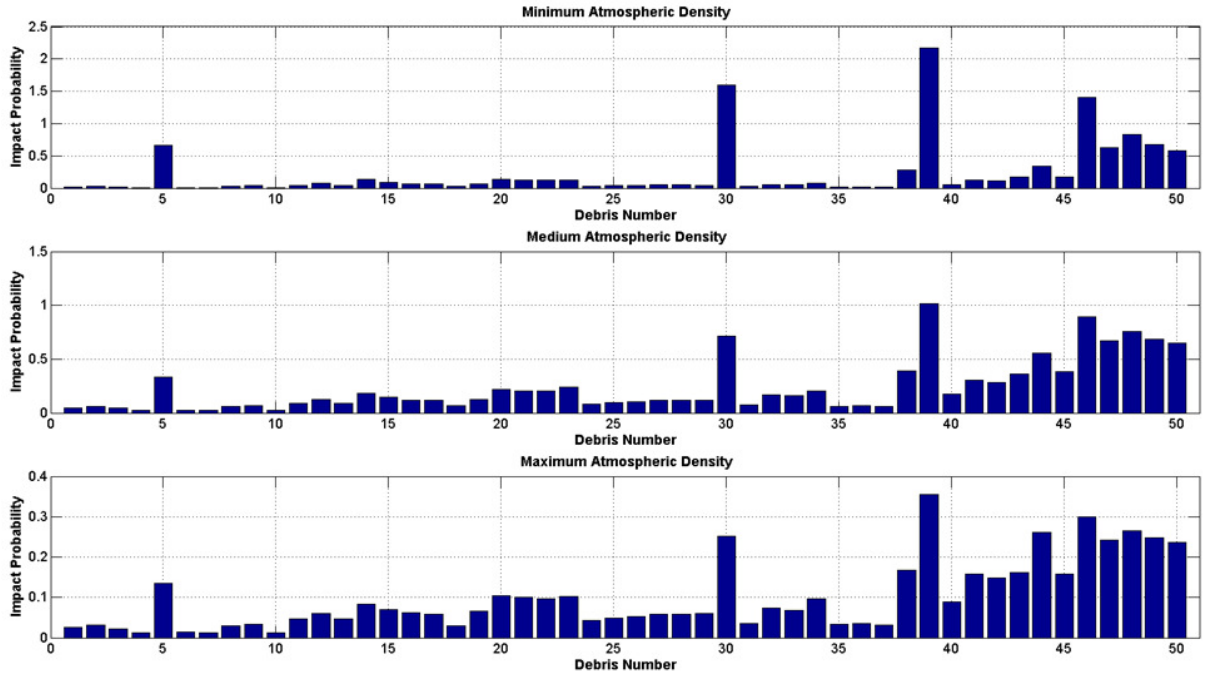

Figure 28: Impact probability for the DISCOS list in the minimum, medium and maximum density scenario.

Observing the original area-to-mass ratio and its change for different atmospheric density scenarios, it is easy to notice that objects with a large area-to-mass ratio do not get significant advantages from this drag augmentation method and the influence of the atmospheric density scenario, as shown in Figs. 29-30.

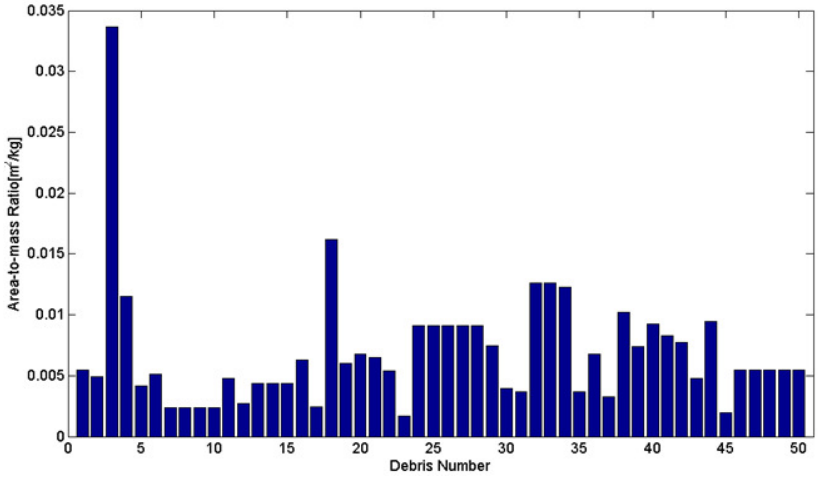

Figure 29: Original area-to-mass ratio for the debris of the DISCOS list.

Figure 30 shows the area-to-mass ratio of foamed debris over the original debris area-to-mass ratio, plotted in Fig. 29, for each debris in the DISCOS list in the three atmospheric density scenarios. In Fig. 30 it is easy to observe that the increase in the area-to-mass ratio before and after the foaming process, changes for the three scenarios. In particular, for a given debris, this value is, on average, larger in the minimum density scenario than in the other two.

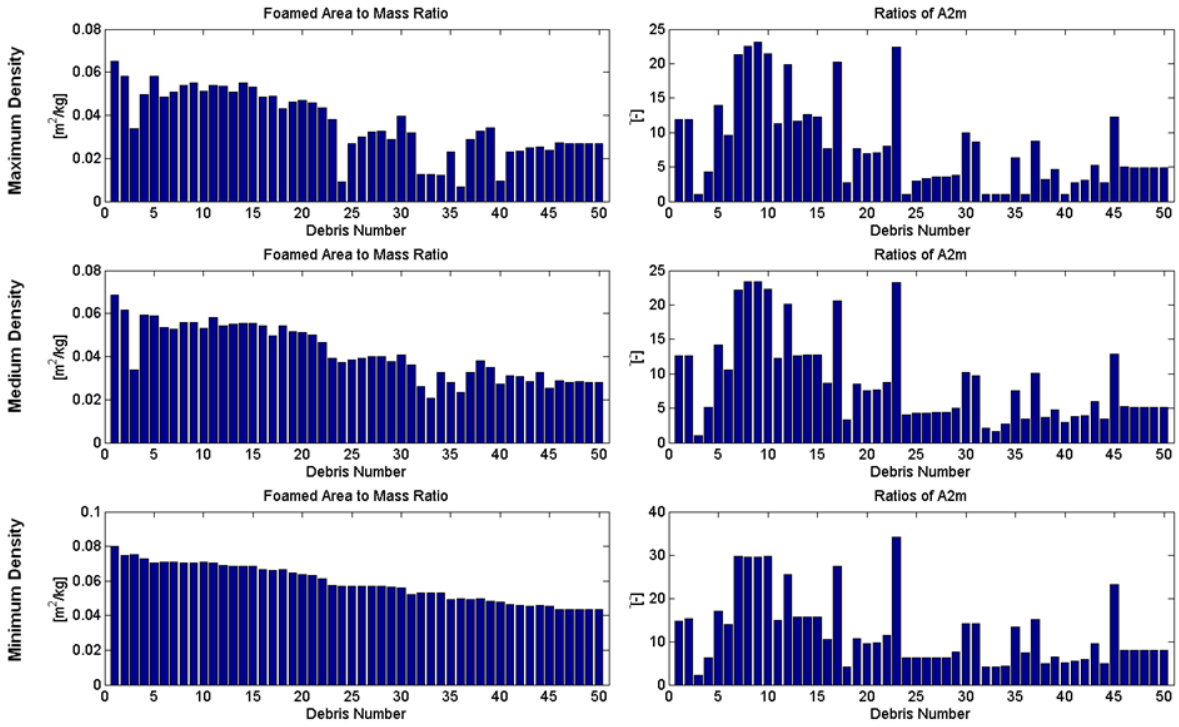

Figure 30: Foamed area-to-mass ratio and old-to-new area-to-mass ratio for the DISCOS debris list in minimum, medium and maximum density scenarios.

Figures 29-30 also clearly show the reason of the anomalous behaviour previously described for some debris showing a deorbiting time ratio of 100%. In that case the original area-to-mass ratio (see Fig. 29 for debris n°3) is already large enough that no valuable effects can be provided by the foam-based method (or any other drag augmentation device).

Since the ball radii, resulting from the high density scenario, in some cases lead to deorbiting times shorter than 4 *years*, it is possible to assume that, for these debris, the most suitable period to perform the deorbiting is actually represented by the latter one.

It is then worth to stress again that for a realistic mission, some of the target debris should complete their deorbiting phase within a high atmospheric density period, while others should have to be targeted and begin their deorbiting phase during a high atmospheric density period. The deorbiting phase would definitely last more than few years in some cases, but the deorbiting time provided by the medium density solution still represents a conservative result. Moreover, it is worth saying that similar analyses, carried out for the other two lists for the minimum and the maximum density scenarios, have shown the same tendency of the DISCOS list. For this reason, the following analyses, on the all three lists, are carried out only considering the medium density scenario (see Sec. 2.2).

For the sake of completeness, Figs. 31-32 show the same plots of Figs. 25-27 for a medium density scenario, taking into account the proprietary SSO and UCS lists described in Sec. 3. The same considerations drawn above can still be done even for these two cases, one more crowded and the other spatially more distributed.

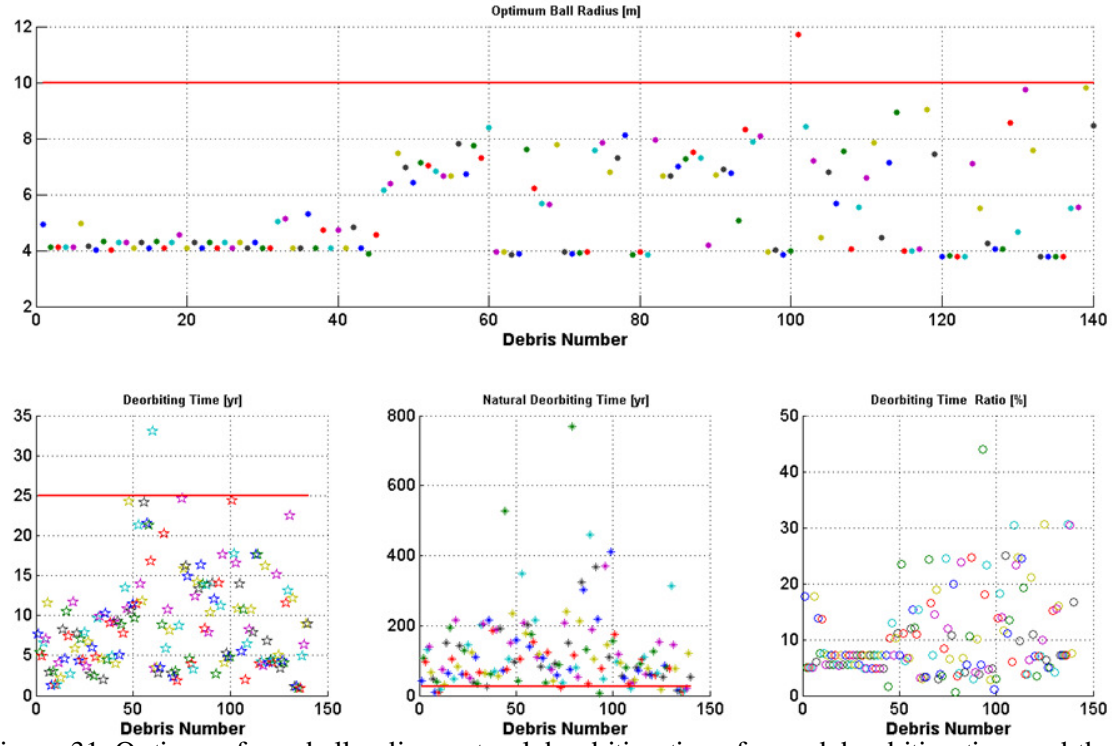

Figure 31: Optimum foam ball radius, natural deorbiting time, foamed deorbiting time and their ratio for the proprietary SSO list in the medium density scenario.

In both cases 10 *m* limit represent a reasonable assumption and almost all debris can be deorbited considering a radius below this threshold. Moreover, in the SSO list almost all debris can be deorbited within 25 *years*, while in the UCS one less than the 10% is beyond this threshold.

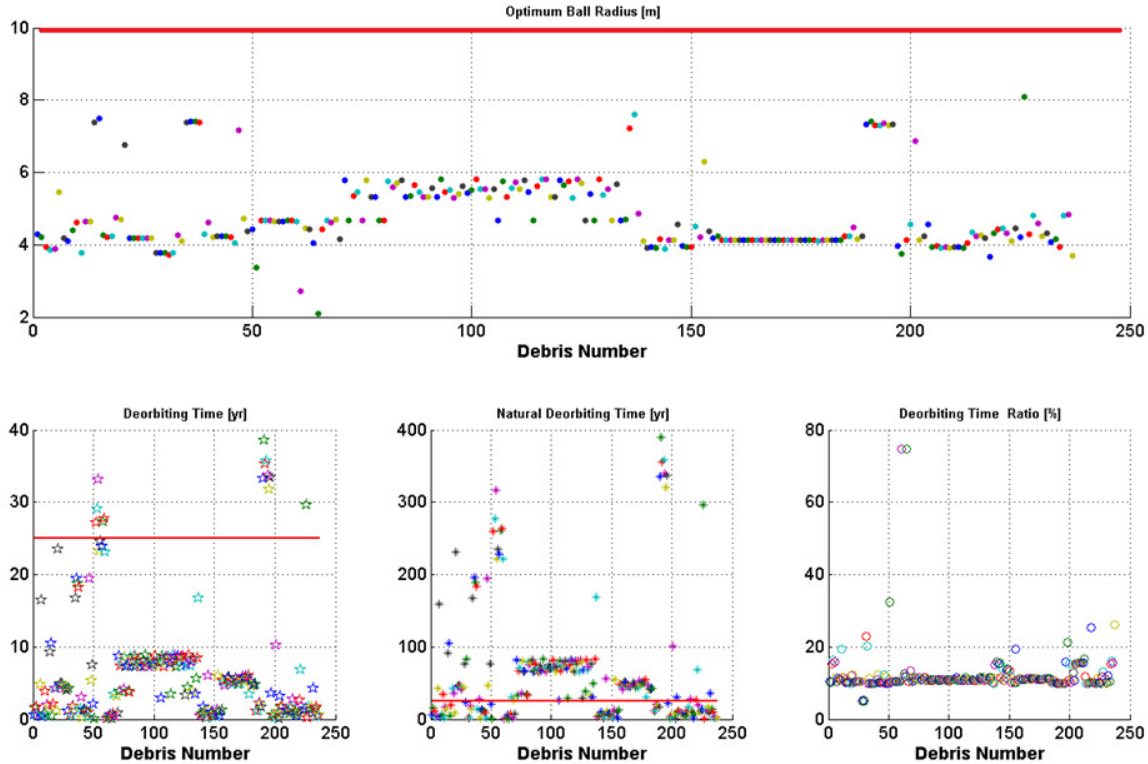

Figure 32: Optimum foam ball radius, natural deorbiting time, foamed deorbiting time and their ratio for the UCS list in the medium density scenario.

For the sake of completeness, in Fig. 33 also the impact probability for the proprietary SSO list in the medium density scenario is shown.

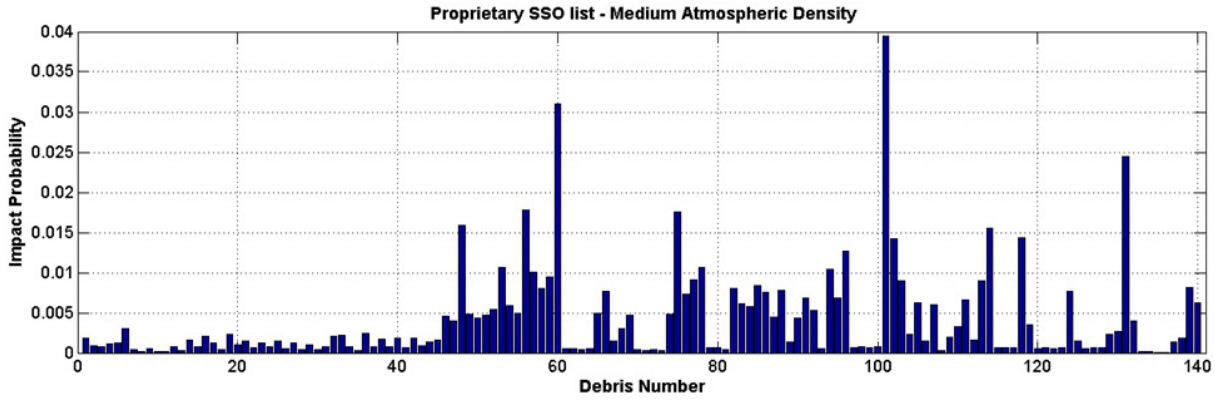

Figure 33: Impact probability for the proprietary SSO list in the medium density scenario.

In the same fashion of Fig. 29 and Fig. 33, Fig. 34 shows the impact probability for the UCS list in the medium density scenario.

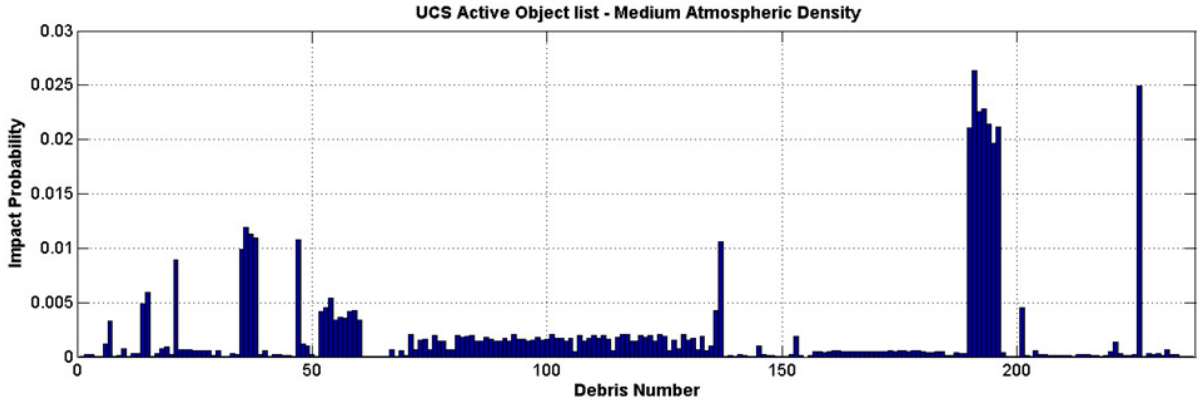

Figure 34: Impact probability for the UCS list in the medium density scenario.

Once again, for both the proprietary SSO and UCS lists, we can notice higher impact probability values for the heaviest objects.

In order to better understand the impact of the proposed approach on each debris and to identify in which cases this method provides major benefits for the mitigation of the debris population, some analyses are here reported considering the debris of all the three list described in Sec. 3 at once.

In Fig. 35, the optimum radii, calculated using the method described in this section, are plotted versus the debris mass. The red line in the plot is the same line of Fig. 21 and it is here presented to highlight the difference between the optimum radius obtained considering the impact probability (blue dots) and the theoretical value obtained by means of Eq.(16), where only the area-to-mass ratio is considered.

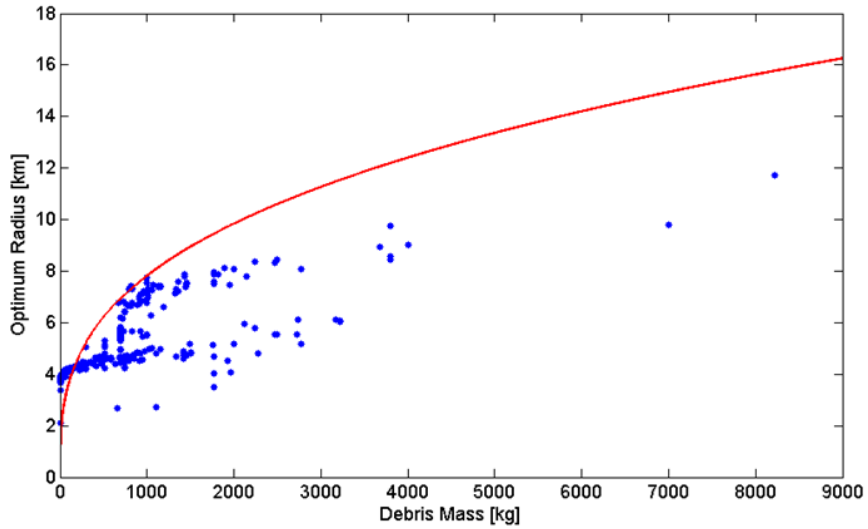

Figure 35: Debris mass vs. optimum radius. The red line represents the optimum radius value as function of the debris mass, obtained neglecting the impact probability.

It is clear that the deorbiting time estimated for the foamed debris can be further improved with respect to the values previously reported. Indeed the foam ball radius can be still increased in order to reach higher area-to-mass ratio, thus accepting higher impact probability. Some of the leftmost blue dots are not wrapped by the red line in Fig. 35. This happens due to the assumption of Eq.(15) about the initial volume of the debris. Indeed, this parameter has been taken into account for the analysis considering the impact probability, but it has been neglected to derive the analytical relation of Eq.(16) .

In order to complete this analysis, this section also provides several analysis and general considerations on the changing of the characteristics of all the debris listed in Sec. 3.1 after the foaming process.

From the plot in Fig. 36, it is possible to notice that high values of area-to-mass ratio, and accordingly small values of deorbiting time, can not be obtained for heavy debris.

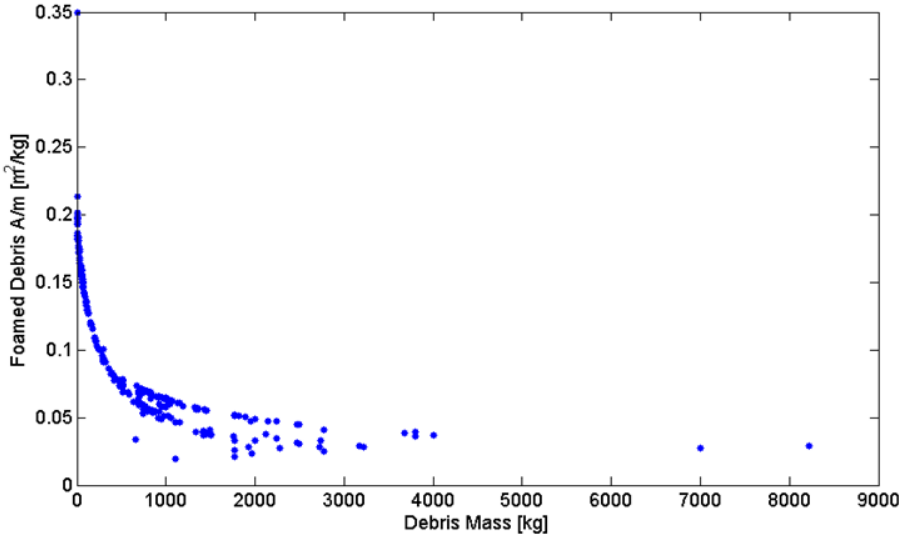

Figure 36: Debris mass vs. foamed debris area-to-mass ratio.

In particular, an area-to-mass ratio of 0.07, required to deorbit from 900 *km* of altitude within 25 *years* (see Sec. 1), is not obtainable for debris heavier than 1000 *kg*. As stated before, this result can be further improved increasing the optimum radius value so far considered.

Figure 37 shows the change in the area-to-mass ratio before and after the foaming process. As it is easy to observe, for growing values of the original area-to-mass ratio, the final value of this parameter does not keep growing. Indeed, as already stated, this method, as any other drag augmentation method, loses efficacy for those debris that already have a large value of the area-to-mass ratio.

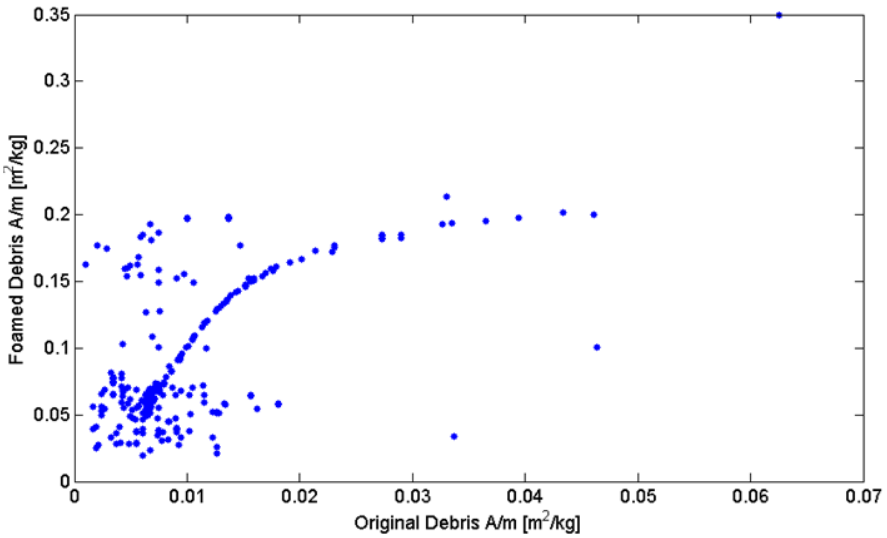

Figure 37: Original debris area-to-mass ratio vs. foamed debris area-to-mass ratio.

This behaviour is even more evident considering the plot of Fig. 38 where the foamed-to-original area-to-mass ratio is plotted versus the original one. After the foaming process, the area-to-mass ratio is increased up to 35 times for those debris with a small value of the original ratio. Looking at the right side of the plot, however, we can notice that this increase becomes smaller and smaller until it reaches values close to 1.

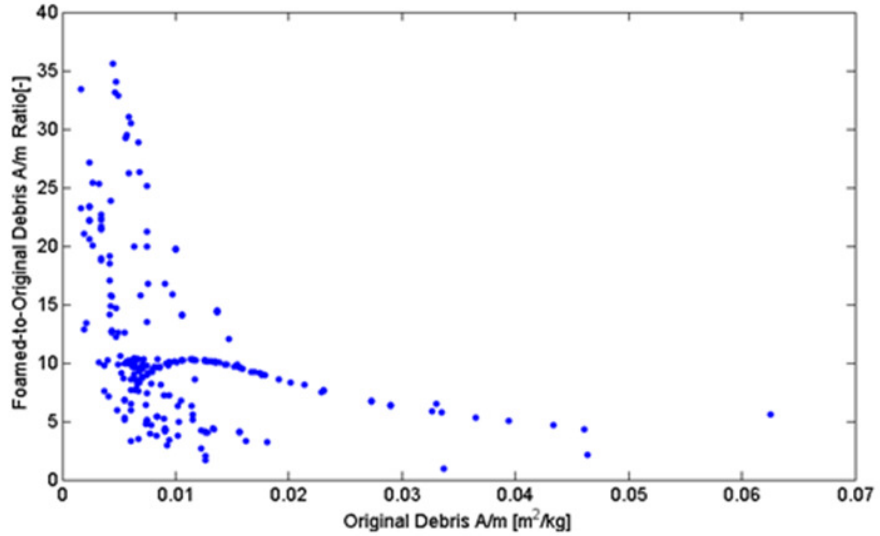

Figure 38: Original area-to-mass ratio is plotted versus foamed-to-original area-to-mass ratio.

Considering again the debris mass, we can see from Fig. 39 that also debris heavier than 1000 *kg* obtain major benefits from this method, since their deorbiting time is lowered up to 1/10 of the original one. For some debris, as already highlighted before, the method is actually useless since the deorbiting time is not effectively changed, but for most of them (90%) the deorbiting time is the 20% of the original one and the average ratio between the deorbiting time after and before the foaming process is about 12%.

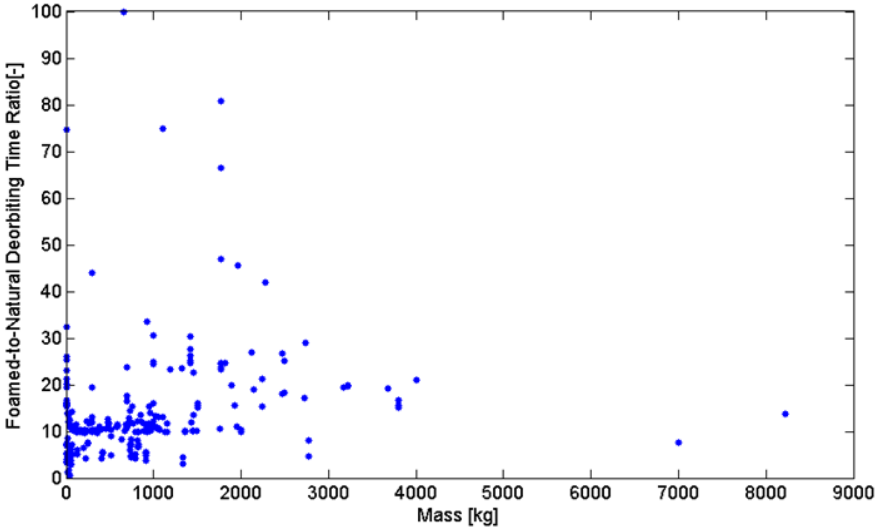

Figure 39: Debris mass vs. foamed-to-natural deorbiting time ratio.

The foamed deorbiting time values are shown in Fig. 40 with respect to the debris mass.

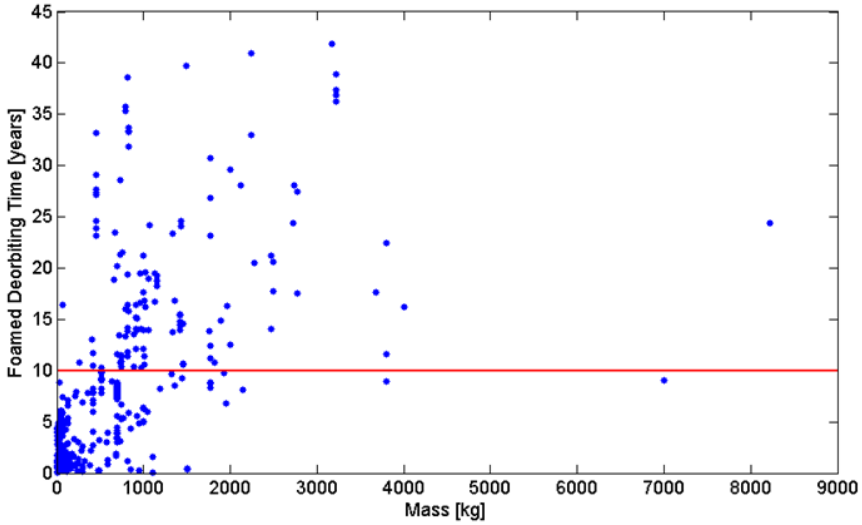

Figure 40: Debris mass vs. deorbiting time of foamed debris.

The red line shows a 10 *years* limit and the 71.6% of the total number of debris deorbits within this timespan. If we consider 25 *years* as a suitable deorbiting time, instead, we can see that the 91.6% of debris would decay within the given time assuming a realistic medium density model.

Furthermore, considering the deorbiting time of foamed debris with respect to the natural deorbiting time, see Fig. 41, it is possible to identify an almost linear relationship between these two quantities. The deorbiting time for most of the foamed debris considered is 1/10 of the original one. For many

debris, however, the increasing in the natural deorbiting time behaves more than linearly reaching up to 1/100 of the original time.

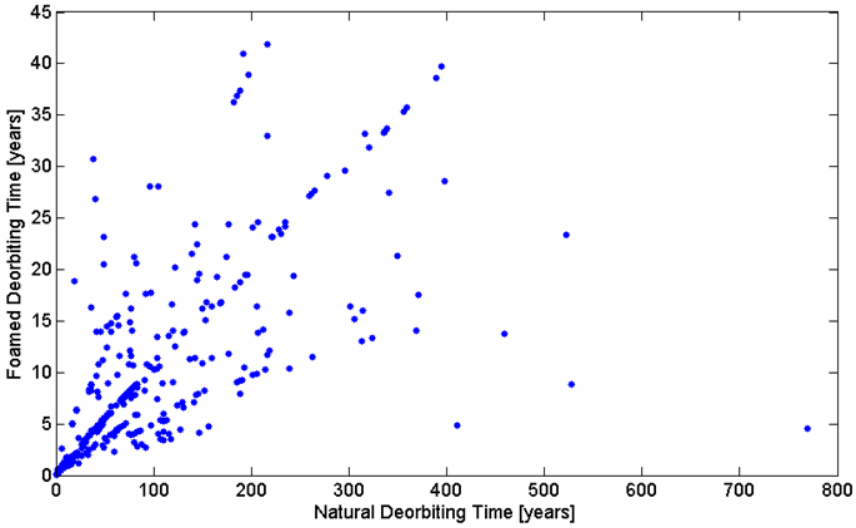

Figure 41: Natural deorbiting time vs. deorbiting time of foamed debris.

Considering the ratio of the two quantities plotted in Fig. 41 with respect to the initial orbital altitude of the debris, Fig. 42 shows the performance of this method in different space regions. It is actually reasonable to say that the performance of the method is not affected by the initial position of the debris. Most of the debris actually show values of the deorbiting time ratio around the 20% and since most of the considered debris lie in the 800 *km* of altitude region, those debris drifting away from this value are mainly placed in this region.

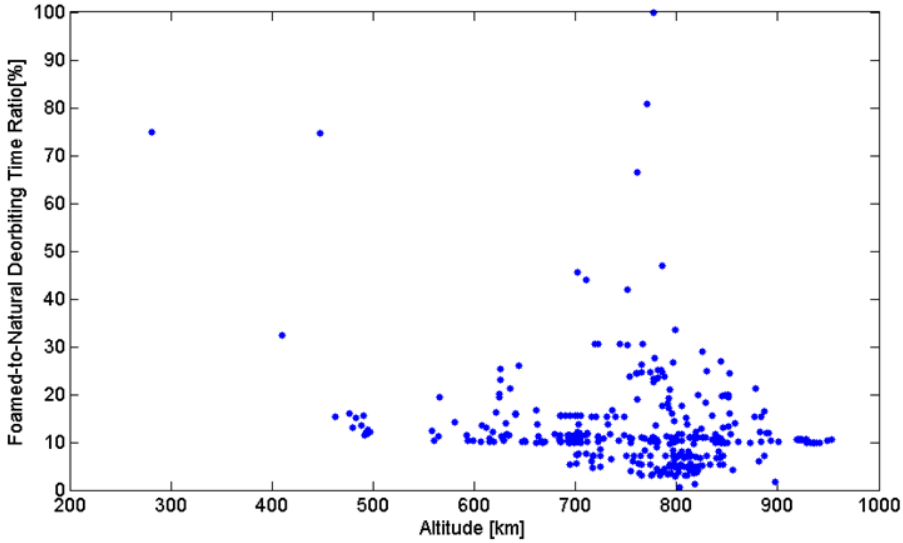

Figure 42: Orbital altitude vs. foamed-to-natural deorbiting time.

From the analysis of Fig. 43, finally, it is even more clear that the initial altitude of the object does not affect the achievable area-to-mass ratio value and that fast decays can be obtained also for debris up to 900 *km* of altitude. Once again, only the 6.3% of the total debris number does not deorbit within 25 *years* and these debris are all located between 750 and 950 *km*.

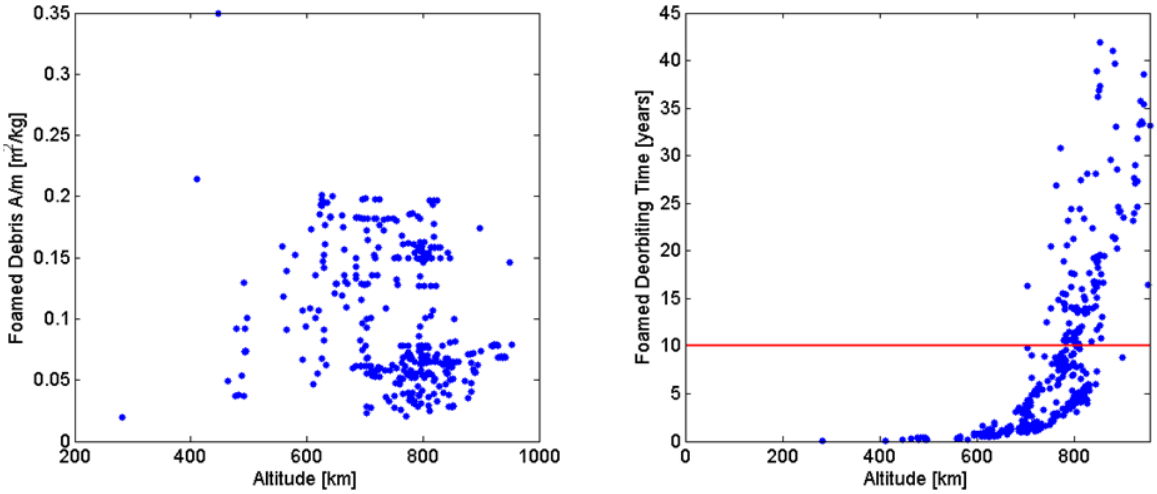

Figure 43: The left plot shows the orbital altitude vs. the foamed debris area-to-mass ratio. The right plot shows the orbital altitude vs. the deorbiting time of the debris after the foaming process.

All these analyses aim to highlight the effectiveness of this method considering the suitable size of foam balls and the corresponding deorbiting time values. Moreover, it has been shown that the proposed method, even if more suitable for debris with mass below 1000 *kg*, may be applied also to heavier objects, regardless of their initial altitude. It is worth stressing again that the foam density is the major parameter affecting all the obtained results.

5 FOAM GENERALITIES

After the general considerations on the active space debris foam-based removal mission scenario, let us focus on the key technological aspects of the proposed method. This and the two following sections are devoted to investigate about the main foam characteristics and to identify suitable candidates.

Foams can be considered biphasic materials with a firm structure enclosing hollow regions or gas bubbles. These regions are usually referred as *cells* to discriminate between the structure of the foam and the inflating component. There is a fundamental distinction between chemical foaming, where a special component starts the expansion, and physical foaming, wherein a gas or volatile liquid is added to the mixture [40].

The aim of this section is to provide an overview of the main foam characteristics, their composition and foaming processes. While Sec. 5.1 presents a brief summary of the state of the art of expanding foams used for ground- and space- based applications, the following sections deals with the main foaming phases and possible improvements of foam characteristics. The survey presented in this section aims to identify a suitable foam class whose main characteristics are pointed out in Sec. 7.

The great majority of available foams are tested in ground-based applications for thermal and acoustic insulations and light-weight applications. Expanding foams are substances able to increase their volume many times. There are foams able to expand up to 280 times [41] their original volume in atmosphere (1 *bar*) and, considering also foams with low physical consistency (e.g. fire fighting foams), expansion factor (the ratio between the foamed volume and the original one) values of 1000 can be achieved [42]. It has to be stressed since now that, in vacuum the expansion factor for the already available foams increases as the outside pressure is zero. Foam physical and chemical characteristics, as surface tension and viscosity, also represent driving factors for the expansion of the foam cells, that have to be able to contain all the gas chemically produced or mechanically introduced (see Sec. 6).

Solid foams have outstanding low weights as the larger part of their volume consists of gas, while the rest is solid material incorporating structural elements. They have high strength and loadability if compared to their small mass and density. Solid foams can be used as thermal and sound insulators, energy absorbers, as fire retardant and extinguisher [43]. Industry interest in this kind of structures also reflects in some experiments about foam utilization in space, such as the Admatis Ltd. Experiment on FOam Casting and Utilization in Space (FOCUS) conducted in February 2010 on board of the European Columbus laboratory module of the ISS [44].

Different foams have been used in space over the years for cladding the payload section in the nose cone of the Ariane 5 launcher rocket. This protects delicate satellites from the high acoustic pressure exerted on the rocket during the start-up phase [45]. Solimide polyimide insulation foams have been adopted in the construction of the Space Shuttle fleet. In the beginning, the Space Shuttle used foam for standard thermal insulation, packaging and protecting fragile equipment. Since solimide foam remains flexible and resilient, despite the strong temperature swings of the space environment, it has been also used for cryogenic insulation of fuel tanks on major rocket propulsion systems [46].

For the sake of completeness, there is at least a further foam type that has been used in space missions, like Mars Pathfinder [47] and Stardust [48], and that has been recognized as the solid with the lowest density nowadays available: Aerogel [49]. Aerogel is not like conventional foams, but is

a special porous material with extreme microporosity on a micron scale with many unusual properties, such as low thermal conductivity, refractive index and sound speed, in addition to its exceptional ability to capture fast moving dust [49].

5.1 Foam Classes and Characteristics

Foams characteristics are extremely various and wide-ranging due to the different nature of the various substances that may form their gaseous part as well as their liquid or solid part. For this reason, industry demonstrates growing interest for the exploitation of advantages provided by foam structures.

In general, bubbles are created into a viscous mixture at pressure, during the foaming process, higher than the external one. In these conditions the pressure difference acts as the driving force for the expansion. However, the fluid viscosity and the reaction time for the polymerization have to be such that bubbles remain trapped into the mixture not flowing outside. One of the most important characteristic classifying foams, indeed, is the structure of its cells. There exist *closed-cell* foams, in which an insulating gas is retained within the cells, and *open-cell* foams [50]. The foam nature is crucial also for the selection of the deorbiting foam here sought as their use in vacuum may be strongly influenced by this characteristic. Closed-cell foams usually exhibit higher rigidity and strength but this mainly depends on the resin resistance to the outer environment (and interior-exterior pressure difference, see Sec. 6). On the contrary, open-cell foams are not particularly affected by this problem but their mechanical properties are typically reduced by the absence of their own interior gas.

As mentioned, the most important characteristics classifying specific foam is the structure of its cells. The two main classes can be detailed as follows:

- In *closed-cell foams*, gas is retained within the cells. This means that the decomposition of the blowing agent remains inside the foam acting as insulating gas. Insulation can be measured by means of the *R*-value indicating the resistance to the heat flow [50]. Closed-cell foams have very high insulating characteristics. Furthermore, the close structure of cells results in high effective air barrier, low moisture permeability and excellent water resistance. These foams are characterized by a good rigidity and strength.
- In *open-cell foams*, cell structures are not closed and the gas does not remain trapped into the foamed structure. These foams are lighter than the closed-cell ones; in particular they have a lower density that corresponds to a higher yield. Thermal insulating properties of these foams are lower than the one of closed-cell foams and are more permeable to moisture vapour and water. Open-cell foams are more effective than closed-cell foams as sound barrier. They have a soft appearance and a lower rigidity and strength with respect to closed-cell foams.

In brief, open-cell foams present interconnected bubbles, while closed-cell foams are characterized by spatially separated bubbles. Some (and for sure not exhaustive) characteristics of these two kinds of foam are summarized in Tab. 6:

Closed-cell	Open-cell
Low vapour permeability	**High vapour permeability**
Good water insulating	**Good sound insulating**
Medium density	**Low density**
High strength and rigidity	**Low strength and rigidity**

Table 6 Comparison of closed-cell and open-cell foam characteristics

These considerations led to focus our choice, in general, on open-cell foams which may be easier to obtain in vacuum [15]. Furthermore, for the application here considered, open-cell foams represent the best choice, in particular due to their expansion factor, larger than the one of closed-cell foams and their typically lower density value [51].

5.2 Foam Kinds

A further foam classification deserves special attention. In this section foams are classified according to the material they originate from. This criterion is fundamental in order to select the specific foam kind for the deorbiting application. Based on this criterion, foams can be classified in:

- *Glass Foam*s are commercially available since the first half of the 20th century. They can be either made from molten glass or from sintered glass particles. Their structural properties are excellent and are maintained for long time, thus they are suitable (and mainly used) for insulation purposes. The basic manufacturing principle to produce this kind of foams is to generate a gas into molten glass at a temperature between 700 and 900 °*C* [52]. The gas expansion forms bubbles that, remaining trapped into the glass, produce a structure of cells and hence a porous body, see Fig. 44.

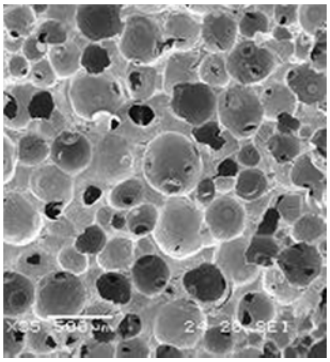

Figure 44: Microscopic structure of glass foam [53].

Depending on the initial state of the glass used, a foaming agent may be required. Typically, the use of sintered glass particles requires the heating of a mixture of sintered glass particles and foaming agent [52]. During this phase the glass powder melts and the foaming agent decomposes producing gas. Accordingly, the bubbles, if the fluid has sufficient viscosity, are captured during the foaming process. The temperature change rate is a critical aspect for the glass foam production as well as the temperature uniformity. If the temperature is too high, bubbles will rise and the body will collapse do not forming foam bodies [54].

Suitable foaming agents can be calcium sulphate ($CaSO_4$) or calcium carbonate ($CaCO_3$). Depending on the selected foaming agent, there will be production of sulphur gases from $CaSO_4$, or CO_2 from $CaCO_3$. In particular, gypsum and limestone are the most available source of $CaSO_4$ and of $CaCO_3$, respectively. The foaming agent particle size affects the cell dimension [55], influencing performance and characteristics of glass foams and in turn the density of the product. The density of glass foam is a typical factor determining its quality; the lower the density, the lower the thermal conductivity of the product. Furthermore, the smaller the cell size, the higher the compressive strength.

The brittleness that characterize glass, and as well glass foams, makes this kind of foam unsuitable for our application.

- *Ceramic foams* are porous materials that consist of polyhedral cells (see Fig. 45), with average linear dimension ranging from 10 μm to some *mm*. Current commercially available ceramic foams include compositions such as alumina, zirconia, cordierite, mullite, silica, silicon carbide and hydroxyapatite [56].

  Depending on their morphology (e.g. open- or closed-cells, pores size and their distribution), ceramic foams can be used as filters, catalyst support, reinforcement for metal matrix composites, thermal protections systems, supports for space mirrors, heat exchangers (graphite foams) and so on.

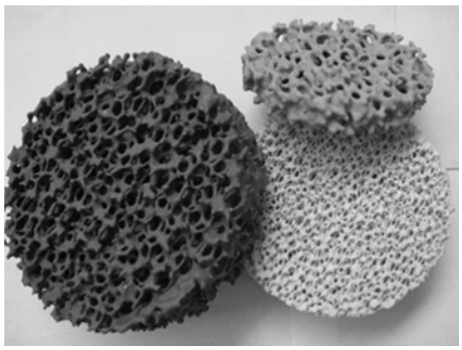

Figure 45: Ceramic foam samples [57].

This wide range of utilizations is mainly due to their high melting point, adjustable electronic properties, high corrosion and wear resistance together with the mechanical and physical characteristics gained through the foaming process. These characteristics are usually coupled with low density, low thermal conductivity and high specific strength.

Currently, there are three main manufacturing processes to fabricate ceramic foams [56]. One of these uses polymeric foams as mould to obtain ceramic foams, impregnating a cellular structure by a ceramic suspension of appropriate viscosity. The polymeric foam is removed in a second step. A different technique is based on the preparation of a continuous ceramic matrix where a second phase is continuously dispersed and has to be burned-out to give the final porosity. The last method (direct foaming) uses a blowing agent as volatile liquid, combustible solid particles or the gas produced by reactions (or eventually added), to generate the ceramic foam mixture. A high temperature sintering may occur at the end of the process to obtain better mechanical properties. The porosity of the foam at the end of this process is proportional to the amount of gas blown into the suspension during the foaming process, while the pores size depends on the stability of the mixture.

Since the wet foam is a thermodynamically unstable system (where bubbles grow and coarse), the most critical issue in direct foaming processes is the stabilization of gas bubbles in the initial mixture. Stabilization can be performed using surfactants (compounds lowering the liquid surface tension) like long-chain amphiphilic molecules. This approach presents the main disadvantage to have absorption energy of surfactants at the gas-liquid interface, so their use requires a setting agent to consolidate the foam microstructure [56]. This method probably gives the widest range of cellular structures and hence physical and mechanical properties [56].

Ceramic foams definitely do not represent a suitable candidate for our purpose since their manufacturing process could represent the major issue for the application in space environment.

- *Metallic foams* are rigid metallic structures containing a large fraction of gas, see Fig. 46. These materials are structurally similar to polyurethane foams, although the mechanical properties of the basic metals make these foams stiff and excellent for energy absorption. Typically these foams retain most of the physical characteristics of the original material, but they have very low specific weight.

  Such foams are obtained mixing the blowing agent with the powdered metal, then pressing and heating the blend up to the metal melting point [58]. The selection of the blowing agent is chosen according to the release of gas at a temperature close to the metal melting temperature, so that the

foaming may occur immediately before the cooling. The sample is immediately chilled to trap this foam structure into the solid state. This usually results in closed-cell foams. There are also other techniques that might lead to open-cell structures [58].

Figure 46: Metallic foam sample [58].

Microgravity experiments have been conducted on metallic foams to understand its behaviour in space environment [59] and to develop a new high strength metal foam materials for space applications [60]. Nevertheless, for the particular application here considered this class of foams seems to have, in general, too high mechanical properties (not really required), too large weight and too low expansion factors.

- *Polymeric Foams* present the significant advantage that almost every polymer can be used to produce foam with good mechanical properties and low price. The selection of a specific polymer depends on the desired application and can result in a rigid or flexible foam. Elastomers result in flexible foams, while glassy polymers produce rigid foams. The foaming process starts from the mixing stage, where the two (typically) foam components are mixed together. Hereafter the bubbles start nucleating within the slurry and growing within [43]. When the polymer dividing the bubbles is reduced to a small film, bubbles start to coalesce and change from being almost circular to polyhedral form. In the end, the curing stage takes place where the foam petrifies due to the completion of the polymerization process [43]. Usually the nucleation gas is dissolved into the components and the total amount of gas dissolved depends on the pressure, the duration of the process and the surface diffusion of the liquid. During this step the gas nuclei generates. This aspect could be rather problematic when the outside pressure is very close to zero, possibly requiring a controlled atmosphere for the nucleation process. Considering current foams, non ad-hoc developed for space applications, the selection of such foams would also impose constraints on the foam nucleating device (see Sec. 9).

  The most common polymeric foams, combining excellent mechanical and physical properties with a rather simple production process, can be classified as:

  - *Polyurethane foams* includes a large number of polymers formed through the polyaddition of polyfunctional isocyanates and reactive polyfunctional compounds [50]. Polyurethanes are the most versatile polymers with a number of different forms, ranging from lightweight rigid foams to soft flexible foams and even dense solid compositions. Polyurethane is obtained through the chemical reaction between di-isocyanates and glycols, supplied as polyesters or polyethers [50]. Polyurethane was developed by Bayer in Germany in 1937, and later in the United States in 1953 [50]. It is formed by a two-part liquid mixture that uses monomer solutions mixing to produce foams. One of components of the mixture consists in a polymeric diol or triol, a blowing agent, a surfactant and a catalyst mixed with the polyisocyanate. All of these components are required.

    Upon mixing, a polymerization reaction occurs in three directions, leading to a large molecule that is rigidly held into a three dimensional structure. At the same time a small amount of water, usually available within one of components of the mixture, reacts with the isocyanate resulting in the release of carbon dioxide (CO_2), which causes the foaming. The blowing agent, a low boiling liquid, is vaporized by the heat of the reaction and along with the carbon dioxide creates gas bubbles into the viscous mixture as the foam sets into a rigid mass. The cell size and structure of the foam is controlled by the silicone surfactant.

    The reaction between isocyanate and water, running parallel to the urethane reaction is represented in Fig. 47 together with a generalized polyurethane reaction scheme [61].

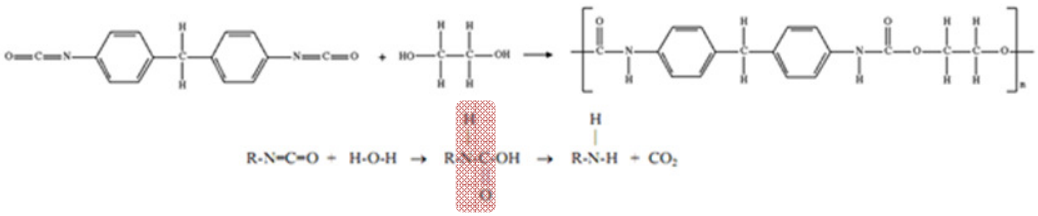

Figure 47: Typical reaction scheme of polyurethane and gaseous carbon dioxide formation. The urethane group is highlighted in the shadowed rectangle [61].

At the end of this bubble formation phase, bubbles grow, coalesce and the mixture is confined by thin films among them, keeping the bubbles inside the mixture. During this step also several stabilization reactions take place. The balancing among bubble growth, reaction progress and stabilizers determines the open-/closed-cell foam structure. A mismatch among these factors can cause or the collapse of the foam, due to the rupture of the cell membranes, or, for a closed-cell structure, a not completely expanded foam, as the cell membranes are over stabilized.

In order to obtain rigid foams, polyester with a short but highly reactive chain and a physical foaming agent have to be mixed [40,61]. At this level of analysis, this kind of foams seems to be the best candidate for our application due to its reasonably high expansion factor (typically), flexibility and its relatively simple production.

- *Polyethylene foams* are obtained by foaming polyethylene. Polyethylene, as any other polymer, is composed of a long monomer (-CH_2-) chain first accidentally synthesized by Hans von Pechmann in 1898 while heating diazomethane [62]. So, the term polyethylene describes a huge family of resins obtained by polymerizing ethane molecules. The general shape of such a molecule is shown in Fig. 48.

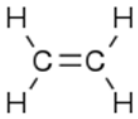

Figure 48: Ethene molecule, the fundamental chemical group of polyethylene foams.

Polyethylene is, so far, the largest volume commercial polymer and it can be formed by a wide variety of thermoplastic processing methods. It is particularly useful where moisture resistance and low cost are required and it can have both low and high density.

Reactions causing the foaming of this class of materials are very similar to the ones described for polyurethane foams. The ethylene converts to ethane taking its place in the polymeric chain. In this case, gas can be introduced by means of a blowing agent. This agent can be of chemical nature (e.g. sodium bicarbonate, $NaHCO_3$) and it is typically a material with low decomposition temperature. During the decomposition a large amount of gas is released into the mixture. However, the blowing agent can also have physical nature (e.g. hydrocarbons). In this case the polymer is physically blended with a blowing agent (and additives) at high temperatures. Polyethylene foams have a wide density range. Accordingly they can be classified as [63]:

- high density polyethylene foams: [0.5, 1] g/cm^3
- medium density polyethylene foams: [0.1, 0.5] g/cm^3
- low density polyethylene foams: < 0.1 g/cm^3

This last category, in particular, presents a gas-to-polymer volume ratio larger than 10 [63].

- *Polystyrene foams* are the result of foaming processes on polystyrene resins. Polystyrene is a linear polymer of styrene, see Fig. 49, whose conversion is energetically very favourable and occurs spontaneously on heating without the addition of initiators or catalysts [64].

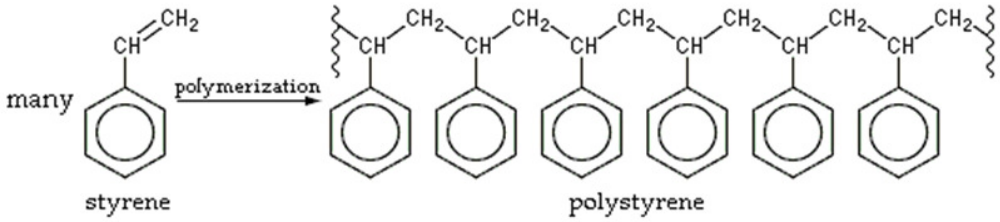

Figure 49: Monomer (left) and polymeric chain (right) of the polystyrene molecule [64].

Addition of butadiene-based rubbers increases impact resistance and copolymerization of styrene with co-monomers such as acrylonitrile or maleic anhydride producing plastics resistant to heat and solvents [64]. An extremely wide performance range can be achieved by using various styrene plastics. Within each group, additional variations can be expected. In order to obtain other properties and specific polymer behaviours for a given application, an appropriate resin must be chosen during fabrication.

Polystyrene foaming beads were developed in the 1950s by BASF under the trademark of Styropor [64]. These beads are made by suspension polymerization in presence of blowing agents such as pentane or hexane, or by post-pressurization with the same blowing agents. Two completely different production systems are based on extrusion of styrene chains and lamination, producing foam sheets. The physical characteristic of the resulting styrene-based foams are heavily affected by the production process. Several typical physical properties of polystyrene foams, classified according to the production process, are listed in Tab. 7.

	Styrofoam Extruded	**Beadboard-molded**	**Foam Sheet**
Density [kg/m^3]	35	32	96
Compressive Strength [*kPa*]	310	207-276	290
Tensile Strength [*kPa*]	517	310-379	2070-3450
Flexural Strength [*MPa*]	1138	379-517	-
Thermal Conductivity [*W/mK*]	0.030	0.035	0.035

Table 7 Some relevant polystyrene physical characteristics [64].

In particular, polystyrene foamed products are the result of polystyrene resins containing few percentage points of blowing agent. The styrene monomers polymerize and then the beads are impregnated with the blowing agent [64]. An agitator mixes the styrene monomers with water controlling pressure and temperature of the slurry. After the process, a dewatering process is required to obtain, usually, expanded polystyrene rigid foams. This plastic material has closed-cell structure and low density (around 0.02-0.05 g/cm^3). In normal conditions such foams can expand up to 40 times their volume [65]. Given their typical internal structure, this kind of foams does not represent a suitable candidate for our purpose.

- *Polyvinylchloride foams* are the result of gas inclusion into polyvinylchloride resins. Polyvinylchloride (PVC) is a polymer prepared from vinyl chloride monomers. The chemical structure of such monomers is shown in Fig. 50.

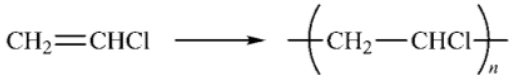

Figure 50: Polyvinylchloride monomer before (left) and after (right) the polymerization process

Its relatively low price and the wide range of possible applications make PVC one of the most versatile commercial polymers. Due to the wide range of PVC polymers commercially available, it is not easy to give a precise description of its properties. PVC is never used alone and each possible additive, as well as its molecular mass, influences the final characteristics of the polymer. In particular, flexible PVC and plastisols [66] are produced by the addition of plasticizers during the polymerization process. Plastisols, commonly called pastes, are dispersions of PVC powders in plasticizers [66]. As no plasticizer can satisfy all the desired properties, several plasticizers are usually mixed up to obtain the final product. Moreover, blowing agents such as azodicarbonamide have to be added for foamed PVC production [66].

Also in this case the basic principles of the foaming process are the same of previous polymeric foam kinds. The foaming agent is usually carbon dioxide that represents the gas trapped into the foam bubbles. The mechanical properties of the resulting foam are quite various depending on the specific plasticizer added. Its specific weight is low (almost one half of solid PVC) although the structure is very rigid, high resistant to moisture and easy to manipulate [66,67].

From this excursus on foam classes, it is clear that polymeric foams offer the best combination of characteristics for the considered application. While glass and ceramic foams are fragile, not particularly light and not broadly adaptable acting on the foaming process, the metallic foams are too heavy and with mechanical properties not required for deorbiting purposes. Polymeric foams, and in particular polyurethane foams, are thus selected as the foam class candidate for the foam-based debris deorbiting system. This specific class is chosen due to its reasonably high expansion factor (typically), flexibility and its relatively simple production.

Before moving forward with the polymeric foam discussion, let us briefly describe the other fundamental component to obtain a foamed body from a solid material. Additives are required in almost every kind of foaming process, regardless from the foam kind and the resulting structure. The final physical and chemical characteristics of the foamed body are highly dependent from the specific additive considered. Additives can be classified in two main classes:

- *Foaming (blowing) agents* are inorganic or organic additives that produce a foamed structure [68]. They are extensively used in PVC, polyethylene, polypropylene and polystyrene production processes, in order to improve properties and appearance as well as to reduce weight. Blowing agents can be classified as either physical or chemical. Physical blowing agents are volatile liquids or compressed gasses dissolved in the polymer changing state during the cellular structure formation process. Chemical blowing agents decompose thermally to liberate gasses that form a foamed product [68].
- *Impact modifiers* act by absorbing the impact energy and dissipating it. They are typically represented by elastomers added to a wide range of thermoplastic materials at levels up to 20% [68]. The major types of impact modifiers are acrylics, styrenics including methacrylate–butadiene–styrene copolymers and Acrylonitrile-Butadiene-Styrene [68].

5.3 *Polymerization and Curing*

As previously mentioned in this chapter, gas molecules can be dispersed in the polymeric matrix by dissolution in the molten state, or by reaction within the polymer before, during or after polymerization. Thus, gas formation within the polymer is a necessary condition for foaming, as well as the polymer capability to hold gaseous bubbles, until a stable structure is obtained. Polymer properties and strength are the governing aspect for high expansion ratio foams, as the ones sought for the deorbiting application.

Too high polymeric strength, indeed, could cause restrained expansion although a fine celled structure can be established. On the contrary, polymer weakness could lead to quick over expansions or bubble ruptures. In these conditions, an acceptable expansion may occur, but, due to the poor material strength, foam shrinking will certainly follow. The balancing between polymeric strength and gas/melt ratio is thus fundamental to obtain expanded foams. The possible combinations, together with the ideal region (shadowed), are shown in Fig. 51.

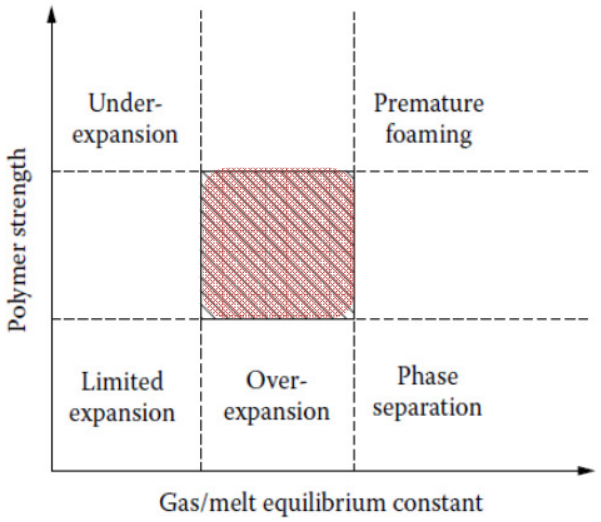

Figure 51: Possible and suitable (shadowed region) polymeric strength and gas/melt equilibrium combinations [50].

The processes driving the foam expansion are, indeed, the polymerization of the solid part of foam and its curing. Polymerization is the process that involves a huge quantity of monomers reacting to produce a polymer molecule chain. During the curing phase, polymer chains start to bond by cross-linking, thus giving the firm part of the foam.

Polymers may be synthesized according to two major kinetic schemes: *chain* and *step* polymerization. The most important approach for chain polymerization methods is the free radical polymerization [69]. It requires free radicals, derived by thermal or photo-chemical decomposition of unstable materials. This method is composed of three major kinetic steps: initiation, propagation, and termination. The initiation step usually includes the addition of the first monomer molecule then, on heating, one of the components of the reaction decomposes to give free radicals that attack the monomer and add to it. After initiation reactions, many monomer molecules are added rapidly moving the free radical to the end of the chain. In the termination reaction, two free radicals react with each other closing the chain [69].

The second important kinetic scheme is the step polymerization. The essential polymerization step is a repetitive free radical addition to the monomer double bonds, forming chains constructed of units linked together predominantly head-to-tail. This linking only requires that the appropriate functional groups meet in space.

Bubble nucleation and growth are essentially unstable processes pointed to a new equilibrium state, while the contiguous polymer is in charge of the stabilization of the process.

At the end of the foaming phase the hot, or even molten, polymer cools down into a stable solid phase. Cooling is the natural way to enhance material strength and, since polymers and gaseous phase are poor heat conductors, it can take seconds to days until a thermal equilibrium between the foam and the outside environment is reached.

As soon as cooling begins, the equilibrium between internal and external pressure is achieved so that the blowing gas contained in the foam cells could start to permeate outside the polymeric membrane with no significant effects on the cell volume. The completion of this phase can occur later than the solidification itself, depending on the permeability of the blowing gas [50].

In this context, polymers can be further categorized with respect to their behaviour during thermal variations as *thermoplastics* or *thermosets*. Thermosets polymer chains form a not too long thermo-reversible network structure when exposed to high temperatures. In thermoset foams, the material strength is established by virtue of completion of polymerization and cross-linking. Since inter-polymer bonds are developed, thermoset foams can allow excessive expansion to create open-cell structure without causing concerns with regards to dimensional stability [50]. The thermoplastic family of polymer has a thermally-reversible morphology. This behaviour is due to the long-chain held by the interpolymeric coiling and the van der Waals force.

5.4 Composite Foams

In the recent years, the industrial attention towards increasing foam potentialities focused the research on the development of composite foams. Composite foams, unlike conventional single-phase foams, are composed of a phase with voids and an additional dispersed solid or hollow phase. The presence of additional solid constituents may enhance certain specific properties of the foam such as stiffness, strength, electrical or thermal conductivity and so on [70].

It is worth stressing that, beyond the identification of a particular foam kind, the development of an ad-hoc composite foam could enhance method capabilities due to the possibly improved foam characteristics. For this reason, a brief overview of composite foams peculiarities is here given, whether in the following sections a simple polymeric foam is chosen for the candidate foam identification.

Composite foams can be categorized in *syntactic foam, particle-reinforced foam,* and *fibre-reinforced foam* [70]. Syntactic foams are particle-reinforced foams with an hollow dispersed solid phase aimed at reinforcing the material. These spheres, ranging in size from less of a micrometre to few millimetres, may consist of glass, carbon, metal, polymer, or ceramic materials and they can be mixed in a polymer either in liquid or in solid powder form. More precisely, composite foams may be processed in few ways: by the introduction of gas, mixing or using a physical or chemical blowing agent, by a sacrificial cell-forming material, or by bonding together spheres, powders or fibres. Each of these methods intentionally introduces voids in the finished material giving different

voids size and distribution, the resulting in different material properties. The gas introduction into the composite material during the curing or solidification phase, may be easier for thermoset materials in which it is easier to control the degree of cure while, in the case of a thermoplastic, the temperature during the foaming process has to be accurately managed [50]. In case of an added physical blowing agent, this undergoes vaporization during the polymerization phase and then it dissolves into the polymer material under high pressure, coming out from the solution and blowing the foam at pressure release.

Chemical additives to polymers or gaseous phases, as reaction products, allow a blowing of the foam similarly to the physical blowing case. These agents evolve from a cross-linking reaction, and then the careful control of the reaction kinetics is required in order to avoid foam to overblow and collapse, in case the resin does not have a sufficient viscosity.

The addition of voids into the material may also occur through mechanical mixing or stirring. This easy method turns out to be very difficult to control so as to obtain a desired type, size, distribution, or volume fraction of voids [71]. The inclusion and then removal of sacrificial material ensures cell size uniformity; however, a very high volume of material must be introduced and a reasonable time period has to be accounted for removal of the sacrificial material.

The last method of composite foam production is based on the bonding of spheres, powders, and fibres within the foam. These syntactic foams can consist of two, three or four phases coexisting into one single foam. Indeed, a two-phase foam microstructure only has the polymer binder and the hollow microspheres while, in a three phase material interstitial voids fill the spaces between microspheres constituting the third phase. Fibres can then represent the fourth constituent in the composite foam.

6 FOAM EXPANSION MODEL

The aim of this section is to define a low order analytical model to estimate the final foam characteristics at different external pressure levels. The main characteristics to take into account are the final foam volume, its porosity and density and then the corresponding expansion factor. Also the stickiness of the foam is a fundamental aspect to be considered and it is addressed in Sec. 11.3, considering commercial polymeric resins, to size the minimum foam-debris contact area.

Before starting with the description of our model, a short survey of available standard software is given. These are usually too complex and specific for our first order analysis, thus we developed a low order model. Several commercial simulation software dedicated to polymer application, as well as several multi-physics codes, are able to model the foam expansion process. *Comsol*, *Ansys* and *Nastran* are just the best-known ones but, for specific industrial purposes, dedicated codes still seem the best option.

Among these, the *REM3D* [72] code has to be mentioned. It is built from the *CIMlib* library [72], based on the finite element method [72]. In general, all *CIMlib* solvers include also a mixed solver for Navier-Stokes equations with compressibility and viscoplasticity, a mixed Galerkin solver for the heat transfer equation and a discontinuous Galerkin solver for the transport equation [72]. These libraries use 3D tetrahedral, linear and unstructured elements, only one mesh for all the simulation parts, an Eulerian kinematics with a R-adaption of the initial mesh, which remains the same during the process and a space-time formulation [72]. Furthermore, this software is able to simulate, predict and optimize many industrial processes, like extrusion and injection moulding for polymers, all multi-domain versions of extrusion and injection moulding like co-extrusion, co-injection, gas or water assistant injection, over-moulding, fibre reinforces injection and, in general, other multi-domain processes, as casting or polymer foam expansion [73]. It is worth noting since now, that a reduced order model very close to the one here developed has been also validated by means of the *REM3D* exploiting a numerical method implementation for the expansion of a gas bubble into a pseudo-plastic fluid [73].

Other software able to simulate the foam expansion process are *SurfaceEvolver* [74] and *Ximex* [75]. *SurfaceEvolver* is an interactive program that minimizes the energy of a surface, implemented as a simplicial complex, subject to some constraints [74]. The energy can be represented by surface tension and gravity related energy, knot energies and many others; while constraints are typically geometric constraints. The code evolves the surface by gradient descend method [74]. Some applications of *SurfaceEvolver* include modelling the shape of fuel in rocket tanks under low gravity conditions, computing capillary surfaces in cubes and in exotically shaped containers, simulating grain growth, studying polymer chain packing, and so on [74]. Furthermore, this kind of code is even able to simulate diffusion processes [74]. *Ximex* is a 3D software for computational fluid dynamics which also reproduces extrusion and mixing process [75]. This software models the integration of virtual particles in the material and quantifies the dispersive/distributive mixing: its density, average distance between two particles and particles size [75].

Using these simulation codes, it would be possible to study the foam evolution behaviour, but for our purposes, a first approximation of the expansion phenomena is sufficient, thus we developed an analytic model describing the foam growth. In order to evaluate the foam expansion performance, we consider the foam as composed of a polymeric matrix and an expanding gas (blowing agent). This gas is developed by the reaction between the two components and it fills the bubble nuclei inflating the total foam volume. At the same time the polymeric matrix polymerizes fixing the bubbles into it.

6.1 The Analytical Model

The foam can be modelled as a whole bubbly fluid where a set of bubbles are dispersed into a (semi)-solid matrix [76]. In this model the foam (subscript *f*) is supposed to be composed of two components, the polymer (subscript *p*) and the gas (subscript *g*). The gas is always supposed to be a perfect gas.

The number of bubbles is given by the bubble concentration per unit of polymer volume, n_B, multiplied by the volume of polymer, V_P. In equation:

$$N_B = V_P n_B \tag{20}$$

The volume of polymer per each bubble is given by the ratio between the polymer volume and the number of bubbles:

$$V_{PB} = \frac{V_P}{N_B} = \frac{1}{n_B} \tag{21}$$

The volume of foam, after the expansion, will be approximately equal to the total volume of bubbles (as the polymer contributes principally in mass rather than volume), thus:

$$V_F \cong V_G = N_B V_B \quad \Rightarrow \quad V_B \cong \frac{V_F}{N_B} \tag{22}$$

Moreover, the total mass of gas and polymer can be computed by the density and volume of both:

$$m_G = V_G \rho_G \cong V_F \frac{p_G}{R_G T_G} \tag{23}$$

$$m_P = V_P \rho_P \tag{24}$$

These general relations would lead to a multi-phase fluid, rather hard to modelling, but the same conclusions can be drawn considering a single bubble into an infinite polymeric matrix [76]. The bubble, due to an initial gas overpressure, is assumed to grow keeping a spherical symmetry as shown in Fig. 52. This assumption is quite realistic regardless the external pressure. At standard atmospheric pressure, bubbles tend to assume spherical shapes in order to minimize their energy; then the foam expansion in vacuum is expected to be similarly isotropic [76].

Bearing in mind these global considerations, we limit here to study of the evolution of a single bubble. This actually means that this single bubble is the envelope of all the initial bubble nuclei and that any bubble merging is neglected. The analysis here performed is based on the classic Rayleigh-Plesset equation [77,78]. In this way it is possible to provide the evolution of the bubble radius by means of an analytical method.

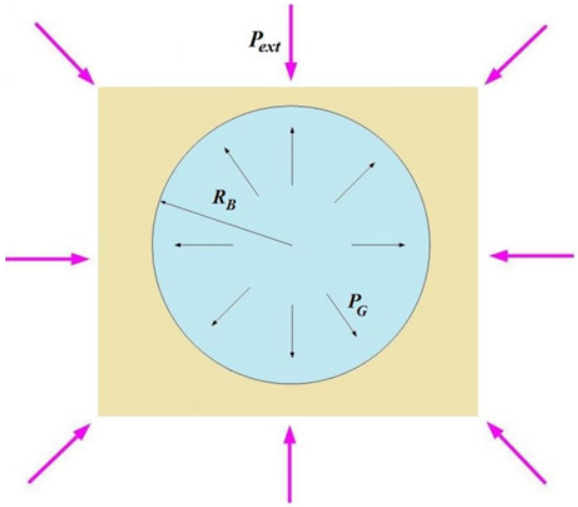

Figure 52: Bubble of gas into an infinite polymeric matrix. The purple arrows indicate the external pressure and the arrows inside the blue bubble represent the gas pressure.

The Rayleigh-Plesset equation can be written as follows [77,78]:

$$\rho_l\left(R\ddot{R}+\frac{3}{2}\dot{R}^2\right)=-\frac{2\sigma}{R}+P-P_\infty-4\mu\frac{\dot{R}}{R} \tag{25}$$

where ρ_l is the density of the liquid, μ its viscosity, σ the gas/liquid surface tension, R the instantaneous bubble radius, P the pressure of the gas inside the bubble and P_∞ the pressure in the liquid matrix. The pressure in the liquid, different from the one of the gas at the beginning of the expansion phase, is constant and equal to the external pressure [76].

Equation (25) can be further simplified by means of a dimensional analysis of the equation terms. The first term on the right hand side takes into account the surface tension effects. From the evaluation of the *capillary number*, which represents the relative effect of viscosity with respect to surface tension, it comes out that this contribution can be neglected. The capillary number can be expressed by means of [76]:

$$Ca=\frac{U\mu}{\sigma} \tag{26}$$

Indeed, during the expansion we have $Ca>>1$, since μ and σ are in the range of 1e5 *Pa s* and 1e-2 *N/m*, respectively [79,80] and U is a characteristic velocity of the order of few meters per second. Furthermore, it is possible to evaluate the influence of inertia effects, represented by the term on left hand side of the Eq.(25). The inertia term role is well modelled by means of the Reynolds number *Re* [76,79]:

$$\mathrm{Re}=\frac{\rho_l V_B^{2/3}\left(P-P_\infty\right)}{\mu^2} \tag{27}$$

Here the numerator represents the inertial term and the denominator the viscous one, thus the absolute value of this non-dimensional parameter gives an idea of which one of the two dominates. According to [76,79,81], $Re<<1$ for applications like the one in consideration. As a consequence also the inertia effects can be neglected if compared to the viscous term.

Most of polymerization reactions are exothermal, but the polymer mass is much larger than the gas mass, thus it represents a very large thermal inertia that slowly conduct part of the produced heat to the gas. Thus, in first approximation, a constant temperature for the whole gas reaction is a reasonable assumption. This means that, besides previous assumptions, considering also the isothermal case, Eq.(25) can be written as [76,79]:

$$\frac{\dot{R}}{R} = \frac{P - P_{\infty}}{4\mu} \tag{28}$$

Equation (28) models the radius time evolution due to a pressure difference taking into account the viscosity effects. It is clear that this local growth velocity depends only by the local pressure difference. In the simple single-bubble model, this local pressure difference corresponds also to the global one.

From Eq.(28), when $P \rightarrow P_{\infty}$, $dR/dt \rightarrow 0$, thus the bubble stops growing and stationary conditions are reached. On the contrary, when $P_{\infty} \rightarrow 0$, the bubble grows indefinitely. It is worth stressing since now, that this model can not forecast the bubble radius value in perfect vacuum conditions, but it just gives an approximation of the bubble evolution even at very low external pressures.

It is possible to find an analytic solution of Eq.(28) as function of material properties, initial conditions inside the bubble (pressure and radius) and outside pressure [76]. Assuming, as already mentioned, that the inflating gas obeys to the perfect gas law, it follows that the product between pressure and volume is constant since the temperature is assumed constant. This can be written in equation as:

$$PR^3 = P_B R_B^3 \tag{29}$$

where the volume has been expressed by means of its radius dependency for a spherical shape ($V=4/3\pi R^3$). In Eq.(29) the left hand term represents the final state and the right hand one the initial condition.

Under these considerations, the time (t) evolution of the bubble radius (R) is expressed by [76]:

$$R(t) = R_B \left[\left(1 - \frac{P_B}{P_{\infty}} \right) \exp\left(\frac{-3P_{\infty}}{4\mu} t \right) + \frac{P_B}{P_{\infty}} \right]^{1/3} \tag{30}$$

where actually this equation is the result of the integration of Eq.(28) under the assumption of Eq.(29).

In this model, the polymeric matrix has constant viscosity. It is the viscosity of the resin dough and is equal to the one at the beginning of the reaction. Actually, the viscosity increases during the polymerization process as an exponential function of time [81]:

$$\mu(t) = \mu_0 \, e^{\frac{t}{t_{dry}}} \quad , \tag{31}$$

where t_{dry} , called *drying time*, is an input parameter depending on the specific foam. It is clear that, if t_{dry} is several times larger than process time, it is possible to assume that the viscosity is constant in time [81]. Moreover, experimental results [77] show that there are no significant effects on the

final foam expansion volume caused by the variation of viscosity in time. Thus, considering constant viscosity is a reasonable assumption and it is used in the following model validation. Finally, considering bubble clusters would add another degree complexity to the simulation. The bubble interactions came into play and the bounding surfaces assume very complicate shapes where the surface tension effects can not be neglected anymore [73].

6.2 Model Validation

In order to implement and test the model derived in the previous section, some additional assumptions are required. These are mainly related to the specific foam to model and the value provided should be tuned according to experimental tests.

Most of the reactions generating blowing agents produce carbon dioxide (CO_2). In this validation it is always assumed that this gas is the one expanding inside the bubbles. The molar mass of CO_2 is 44.01 *g/mol* that results in a gas constant $R_G = 8.314471/44.01 = 188.9233\ m^2/Ks^2$. Of course just a limited fraction of the whole initial polymer mass can be transformed into gas. Such a fraction depends again by the specific reaction and it is in general very small. Moreover, it is possible to assume that the reaction proceeds at constant room temperature of 25 °*C*. The density of the unexpanded foam components is very close to the one of water. Actually this value for the two components mixture, i.e. the prepolymer, is slightly higher, with densities in the range 1000-1500 kg/m^3 [82]. Polyurethane foams are close to the lower boundary of this range [83]. A prepolymer density of 1100 kg/m^3 is here assumed and it represents again a quite conservative assumption. In general, the final foam volume increases assuming lower initial densities. As said, the growth is driven by the pressure difference between the gas pressure inside the bubble, *P*, and the background pressure outside the matrix envelope, P_∞. Here we assume that, as the reaction starts, the initial pressure difference is in the range of 1e2 *Pa*, and in particular 100 *Pa*, seems to be a good assumption [76]. Of course, once the initial gas pressure inside the bubble is known, by means of the perfect gas law, it is possible to calculate the initial gas density. The (constant) value here assumed for the viscosity of the polymeric foam is 5e5 *Pa s* [79,80].

After these assumptions, a specific foam has to be considered to assess the bubble radius evolution. In particular, it is required to evaluate the gas mass. It is possible to assume that all the gas mass spreads instantaneously at the beginning of the reaction. In this way the gas mass at the end of the reaction is equal to the one at the beginning. By way of example, let us consider the ESPAK 90 foam [84]. It is a commercial two components foam expanding, at atmospheric pressure, from 10 to 16 times its initial volume [84]. The foamed polymer is declared to have a density about 90 kg/m^3 [84]. Assuming again the same reference density 1100 kg/m^3 for the two originating components, this means that a gas percentage around the 2% of the original mass has been transformed into gas. This number can be approximated from the final value of external pressure as follows:

$$\begin{aligned} m_G &\cong \rho_G V_F\big|_{FIN} \cong \frac{P_G}{R_G T_G} V_F\big|_{FIN} = \frac{101325}{188.9 \times 298.15} f\, V_F\big|_{IN} = 1.799 \times 13 \times 8e-6 = 1.87e-4\, kg \\ m_P\big|_{IN} &= \rho_P\, V_F\big|_{IN} = 1100 \times 8e-6 = 0.0088\, kg \\ m_G / m_P\big|_{IN} &\approx 2\% \end{aligned} \tag{32}$$

Here the first equation estimates the gas mass by the final foam volume which is correlated with the initial volume by means of the expansion factor, *f*. The second equation estimates the initial polymer mass from the initial component densities and the last one gives their ratio, i.e. the

percentage of initial mass transformed into gas. An initial volume of 8 *ml* of polymer resin (4 *ml* for each component) and an expansion factor of 13 (the average between 10 and 16) have been assumed. This percentage heavily affects the resulting foam volume and specific values should be available, nevertheless the estimation here made can be considered rather reasonable. It is worth stressing that in the first of Eqs.(32) the internal pressure has been considered, as the reaction is assumed to be already completed, equal to the external one due to the internal-external pressures balance.

To this gas mass percentage corresponds an initial volume of gas, which gives us the initial radius for the bubble R_B under the spherical bubble assumption. This can be easily computed as follows:

$$V_B = V_F\big|_{IN} \frac{\rho_P}{\rho_G} \times 0.02 \qquad R_B = \left(\frac{3V_B}{4\pi} \right)^{1/3} \tag{33}$$

In order to evaluate the validity of the model for the growth of a single bubble into the polymeric matrix, it is possible to compare its results with (very limited [85]) bibliographic data and with commercially available two components polymeric foams.

First of all, implementing the model at atmospheric pressure, we obtain a final volume of gas around 0.098 *l* (from an initial one of 8 *ml*) corresponding to an expansion factor slightly larger than 12. This value perfectly fits into the range declared by ESPAK 90 (between 10 and 16 at atmospheric pressure)

Furthermore, Fig. 53 shows the trend of bubble growth in percentage, with a reaction time of 60 *s*, equal to the typical value of ESPAK 90 [84] and, in general, close to the one of polymeric two components foams.

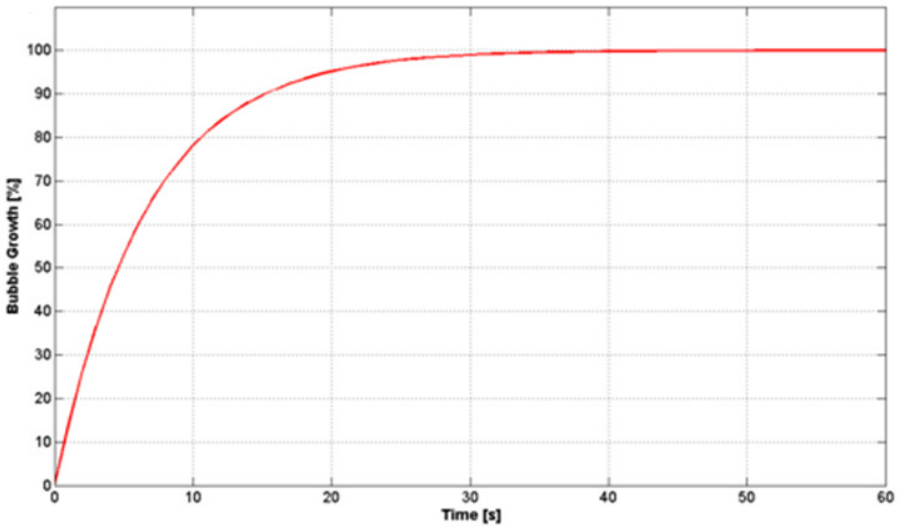

Figure 53: Time evolution of bubble radius at 10100 *Pa*.

We are more interested however, in the foam expansion process in vacuum, or, in general, in very low pressure conditions. Some experimental results for the growth of an air bubble in a viscous fluid under vacuum conditions are shown in [85, 77]. In particular, in [77] also the Rayleigh-Plesset equation is exploited to develop an analytic model, and afterward a series of experiments in vacuum chamber are shown in order to evaluate the effectiveness of the model. In this work, however, the surface tension term is not neglected, but a value of 0.02 *N/m* is considered. This value leads,

however, to a capillarity number (Eq.(26)) much larger than one which motivates to neglect the surface tension effect.

The effect of this term is here briefly investigated in order to understand if it influences the (actually small) difference between this model and the experimental results of [77]. According to the reference case modelled in [77], the initial bubble radius is 0.477 *mm*, the outside pressure around 8100 *Pa* and the initial gas pressure value inside the bubble approximately 101100 *Pa*. The model presented in [77] predicts a reaction time of 0.2 *s* and final radius of 1.1 *mm*. This implies an expansion factor of approximately 25. In the same work, however, experimental results measured a final radius of 2.5 *mm*, corresponding to an expansion factor of about 150. Moreover, the resulting reaction time is around 20-25 *s* [77]. Figure 54 is taken from [77] and it shows the comparison between experimental results and the model there developed.

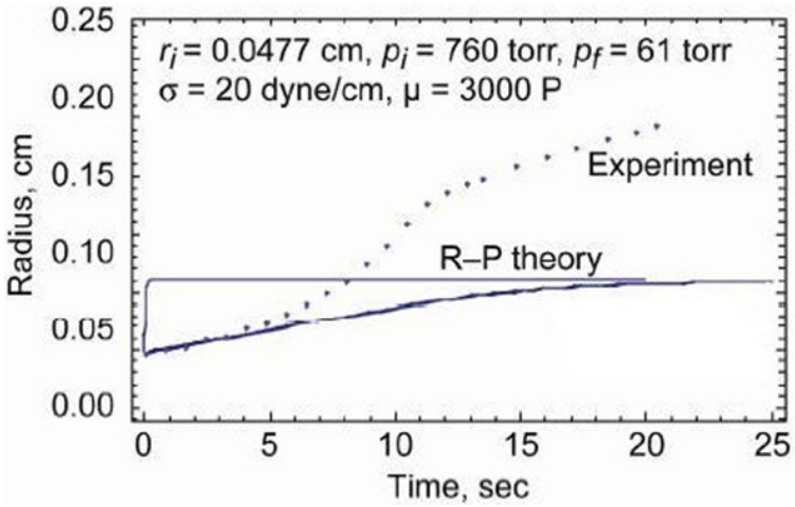

Figure 54 : Comparison between experimental results and model developed in [77].

It is clear from Fig. 54, the significant difference between theoretical and experimental results in terms of final radius and reaction time. In particular the model developed in [77] results to be too conservative with respect to the experimental data.

On the contrary, implementing the model here presented with the same value for the external pressure and the above values for ESPAK 90 (initial polymer volume, initial percentage of gas mass and initial internal pressure), results an expansion factor of the same range of the experimental results (≈152). This comparison validates the presented model with the experimental results presented in [77]. It has to be mentioned, however, that the specific foam characteristics can affect the resulting expansion factor, also if it is reasonable to assume that it remains in the range of some hundred % at some thousands of *Pa*.

Figure 55 shows the trend for the bubble growth in percentage with the input data above described in order to compare the model here implemented with results of [77].

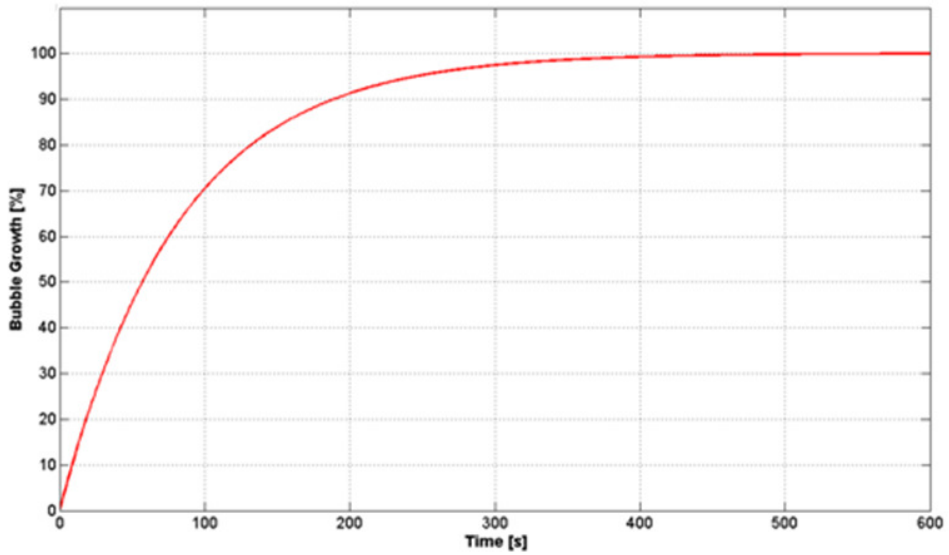

Figure 55 : Bubble growth in time, estimated by the analytical model at 8100 *Pa* and μ=5e5 *Pa s*.

It is worth stressing that in low-pressure conditions, the reaction time is much larger than in atmosphere. Even compared to the experimental cases [77], there is a different temporal scale. Most probably this is due to the different value of matrix viscosity. In fact, the viscosity of the solution influences the ability of the solution to flow under the gas expansion, thus a larger viscosity value corresponds to a larger inertia in the expansion process and accordingly a longer process time. In Fig. 56 the result for the bubble growth in percentage using a value of viscosity in the range of 1e3 *Pa s*, the same one assumed in [77], is shown.

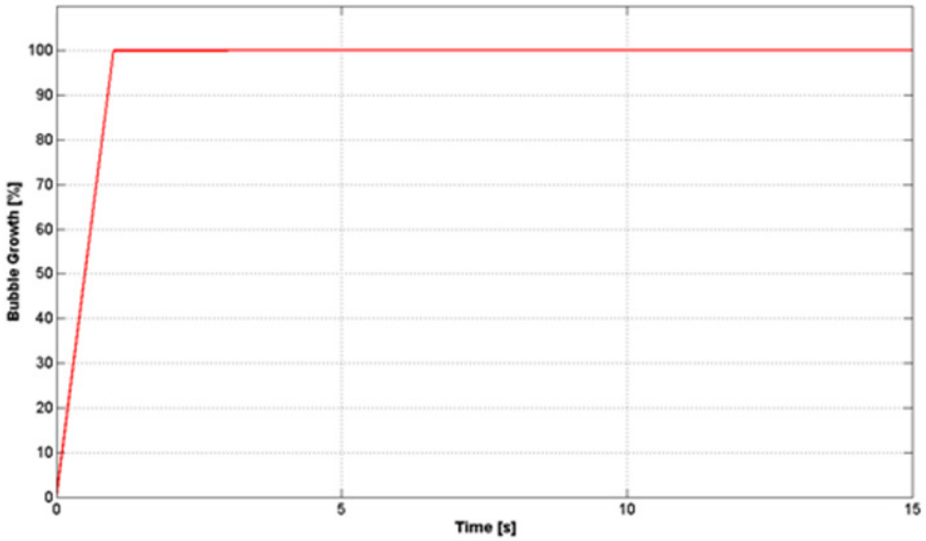

Figure 56 : Bubble growth in time, estimated by the analytical model at 8100 *Pa* and μ=1e3 *Pa s*.

As shown, in this case the reaction time decreases to around 1 *s*, i.e. the expansion occurs almost instantaneously.

Compared to theoretical results shown in Fig. 54, it is possible to observe the same absence of transitory, but, while the asymptotic value for [77] is smaller than the experimental results, in our implementation the expansion achieves an asymptotic value comparable to the experimental one.

Furthermore, this motivates to argue that changing the viscosity order of magnitude influences only the time scaling for the bubble growth, but not its final value, this is indeed visible in Eq.(30). Moreover, as the viscosity increases, the reaction time increases.

All in all, both the atmospheric pressure comparison and the experimental comparisons have shown that the proposed model catches the order of magnitude of the expansion factor of polymeric foam even at low external pressure regimes.

6.3 Pressure Dependence

The aim of this section is to point out the strong dependence of the foam expansion process from the external pressure resulting by the model presented in Sec. 6.1. In particular, as pressure decreases, the bubble radius, and accordingly the final volume and the reaction time, increases. This causes a general increasing of the expansion factor for decreasing external pressures. In order to explicitly investigate about this dependence, it is possible to implement the model for different values of the external pressure with the above mentioned values for the ESPAK 90 foam, see Sec. 6.2. The results, in terms of final foam volume and expansion factor are shown in Fig. 57.

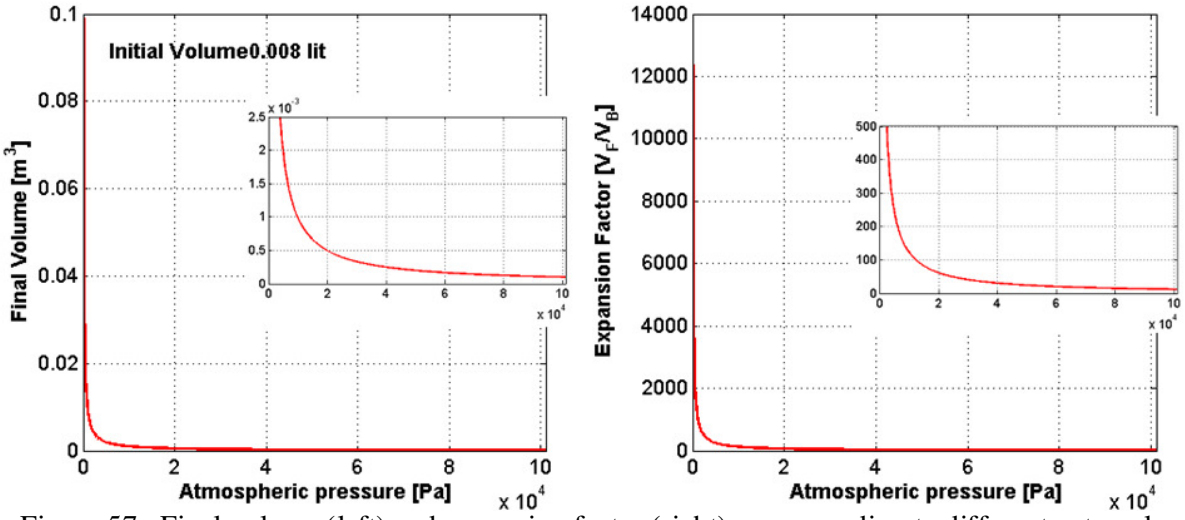

Figure 57 : Final volume (left) and expansion factor (right) corresponding to different external pressures in the range [0, 1e5] *Pa*.

On the left of Fig. 57, the final volume of the original 8 *ml* of polymer is shown; the hyperbolic trend can be easily observed. For instance, at 1/10 of the atmospheric pressure, the final volume is approximately 1 *l*, while it grows up to around 10 *l* at 1/100. On the right plot of Fig. 57, the expansion factor (final-to-initial volume ratio) evolution is shown and it reflects again the same hyperbolic behaviour.

In order to complete this analysis, in Fig. 58, also the foam density and its porosity are shown. Once the final foam volume is known, the foam density can be retrieved by the mass conservation. In addition, the foam porosity represents a measure of void spaces. In equation it is given by [86]:

$$\phi = \frac{V_B}{V_{TOT}} \tag{34}$$

where V_B is the bubble volume (the void space volume) and V_{TOT} is the total volume of material, including solid and void components.

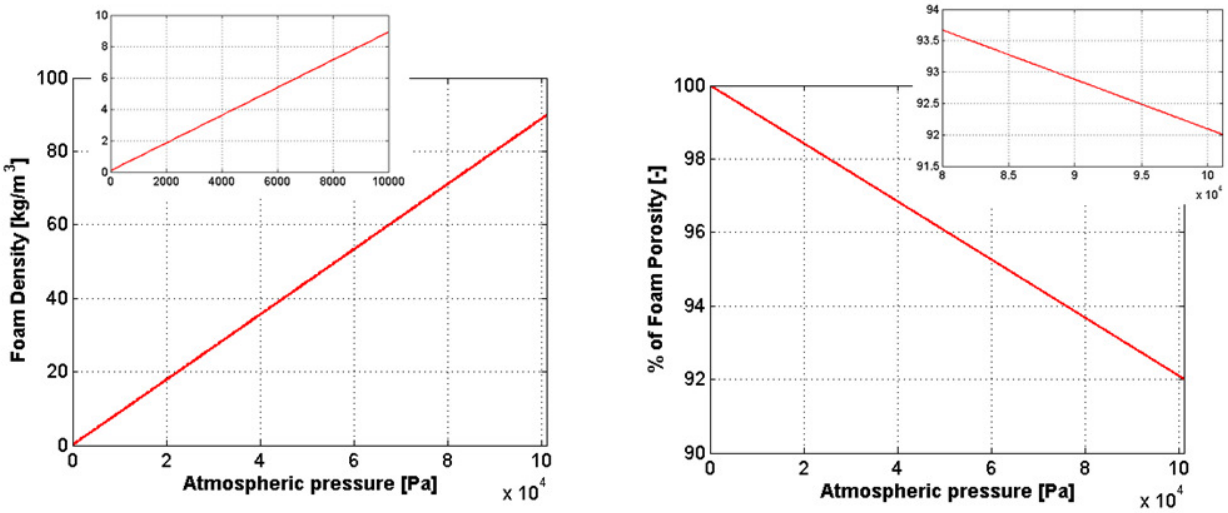

Figure 58: Foam density (left) and its porosity in percentage (right) corresponding to different external pressures in the range [0, 1e5] *Pa*.

In this analysis the hyperbolic trend shown results in an expansion factor tending to infinity when the external pressure tends to zero (as already stressed in Eq.(28)). At 0.001% of the atmospheric pressure, the foam has to expand with an outside pressure of approximately 1 *Pa* that corresponds approximately to the pressure in a low Earth orbit of around 100 *km* altitude. In this situation, the reduced order model implemented results in a final volume of approximately 9.9 m^3, that means an expansion factor of 1.2e6. The final density would be close to 1e-3 kg/m^3.

State of the art ground based foams could not be able to tolerate such high expansion factors and to polymerize fast enough to capture the blowing agent. Thus, these values have to be intended as reference values highlighting the hyperbolic trend of expansion with respect to the outside pressure. Of course, we are here referring to already existent two-component polymeric foams, and ad-hoc space-developed foams could have characteristics significantly beyond the values here assumed, improving the performance of the deorbiting method. Since the values here obtained are just the results of a low order analytical model, more conservative parameter values are considered for the following studies. For this reason, in Sec. 7, a parametric analysis is carried out with respect to the final foam density and the expected expansion factor in order to identify suitable but more conservative foam characteristics.

7 FOAM IDENTIFICATION

The analysis and the categorizations summarized in Sec. 5, aim to choosing specific foam class for the conceived foam-based deorbiting application. It comes by itself that the key technology of the proposed scenario is the foam. As highlighted in Sec. 5, polymeric foams seem to have a good compromise between mechanical characteristics and versatility. Two-component polymeric foams, furthermore, offer also a simply foaming process, even without any mechanical moving components, see Sec. 9.

In this section, a rough identification of the more suitable polymeric foam characteristics is given; pointing out (where possible) specific value ranges and comparing these with the state of the art for ground based expanding foams of the same kind. In general, the foam we are looking for has to fulfil several fundamental requirements:

- It has to be sticky, such that the foam ball-like structure formed and the debris become a single object with a high area-to-mass ratio.
- The foam has to be able to undergo the polymerization process, the expansion and the curing in vacuum.
- The higher the expansion factor, the better the performance of this scenario. In general, increasing this value decreases the foam mass required to realize the same cross section, thus decreasing the incidence of the debris on the total mass of the deorbiting platform.
- The lower the density of the unexpanded foam, the lighter the architecture of the deorbiting platform or, equivalently, more debris can be deorbited with the same launch mass.
- The foam should not degrade too fast during the atmospheric re-entry, otherwise the area-to-mass ratio diminishes causing longer deorbiting times. However, this requirement is not that crucial as, lowering the altitude, the foamed-debris encounter higher density atmospheric layers. Thus, it will keep deorbiting, although in a time potentially longer than the prescribed threshold (and the one estimated in this study).
- It is preferred that this foam is not hazardous for human and for the on-board equipment. The foam should be even environmentally innocuous, if burning up in the atmosphere, or crashing in waters or on the ground.

At this point the aim is to provide a rough estimation of suitable values at least for the foam expansion factor and density. The analysis follows a reference foam ball radius of 10 *m*, as assumed in Sec. 4 as the optimum value to achieve the highest area-to-mass ratio for a 2-2.5 *tons* debris, see Fig. 20. With such value of radius, this kind of debris reaches an area-to-mass ratio of 0.05. Accordingly, it can be deorbited from 800 *km* within 13 *years*, see Fig. 4.

What described so far does not depend explicitly on the specific foam characteristics. These come into play at this point to size the ball cross section, its mass and its stored weight. In fact, the higher the foam expansion factor the smaller the initial foam volume. From Fig. 59, it is possible to compare the compressed volumes required for different expansion factors. A range from 100 to 5000 times of the initial foam volume is explored.

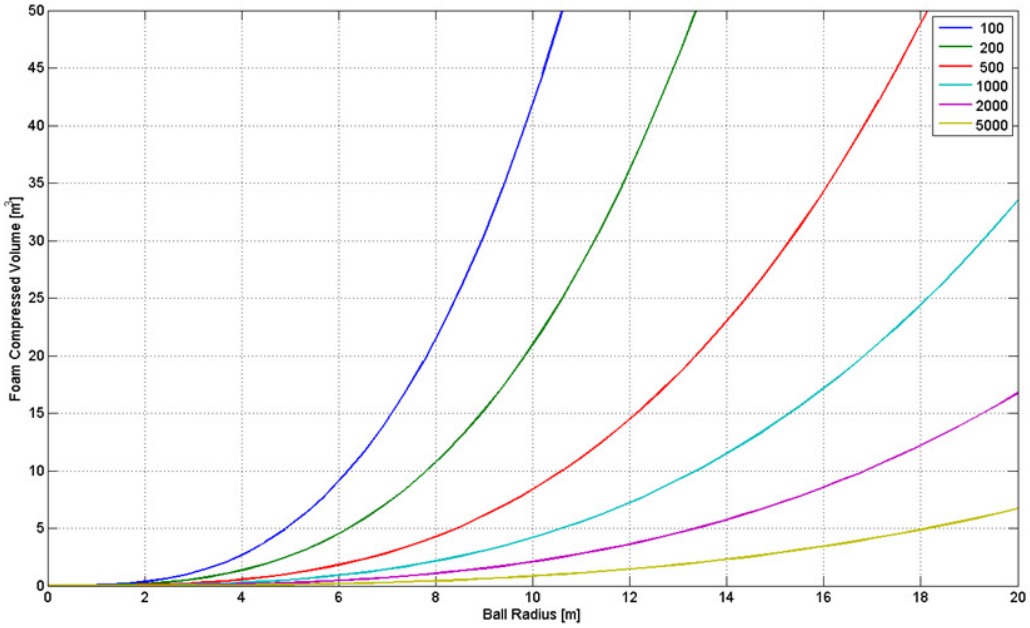

Figure 59: Foam compressed volume with respect to the radius of the resulting foam ball.

In the range explored, it is clear that a remarkable reduction of the original volume can be obtained increasing the expansion factor up to 1000 times. Of course, further increasing this value, the compressed volume decreases for the same value of ball radius, but the gain is not as meaningful as considering the difference between 100 and 1000 of expansion factor. Considering again 10 m as reference radius value, the foam compressed volume reduces from 42 m^3 for an expanding factor of 100 to 4.2 m^3 for 1000; considering the case of 5000, it is just 0.85 m^3. Moreover, it is important to stress that, as already mentioned in Sec. 5, ground-based polymeric foam can expand up to 280 times their volume [41].

The second key factor to take into account for the preliminary assessment of the foam description is its density. Of course, once the tank has been designed to contain a given foam compressed volume, the lighter the foam components, the better. In general, depending on the compressed foam density, the same debris can be deorbited foreseeing a larger or smaller platform launch mass. Assuming that the mass of the expanded foam is given by the sum of the masses of the two components (i.e. there is no mass losses during the foam ejection), a suitable value for the foam density can be obtained considering its density at the end of the expansion phase. Moreover, since the two polymeric components may have different densities and require different mixing ratios, the result of this analysis could be also intended as a target value to develop an ad-hoc foam.

Carrying out a preliminary analysis on the foam density, similar to the one done before, it is possible to identify a sort of qualitative threshold for this value. This analysis considers a 2500 kg debris and the foam-debris mass ratio for growing foam ball radii, in order to identify a suitable foam density value. Figure 60 shows the foam-debris mass ratio for different values of the expanded foam density as function of the ball radius.

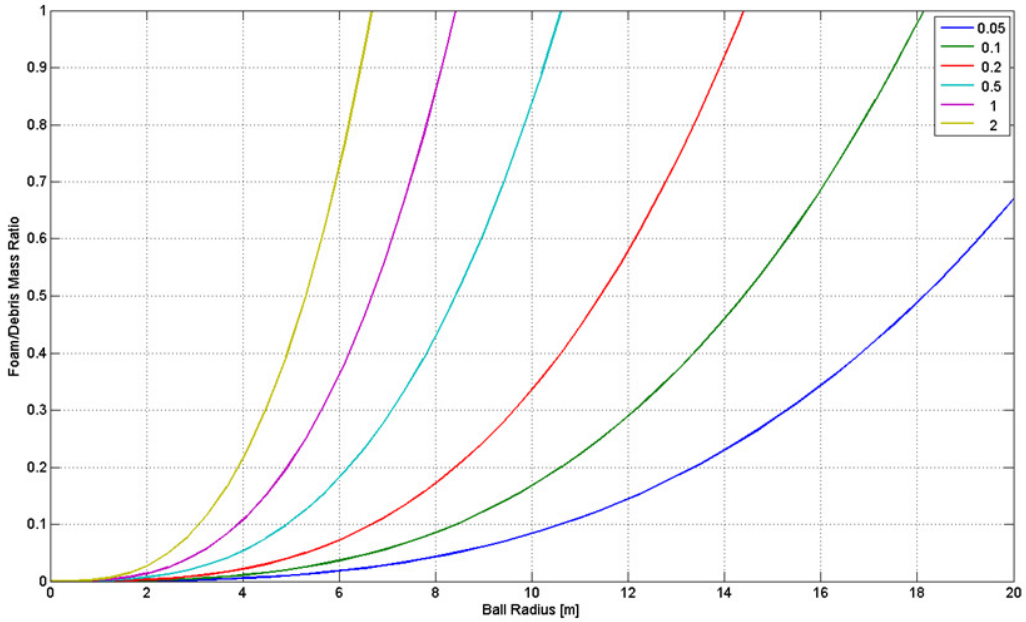

Figure 60: Foam-debris mass ratio for different values of the expanded foam density as function of the ball radius.

Considering again a foam ball radius of 10 *m*, it is clear that densities higher than 0.5 kg/m^3 could require a foam mass larger than the one of the target debris. In particular an expanded foam density of 0.2 kg/m^3 gives a significant mass saving, if compared to larger values. From Fig. 60, it is clear that further lowering the foam density below this value does not give particular advantages. Of course, the smaller the density, the lighter the foam components and more foam can be carried on board of the deorbiting platform.

Again, a short comparison with the density ranges of ground used polymeric foam can be carried out. Low density foams are already available with densities in the range 6-18 kg/m^3 [87] (although also values in the range 1-6 kg/m^3 are declared [87,88]).

Bearing this in mind, for the following analyses (in particular Sec. 8-11) a foam density value of 1 kg/m^3 (after the expansion) will be considered. Such density value is clearly not suitable (see Fig. 60) as it could require 4.2 *tons* of foam to deorbit 2.5 *tons* of debris. The considered value can be intended as the foam density that would assume the commercial polymeric foam considered in Sec. 6 if it could be able to reach an expansion factor of 1000. This density value is also the outcome of the analytical model for the same value of the expansion factor (see Figs. 57-58). Moreover, also the lightest developed silica aerogel is declared to have such a density [89].

It is worth stressing that the previous analyses have been performed taking into account only a reference value for the debris mass and that the optimum foam ball radius varies accordingly to debris characteristics and orbit, so the outcome of these parametric investigations could be considered as rather conservative, since one of the worst conditions has been used.

Concerning the other foam aspects, there are at least few mandatory remarks. Considering commercial available foams, the foaming process, requiring anyway a mixing phase, can be accelerated by two mechanisms. The first one exploits a heat source to speed up the cure, the hardening process and to drive off solvents or other volatiles possibly present in the liquid dough [90]. Another possible approach uses Ultraviolet (UV) light to activate this curing process. Indeed, the light emitted from an UV source, which is the radiant energy, is absorbed and then converted into chemical energy. With this method the cure process starts in a rapid, almost instantaneous, way

and it occurs without volatile losses [90]. In the sought application, UV sources are widely available in space and can easily exploited to cure the foam. Furthermore, a thermal approach can produce polluting gases and it would be significantly affected by the specific debris orbit [90].

Further considerations should have to be done about the desirable rigidity of the foam at the end of its expansion phase. This would help to identify the exact compromise between stiffness and elasticity, with respect to the expected impact of the ball with other larger or smaller debris. Also the foam reaction time can be a significant parameter but, for the level of this analysis, some minutes appear a desirable value.

Let us conclude this section with a brief summary of these main parameters and their values. Table 8 takes in consideration the most relevant factors and outline a suitable value for each one. Furthermore, in the fourth column, also the state of the art (SoA) for the same parameters is given.

Parameter	Units	Value	SoA
Expansion Coefficient	–	1000 (>1000)	20–1000 (280)
Thermal Expansion Factor	$1/°C$		<1e-6
Stickiness	–	with metals	
Compressed Density (25°C)	kg/m^3	200	~ 1000
Expanded Density (25°C)	kg/m^3	1	>6
Human Hazardous	–	low	From low to high
Porosity		~ 90%	> 50%
Kinetic Parameter	$s^{-1}\ m^{-2}$		Order of 10^{-4}
Dough Viscosity	$MPa\ s$	0.5	0.01 – 10
Characteristic Time	s	6000	> 1 min
Foaming Process	–		Mixing + Thermal/UV curing
Vapour Pressure (25°C)	$mbar$		Order of 10^{-5}
Freezing Point	$°C$		from 50 to 50
Boiling Point	$°C$		from 100 to 400
Flexibility Range	$°C$		from -200 to 200

Table 8: Foam main characteristics values and state of the art ranges.

Values provided for the state of the art of ground based foams have to be intended as indicative since specific foam can present values well beyond these ranges. The values indicated in the third column of Tab. 8, instead, are the one sought for the candidate foam. Among these, actually, the crucial ones are the expansion factor (as large as possible) and the density (as low as possible). The others are indicated as derived by means of the foam expansion model, see Sec. 6. The missing values of this column have not been addressed in this analysis. The development of foams with such specific characteristics would result, however, in a very effective debris removal system.

All in all, these analyses were aimed to identify candidate values for the foam density and expansion factor to be used in the mission analysis section, see Sec. 10. For this reason a more conservative value of 1000 is assumed (instead of over a million, see Sec. 6) in the following as expansion factor. To this value corresponds, by the analytical model, a density of 1 kg/m^3 that is the only actual relevant value required in the mission analysis. Just to give a rough idea of the plausibility of this number, it has to be mentioned that BASF® BASOTECT has a density of 6 kg/m^3 in atmosphere [91]. Its expansion factor is not known. Thus a density of 1 kg/m^3 seems a rather realistic assumption for future polymeric foams ad-hoc developed for space applications.

8 PLATFORM PRELIMINARY SIZING

The aim of this section is to realize a preliminary sizing of the deorbiting platform and its propulsion system. This is required as the following mission analysis depends on its mass and performance. Furthermore, the specific initial mass value and the thruster considered highlight if the state of the art space technology are already suitable or innovative equipment have to be developed. In other words the choices here made reflect on the mission feasibility

The first task we have to face, is the identification of the best suited commercially available launchers. In this first analysis, we can not precisely assess the payload (i.e. foam) mass. This happens as the system design and the mission analysis are two iterative and entwined processes. Nevertheless, as reference value we are assuming that some metric tons of launch mass are required. The analysis on available launchers is here limited to European vehicles belonging to the Arianespace launcher family. This class can be broadly divided into very powerful launchers (e.g. Ariane 5), medium size launchers (e.g. Soyuz) and small size launchers (e.g. Vega) [92].

Ariane 5 is able to carry payloads up to 10 metric tons to Geostationary Transfer Orbit (GTO) and more than 20 *tons* into LEO. These two operative orbits are actually reached by two different versions of Ariane 5, the Ariane 5-ECA and the Ariane 5-ES, the first one tailored for GTO missions and the latter for LEO ones [93]. Considering medium class launchers, one of the most common and reliable is the Soyuz. It is able to carry payloads of approximately 3150 *kg* in GTO and up to 5 *tons* can be released into Sun-synchronous Orbits, circular with altitudes around 800 *km* [94]. The smaller launcher of the Arianespace family is Vega. It is tailored for missions to LEO and SSO and its payload capacity is limited to 1500 *kg* into 700 *km* circular polar orbit [95].

On one hand the Ariane 5 launcher is too heavy and costly to represent, at least in the beginning, a valuable option for the deorbiting application proposed. Its payload capacity is well beyond the performance here expected. On the other hand, Vega performance is too limited and definitely not sufficient for our scopes. Actually, choosing this launcher would significantly limit the initial platform mass, thus the number of debris that can be deorbited. This would imply much more missions to clean up even limited space regions, thus however increasing the general mission costs. For these reasons, the Soyuz launcher represents a good compromise, at least in the family considered. Of course, the same qualitative analysis could be extended to non-European launchers. Nevertheless, a complete list and the consequent eventual choice could be verbose and far beyond the scopes of this section. It is worth stressing, however, that in the same performance range of the Soyuz launcher there are several other vehicles, thus the launcher here chosen has not to be intended as the only option, but as a representative type constraining just the launch mass upper limit.

Many of the listed debris, as pointed out in Sec. 3, lie in the SSO region at approximately 800-900 *km*. Bearing this in mind the reference launch mass is here defined assuming the Soyuz launcher and its performance into a SSO of this altitude. Figure 61 shows the Soyuz performance, in terms of deliverable payload, at circular and almost polar orbits between 300 and 1800 *km* altitude [94]. The reference working point is, accordingly, a SSO orbit of 900 *km* inclined at 99 *deg*. In this orbit the launcher is able to carry a total mass of 4600 *kg*, see Fig. 61.

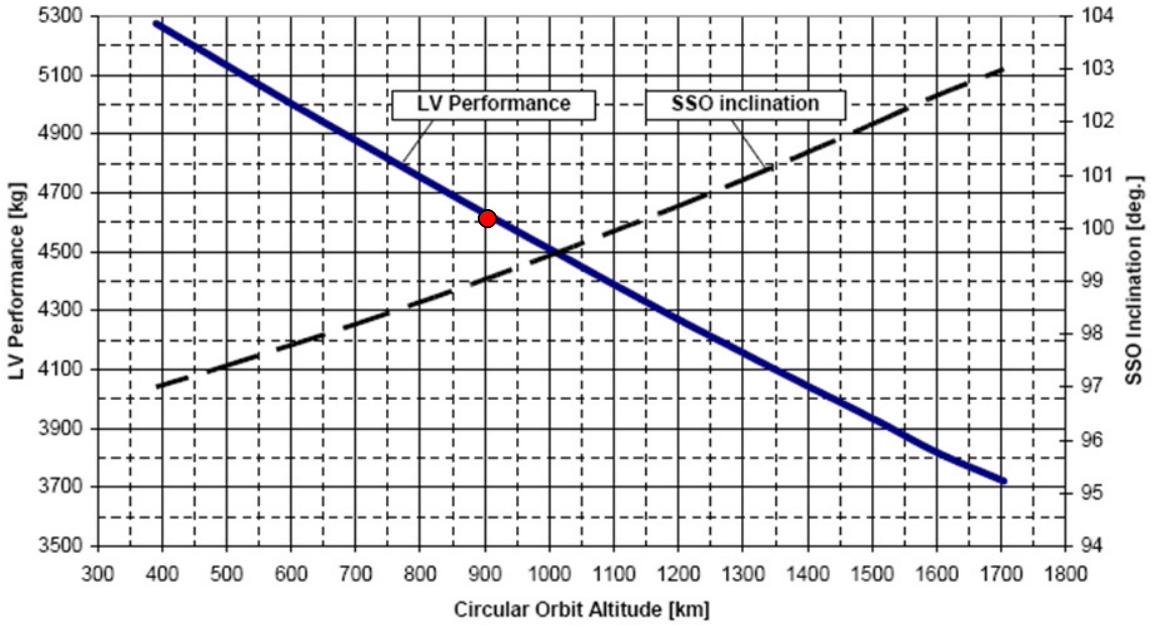

Figure 61: Soyuz vehicle performance for SSO as function of altitude [94]. The red dot indicates the chosen working point.

In the following, this initial mass is assumed as launch mass. However, it is worth stressing that this mass can not be completely allocated for the foam, as the structure, together with the main subsystems of the platform and the propellant for the necessary orbital manoeuvres have to be considered. A rough estimation, refined in Sec. 8.2, considers 1 *ton* for the onboard subsystems and the remaining 3.6 *tons* equally divided between foam and propellant. The sizing of the platform, in terms of the main subsystems mass and power, is shown in Sec. 8.2 to demonstrate that approximately the 20% of initial mass is sufficient to preliminary include all the required onboard systems.

8.1 Propulsion System Identification

This section aims to identify, first of all, a suitable electric thruster for the deorbiting application, and, in second place, a specific reference thruster to assess the mission scenario performance (see Sec. 10). In order to achieve this goal, a brief overview of the electric thruster options is given highlighting their pros and cons. Afterwards, the discussion aims to pick up a specific device and focus on its relevant characteristics.

Although a detailed description of electric propulsion methods is beyond the scopes of this section, in order to identify a suitable thruster for the active deorbiting application, a brief survey of the available options is mandatory.

Electric propulsion schemes are mainly based on the acceleration of charged ions by means of electromagnetic forces. According to the acceleration mechanism, this propulsion methodology can be broadly grouped into three main classes [96].

- *Electrothermal devices* are based on the electrical heating of propellant. The subsequent expansion into a suitable nozzle converts the thermal energy into thrust. To this category

belong resistojets and arcjets. These reach exhaust velocities from 3000 up to 10000 *m/s* and have a typical power-to-thrust ratio in the range 2-10 *W/mN* [97].

- *Electrostatic devices* aim to ionizing the propellant particles that are thereafter accelerated by means of a potential drop. This class includes ion thrusters, Hall effect thrusters and field emission electric thrusters. Such a kind of devices provides exhaust velocities from 10000 to 80000 *m/s* with 20-80 *W/mN* as typical range of power-to-thrust ratio [97].
- *Electromagnetic devices* tend to accelerate the propellant by means of the interplay between an external magnetic field and the electrical current flowing through the ionized propellant itself. Magneto plasma dynamic devices and pulsed plasma thrusters belong to electromagnetic thrusters. In this case from 5000 to 60000 *m/s* can be reached as exhaust velocity with a power-to-thrust ratio between 50 and 90 *W/mN* [97].

Typically the maximum thrust that can be generated excludes some of the previously mentioned systems. As we are assuming to develop a system considering the state of the art technology, also technologies never proven in space and still with low technology readiness values can not be considered as valid options.

The exhaust velocity is often expressed by means of the Specific Impulse (*Isp*) of the thruster, related to the former by means of Earth gravity acceleration, g_0 [96]. In general, increasing the exhaust velocity of the device, the required propellant mass decreases, although the Power Generation System (PGS) mass increases accordingly. This happens because the power subsystem mass is an increasing function of the power (P) by means of a technological coefficient, thus, for a given thrust level (T), it is directly related to the specific impulse by means of [96]:

$$T = \frac{2\eta P}{I_{sp}\, g_0} \tag{35}$$

Considering Fig. 62, it is clear that there exists an optimum specific impulse value, given by the minimum of the total mass curve. A lower value would result in a penalty in propellant mass, while a larger value causes a penalty in the system dry mass.

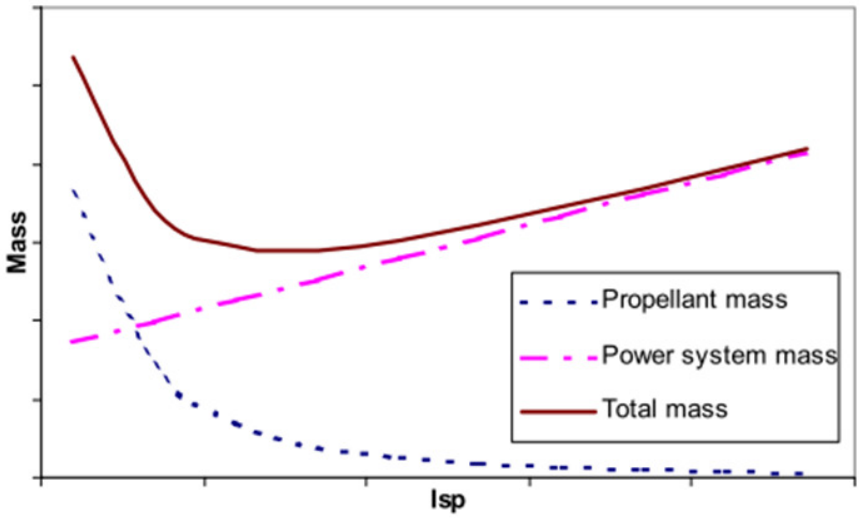

Figure 62: Propellant mass, PGS mass and sum curve as function of specific impulse [98].

The scales on the two axes are missed as they depend, besides from the thrust level, on the power generation source considered and on the current PGS state of the art.

In order to obtain a more specific assessment of the optimum specific impulse, the previous plot has been tailored on the application under consideration. The optimum specific impulse range for a given application, can be estimated by means of the mission ΔV.

The propellant-to-spacecraft mass ratio can be easily computed by means of the Tsiolkovsky Equation [17]:

$$\frac{m_p}{m_0} = 1 - e^{-\frac{\Delta V}{Ispg_0}} \tag{36}$$

where *Isp* is the specific impulse of the thruster and g_0 is the gravitational acceleration value on Earth surface, m_p and m_0 respectively the propellant and the spacecraft mass at the beginning of the thruster operation phase. This equation clearly shows the dependence of the propellant-to-spacecraft mass ratio from mission ΔV and thruster specific impulse. This ratio grows monotonically for growing ΔV values and it is also monotonically decreasing for increasing values of specific impulse. Thus, for a given propellant-to-spacecraft mass ratio, the higher the specific impulse, the larger the total achievable mission ΔV.

Inverting Eq.(35) in order to obtain an explicit relation between the power-to-thrust ratio and the specific impulse, it is possible to relate also this ratio to a single independent variable. Higher specific impulse values involve higher power requirements for a given thrust value. The resulting increase of the power requirements affects the mass of the spacecraft, as the mass of the power generation and distribution subsystem may be considered linearly dependent from the required power. Both these trends with respect to specific impulses in the range 1000-6000 *s* are shown in Fig. 63.

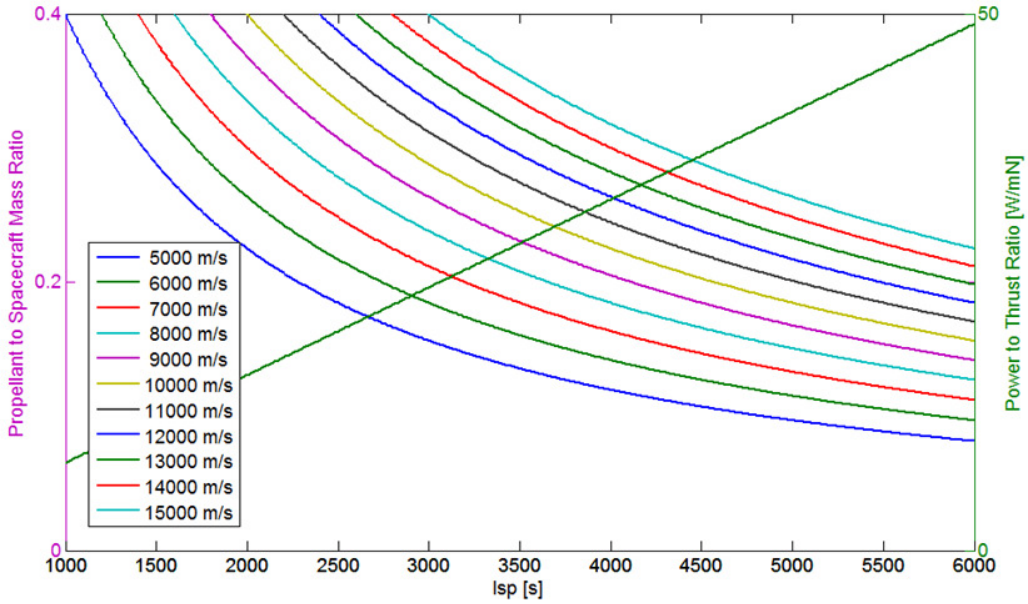

Figure 63: *Isp* vs propellant-to-spacecraft mass ratio and power to thrust ratio for different ΔV values.

At this point the two curves have to be summed up, like in Fig. 62 [98]. In order to compute the total mass curve, however, a proper non-dimensionalization is necessary. The non-dimensional power-to-thrust ratio has been obtained dividing each value with the maximum ratio obtained considering the analysed specific impulse range (e.g. about 50 *W/mN* in Fig. 63). The parameter used for the non-dimensionalization of the propellant-to-spacecraft mass ratio, instead, is defined as the maximum acceptable value for this ratio. At this point, as we are assuming a launch mass around (slightly smaller than) 5 *tons* with approximately 1 *ton* of dry mass (see Sec. 8.2), it is reasonable to assume that the remaining mass is roughly divided between propellant and foam. Of course this does not mean that for each mission about 2 *tons* are required for propellant and about 2 *tons* for foam, but it is a reference value here assumed to obtain the non-dimensional propellant-to-spacecraft mass ratio curve. Of course a propellant-to-spacecraft mass ratio larger than 2/5 would not be meaningful as it would mean to assume that the larger part of tanks is filled with propellant, thus the actual deorbiting system would not be really effective.

The sum of these two non-dimensional curves, for each mission ΔV, allows the identification of a combined dependence of the propellant and power generation subsystem mass, for different specific impulse values. Indeed the minima of these curves, see Fig. 64, represent this best compromise.

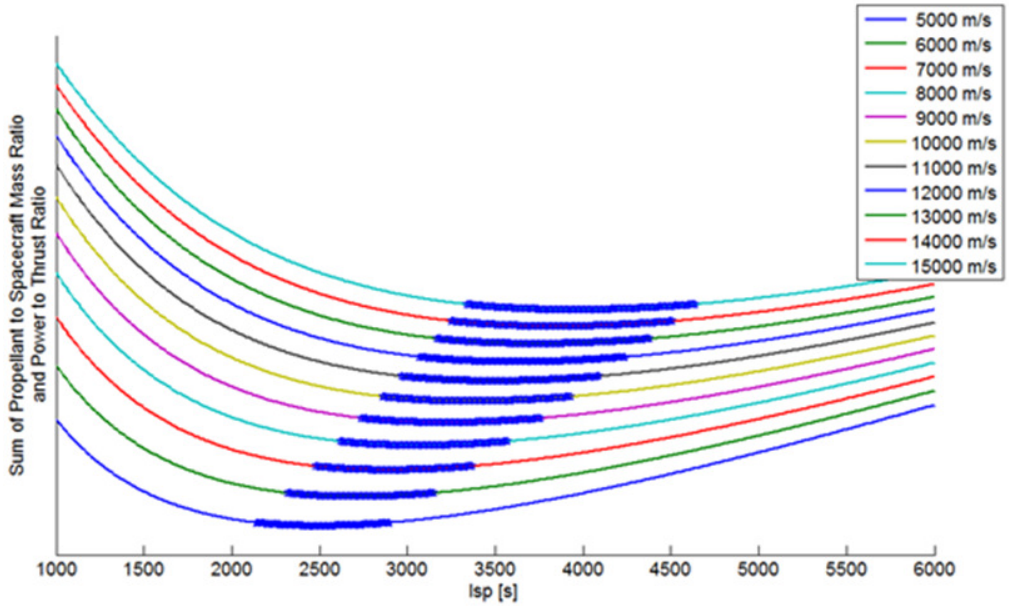

Figure 64: Sum of propellant to spacecraft mass ratio and power to thrust ratio.

Of course, as the presented analysis is based on several assumptions and first guess values, it is not worth identifying a single working point. For this reason, a small range of specific impulse values in the neighbourhood of the minima is highlighted (blue dots in Fig. 64). This range has been identified setting an upper limit from the minimum value equal to 1% of the minimum.

So far, the whole analysis has been carried out for a range of mission ΔV between 5 and 15 *km/s*. This value is actually an input of the procedure and it is here assumed equal to 10 *km/s*. This is a rather large value as many orbital transfers are expected and the gravity losses necessarily cause an increase of the mission ΔV.

Summarizing, the previous analysis shows that, for Earth-close missions and solar generation systems, the optimum value is around 3000-3500 *s*. It is worth stressing since now that this range is the one where Hall effect thrusters can normally operate.

However, a qualitative analysis of all electric thruster methodologies can be easily made to identify the best candidate thruster from a technological point of view [99]. Electrothermal thrusters are able to provide too low values of specific impulse, thus the resulting propellant mass would be too high. Field electric emission thrusters, although have a very large exhaust velocity, are able to provide level of thrust that would result in decades to transfer the platform from a debris to the next one (they are usually used for fine pointing purposes). Magneto plasma dynamic devices would require too much power to work in their optimal range. Hall effect thruster, instead, naturally operate at some mN of thrust with specific impulses between 1000 and 4000 s. Ion thrusters would have been the second-best choice although they usually have slightly better performance they require, in the average, higher power levels to operate. Moreover their size and weight is generally larger than the ones of Hall effect thrusters, mainly due a lower thrust density, causing also significant thermal problems [100].

This survey of the electric propulsion options is completed with Fig. 65. Here the main thrusters so far described are ranked according to the main application field, the power required and the total impulse they are able to deliver.

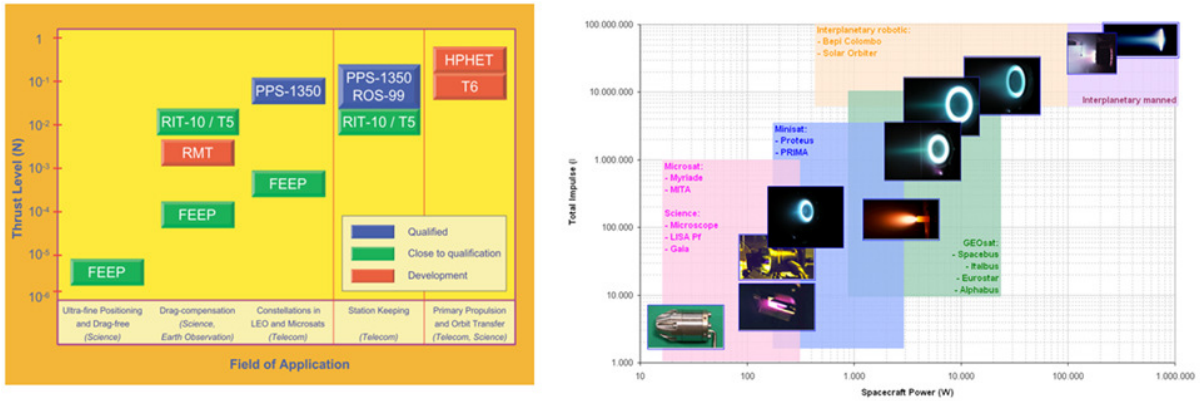

Figure 65: Comparison of different thrusters in terms of power requirements and total impulse [100].

Hall effect thrusters have been already used in space as main propulsion systems. They flew since the seventies on Russian spacecrafts, in particular as attitude control systems. Due to their reasonably high specific impulse they have been also used as plasma sources besides than for main propulsion systems. A Hall effect thruster powered the ESA probe Smart-1 to the Moon [101].

Once that Hall effect thrusters have been selected as best candidates for the application considered, a specific thruster has to be chosen in order to assess the mission analysis performance. Of course, there are several models of Hall thrusters and the mission performance heavily depends on the thruster characteristics, in particular from its thrust magnitude and specific impulse.

Nowadays, the increase in mass and power of telecommunication satellites and the intent upon using electric propulsion also for orbit raising, have motivated the development of more powerful and reliable models. Among these, the selection has been made considering thrusters able to provide a high total impulse. This means that high specific impulses are sought, that leading to reduced propellant mass requirements, enable efficient transfers with power levels around 10 kW.

The SNECMA Moteurs series PPS-X000, see Fig. 66, covers a wide range of powers and performance [102]. Thrusters of this series can operate from 1500 up to 6000 W and they have been already proven in space or are under advanced qualification tests. The PPS-5000 belongs to this

class. It is here considered since it has been already tested and represents one of the main candidates for future space applications of electric propulsion principal propulsive systems [103].
The thruster operates at a nominal power of 5000 *W*, it is able to provide around 3000 *s* of specific impulse with an efficiency larger than the 50% [103]. This means that (conservatively) a single PPS-5000 provides a thrust of 200 *mN*. These values are considered in Sec. 10 for the preliminary mission analysis.

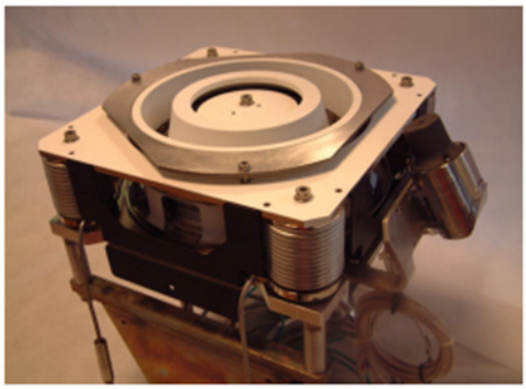

Figure 66: PPS-X000 technological demonstrator [103].

This thruster represents a typical Hall effect thruster with medium-high performance. It is worth mentioning again that, as we aim to deorbit as many debris as possible, the initial platform weight would be of thousands of kilograms. Thus, some hundred *mN* of thrust result in an acceleration magnitude of the order of *1e-4*; typical value for low thrust devices. Nevertheless, as the solar power generation system does not represent a big deal for Earth-close missions, two thrusters of the same kind are assumed. This doubles the required power and available thrust, which however remains always into the low thrust range, while still 3000 *s* are considered for the specific impulse.

8.2 Power and Mass Budget

The preliminary sizing for a foam-based debris removal mission, is here analysed assuming a Beginning-Of-Life (BOL) mass of the spacecraft of 4600 *kg*, as stated in the beginning of this section, considering the Soyuz launcher performance in 900 *km* Sun-synchronous orbit.

Starting from the assumption of an electric propulsion subsystem, in order to maximize the payload mass fraction, we can briefly assume some reasonable values for any system, thus obtaining the total mass of the spacecraft subsystems. This value represents the dry mass and it is considered, in Sec. 10, that the mission ends when this threshold is reached. Table 9 shows the spacecraft main subsystems and their approximate masses calculated as percentage of the dry mass [39]. The third column in Tab. 9 represents the subsystem mass shown in the second column where the 20% of contingency is added.

As rough estimation, here, we assume 1 *ton* of dry mass to start the analysis. This value, however, is here demonstrated a-posteriori to be a reasonable value. Indeed, as shown in Tab. 9, the total dry mass, inclusive of the 20% of contingency on each subsystem, is very close to the value assumed. In the same fashion, the power level for the platform has been considered in first instance, equal to 12 *kW*, and it is a-posteriori verified by means of the power budget. In Tab. 9, indeed, also the power required by each subsystem is summarized and in the rightmost column also this value plus 20% of contingency is given.

Subsystem	Mass [Kg]	Mass + Cont.(20%)	Power [W]	Power + Cont.(20%)
ADCS	100	120	100	120
C&HD	34	41	100	120
PGS	150	180	600	720

Structure	200	240	-	
SPS	178	214	10000	
ESS	30	35	-	
TCS	40	48	60	72
TT&C	60	72	100	120
G&N	30	36	80	96
Total	822	986	11040	11248
Available Mass	**3600**		**-**	
Available Power	**-**		**752**	

Table 9: Spacecraft subsystems preliminary mass and power budgets.

Let us investigate, now, more in detail how the mass and the power values of each subsystem have been estimated. For further details about the coefficients here used, the reader can refer to [39]:

- The Attitude Determination and Control System (ADCS), including both sensors and actuators, is required to stabilize and to orient the vehicle in specific directions during the thrusting or foaming phase. Its mass can be reasonably assumed as 10% of the satellite dry mass. The power estimated represents the 5% of operating power, a rather large value due to the large platform mass.
- The Command and Data Handling subsystem (C&DH), in charge of receiving, validating, decoding and distributing commands to other spacecraft systems, can be sized as about the 3.4% of dry mass. The power absorbed can be estimated, in first analysis, as the 5% of the operating power.
- The Power Generation System (PGS) is the power source of the spacecraft. Considering a power requirement of 12000 *W* and a density of 80 *W/kg*, the dry mass (without contingency) of the system is around 150 *kg*. The power generation system is estimated to require itself the 5% of the whole power it can generate.
- The Structure mass represents the physical support of all the other spacecraft subsystems. Here it is taken (conservatively) as the 20% of the dry mass. Obviously the structure itself does not need any power and the bus housekeeping power is already considered in the C&HD subsystem.
- The Spacecraft Propulsion Subsystem (SPS) is here considered composed of 3 main components and its weight is given by the sum of Tank, Thruster and Power Control Unit (PCU) mass. The total mass of this subsystem results around 178 *kg*. Considering two thrusters and 5000 *W* of power absorbed by each thruster, this subsystem requires up to 10000 *W*, of course the largest contribution to the whole power budget.
- The Energy Storage System (ESS) stores the produced energy in order to handle peak power needs for short times or in case of Sun eclipses. Considering a lithium battery of 5000 *Wh* and a specific energy density of about 170 *Wh/kg*, the ESS mass (without contingency) is about 30 *kg*. No power requirement has been estimated for the batteries.
- The Thermal Control System (TCS) has to maintain the spacecraft components and subsystems in their optimal temperature range. In terms of mass it requires just the 4% of the dry mass and in terms of power it requires the 3% of the operating power.
- The Telemetry, Tracking, and Command (TT&C) or Communication subsystem manage the communication between the spacecraft itself and the ground stations. It represents the 6% of the dry mass and it absorbs the 5% of the operating power.
- The Autonomous Guidance and Navigation (G&N) subsystem is required to determine satellite position and velocity and for pointing manoeuvre during the foam ejection. Its mass can be assumed about 30 *kg* and the power absorbed can be estimated to be about 80 *W*.

The available mass in Tab. 9 has to be allocated for the propellant mass, the foam with its tank and the foam ejection device. Obviously, the available mass is computed as the difference between the BOL mass and the dry mass. In a rough (and conservative) estimation, this mass margin is equally divided between the propellant and the payload. This means that each one of these can weigh up to 1.8 *tons*. This represents a first guess assumption and we consider this just as reference value. Indeed the foam and the propellant mass fractions depend on the particular mission and in general the available mass is not equally divided, but its subdivision depends on the debris sizes and their spatial distribution. The total payload is obviously composed of the foam itself and by the device needed to reach the debris and nucleate the ball, in particular, the robotic arm and the mixing nozzle introduced and sized in Sec. 9.

In Tab. 9, the available power represents the difference between the approximate value of the power level for the platform and the one resulting from the power budget of all subsystems. The power budget has been estimated considering reference values providing an order of magnitude for each subsystem. These values are given as percentages of the total operating power. This power has been assumed of 2000 *W* for all subsystems besides than for the PGS. The main reason is that the reference value estimates the power requirements on the platform bus power. This means that the TT&C or the ADCS are not really affected by the electric propulsion system. Accordingly, for all of these subsystems the power margin (2 *kW*) has been considered for the sizing as operating power. On the contrary, the PGS subsystem has to handle the whole power of the spacecraft. In this case the power requirements have been estimated considering the whole 12000 *W* available on board. Of course, the SPS assumes a constant value given by the two thrusters considered (see. Sec. 8.1).

In order to calculate the total power required by the spacecraft, we have approached a purely qualitative analysis. In fact, during its operative life, the spacecraft will operate in different conditions, and not all the subsystems will work at the same time. Furthermore, each subsystem does not require the total power indicated in Tab. 9 in all operative modes. This means that, depending on the specific mission phase, one of these can absorb a power in the range or even smaller than the one indicated in Tab. 9.

During the foam ejection operation, we need to take into account also the power required from the ejection device. Considering the total pressure drop and the mass flow rate (computed in Sec. 9) and assuming an efficiency of 20%, we can estimate that about 200 *W* are required during this operation mode. All in all, the total power required by the platform is around 12000 *W* that are sufficient even considering all the subsystem working at the same time. This power amount can be obtained with about 40 m^2 of independent, deployable, sun-tracking solar panels.

Considering the propulsion system already described in Sec. 8.1, with specific impulse of 3000 *s*, and 1800 *kg* of propellant mass, the total mission ΔV is approximately 1.4e4 *m/s*. Moreover, we can estimate that approximately the 11% of the total payload has to be allocated for the foam reservoir, the pressurization tank, the robotic arm and the ejection device, ≈200 *kg*. This means that the remaining 1.6 *tons* are available for the foam mass. With this quantity of available foam we can think to deorbit up to 5 debris of 800 *kg* from 900 *km* of altitude. This deorbited debris number has been roughly estimated considering such a kind of reference debris and the foam mass required to deorbit it, see Figs. 5-6.

In order to conclude this analysis, let us briefly address the volume required by the foam reservoirs on the platform. After the expansion process, the estimated 1.6 *tons* of foam, with a foam density of 1 kg/m^3 (see Sec. 7), fill 1600 m^3. Considering an expansion factor of 1000 (see Sec. 7) and assuming no mass losses, the compressed liquid foam components occupy, inside their tanks, a volume of 1.6 m^3.A reasonable value for the launcher so far assumed.

8.3 Chemical-Electrical Comparison

This platform preliminary sizing is here completed considering the comparison, in terms of subsystems masses and propellant mass fraction, between the electrical option chosen and a chemical one.

In general, the main relevant feature of electric propulsion methods is their high exhaust velocity. This makes such a method more suitable for the considered application, as the propellant mass required to realize a given total impulse significantly decreases if compared to chemical propellant mass. However, the drawback of electric propulsion systems is their high power-to-thrust values that causes, considering the standard power budget of a generic satellite, low thrust levels. As direct consequence this implies that longer times are required to deliver the same total impulse with the consequent problem of gravity losses. Nevertheless, electric propulsion systems remain the preferred choice, especially for missions requiring high total impulses, like the one in consideration where multiple transfers, from a debris to the next one, are required.

Considering, from the preliminary mass breakdown (see Tab. 9), that thermal, telecommunication, on-board data handling and attitude control system do not depend on the specific propulsion scheme chosen. The comparison is here made sizing the propellant mass fraction and the power generation system mass for the two cases. As the exploitation of a low thrust propulsion scheme increases the mission ΔV, a meaningful comparison considers the same performance of the two systems in terms of orbital manoeuvre. A given semi-major axis and inclination changes are here assessed in order to compare the two systems.

Equations shown in Sec. 10 provide the ΔV required for a given change in semi-major axis and inclination. Representative values for these variations are here assumed in order to carry out the chemical-electrical comparison. These values are defined as the maximum variations of these parameters in the SSO list. A total inclination change of 3 *deg* and an altitude change of 200 *km* are considered. The total ΔV, computed by means of Eq.(42), results 425 *m/s* for the electric case. A standard Hohmann transfer [17] with complete inclination change at the orbital apogee is, instead, considered to estimate the performance of the chemical scenario. In this case, indeed, a total ΔV of 362 *m/s* results, lower than the electric case, as expected. Now, from the Tsiolkovsky equation (Eq.(36)), these ΔV values can be related to the propellant mass consumption by means of the electric and chemical specific impulses. While for the electric one 3000 *s* are used (see Sec. 8.1), for the chemical one a realistic reference value of 250 *s* is assumed. In addition, for the electric propulsion configuration 10 *kW* are required only for the two thrusters. Assuming two additional *kW* for housekeeping and subsystem requirements, this implies that approximately 150 *kg* of power generation system mass are needed, see Sec. 8.2. For the chemical configuration, instead, the power requirement is much smaller and just a couple of *kW* are required, thus the power generation system mass is around 25 *kg*. In both cases, the same state of the art solar PGS power density of 80 *W/kg* has been considered [39]. The analysis so far described is represented in the two histograms of Fig. 67.

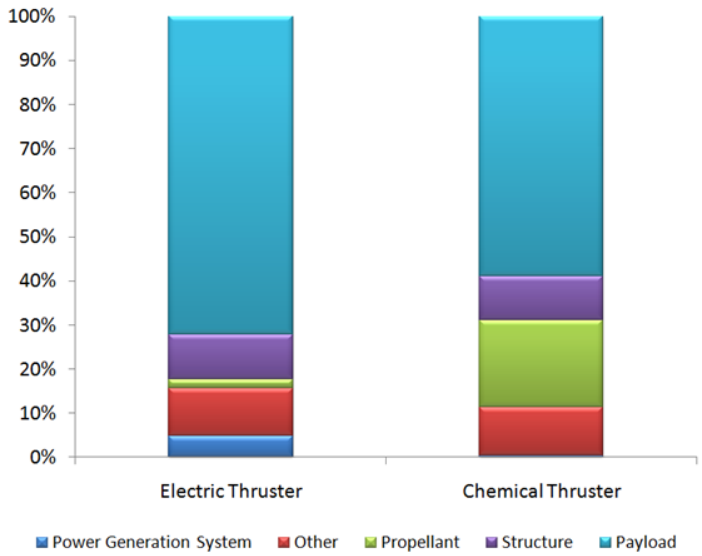

Figure 67: Comparison between electric and chemical propulsion system configurations.

As shown in Fig. 67, the electric configuration allows 600 *kg* of additional payload mass as the propellant mass is almost 10% of the one of the chemical configuration (from more than 900 to less than 100 *kg*) and the power generation system mass increases only by 125 *kg* (from 25 to 150 *kg*).

It is worth stressing that the above analysis is very conservative as only a single transfer between two target debris has been considered. Taking into account the whole mission, or even just several transfers, the performance of the electric scenario would be even better.

9 FOAM NUCLEATING SYSTEM

The kind of foam identified in Sec. 5, may be originated by the mixing of two components. These, upon mixing, give rise to a chemical reaction that starts the polymerization process. The foam is then ready to expand and cure. A mixing device has then to be foreseen in order to allow the foam to start the reaction before leaving the platform and expanding on target debris. In order to simplify (limiting the number of possible failure modes) and reduce the weight of the structure, it is possible to think to a static mechanism, namely a mixing chamber and/or a mixing nozzle, as the easiest way to mix the two components. These devices have to be able to mix the two components when they flow through it.

In this section we propose several solutions for the foam nucleating and attaching strategy and we ponder their advantages and drawbacks in order to define the more suitable one. All of these are however based on a static mixing system since we aim to reduce the overall system complexity. Obviously the foam can not expand inside the spacecraft, but the foaming process needs to occur on the debris surface or in proximity of this one. For this reason, the possible geometries are conceived so as to satisfy this requirement. Furthermore, the device should be also able to provide a controlled environment (especially in terms of pressure) if the specific foam nucleation process might require.

Furthermore the device has to be able to approach the debris and cover its surface to the larger extent in such a way that the resulting foamed object resembles a sort of foam ball, thus the foaming coverage should be as regular and distributed as possible.

The foam nucleating systems described in Sec. 9.1 represent just four of a wide selection of possible devices. These are all driven by the necessity to remove the largest number of debris per year and to reduce overall risks and costs of the mission. Moreover, the methods here presented, have to be intended (and have been conceived) as *remedial methods*.

For future launches, however, it is possible to consider a simplified version of the same methods as mitigation measures to limit post-mission orbital lifetimes. In these terms, it would be possible to equip future spacecraft with some tanks filled with a quantity of foam sufficient for the self-deorbiting. These tanks should be able to be activated at the end-of-life of a given satellite. From this point of view, this kind of device can be also intended as *preventive method* [104]. Equipping all future satellites with such a kind of passive, drag augmentation, foam-based, self-deorbiting devices would avoid the increasing of the space debris population and it would not require the foam nucleating system here presented.

9.1 Device Concepts

The proposed foam attaching methods are here presented. A brief description of the four main candidates is provided in the following:

1. ***Chameleon Tongue***: debris may be approached by the platform using an elastic wire or a sort of retractable tape. This is launched towards the debris with one side of the wire attached to the spacecraft and the other one attached to a vessel containing the mixing chamber and the reservoirs filled with the two foam components. These reservoirs feed the mixing chamber required to generate the needed foam. The box, composed of these tanks and the mixing chamber, is left on the debris surface and the retractable wire goes back to

the spacecraft. This type of device should not be hard to develop, as it can be developed with state of the art technology, but it might be not really effective for those debris with a considerable angular rate.

2. ***Foam Ejection Nozzle***: the spacecraft is equipped with a nozzle from where foam is ejected on the debris surface. This device may also be combined with a robotic arm capable of reaching the debris in a more precise way and covering its surface from various positions. Also in this case, no particular technology has to be developed, as many components of this kind have already been used in space, even if for different purposes [105].
3. ***Satellite Swarm***: a constellation of satellites is equipped with a small nozzle foam ejection system. These satellites are able to cooperate in order to surround the target debris completely covering its surface. In this way it is possible to ensure the almost-total coverage also for large debris. Furthermore, each satellite, or subgroup of satellites, can also work by itself acting on smaller debris in close regions. As above there are not new technology to develop, unless the difficulty of coordinating several satellites. Furthermore these small satellites can carry only a limited amount of foam mass, thus a replacement system or a refill orbiting platform should be considered as well.
4. ***Foam Gums***: gums are a kind of reservoir filled with the two foam components. They are able to mix these two components, so that the polymerization process can start. Moreover, they have to release the foam once they have been shot on the surface of the debris. In order to hit the debris surface, the spacecraft may be equipped with a gum-gun firing these reservoirs. The cannon-like device should be able to precisely target a given debris.

It is worth stressing once more that it is possible to conceive simplified versions of the above-described approaches as preventive methods. In this case the spacecraft can be equipped with self-destruction tank filled with foam. To realise this kind of preventive method there is not necessary to develop or create particular technologies. Indeed, the tank should be equipped only with two reservoirs for the foam component and a static mixing chamber, see Figs. 68-69. At the end of the spacecraft life, the reservoirs release the liquids in order to increase its area and consequently deorbiting itself in a reasonable (a-priori stated) time.

9.2 Issues

After the brief overview of the proposed foam nucleating and attaching methods, this section is devoted to investigate more in detail the possible issues arising in these methods. Furthermore also some deeper descriptions of the more relevant devices are provided.

Dealing with the chameleon tongue, a more accurate description of the working principles is required in order to understand the issues related with this scheme. Indeed, it is important to define the minimum and maximum distances from the debris where the method is able to operate. This means to define a threshold for the retractable wire length. The tongue is conceived as a tether or a tape, objects already widely used in space [106]. Tethers are sort of long cables used to couple multiple spacecrafts or release a mass [107]. They are generally made of strands of high strength fibres or conductive wires. For the preliminary design of the chameleon tongue, we refer to the state of the art of existing retractable tethers. Nevertheless, some additional features are required for the specific system under consideration. The release mechanism, in particular, is supposed to be equipped with a spring-loaded reel that dispenses and controls the wire length. The active reaction device relies on an electric step motor of few *W* directly mounted on the wire reel. A friction brake

and a spiral spring provide a passive retraction system supposed added to the classic active device. In this way the tether retraction is allowed even without consuming any power [107].

As an example of possible devices, and in order to define a maximum length for this tongue, we refer, specifically, to a retractor with the following characteristics [107]:

- The retractor is able to bring about 250 *kg* of mass at 1.2 *m/s*. In our specific application, the weight that the cable has to support depends on the quantity of foam necessary to the covering of different size debris. The container to be released is rather simple. It is composed of the external bus, the two reservoirs and the mixing chamber and/or nozzle. In total, including also the tether, it is estimated that the whole system weights less than 50 *kg*. Thus up to 200 *kg* of foam can be released on the debris surface. This would imply that a single ball of 41 m^2 is produced. If necessary, with large debris, more than a single reservoir shall be released.
- The retractor is able to contain a tether length up to 16 *m*. This size does not represent a particular challenge for space tether applications and realistically could be deployed without particular troubles. The minimum tether length is related with typical problems and risks due to the rendezvous between two objects in space. For the sought application, however it is not required to be too close to the target object in order to have the method working.
- As previously mentioned, the assumed retraction system is passive and the system offers a maximum retraction rate of 0.15 *m/s*.

The reservoir is attached on the free side of the tether and, when it is released on the surface of the debris, the mixing device starts working to produce foam. The attachment is an open question, this because it can be realized in different ways depending on the target size, orientation and the building materials. As example, for large debris a good solution could be a sort of gripper or anchor. A magnetic attachment could be another solution, but this is not possible for non-magnetic debris. Moreover, in more simple way, the reservoir can be soaked with adhesive.

With regard to the foam gum method, we have to define how many reservoirs are required for each debris with respect to its dimensions. In vacuum an expansion factor of about 1000 is estimated, see Sec. 6. Therefore, as example, considering a cubic container of 10 *cm* side, it produces 1000 *l* of foam. This means that, in order to encompass very large debris, we need more than a single container. The cannon-like mechanism mounted on the platform will be able to shot one container after the other, or to fire multiple-shots. Probably the major issue of this method is related to the momentum of these gums that would be transmitted to the debris. This might cause, besides an increasing in the tumbling of the object, also a slightly change of its orbit. This occurs especially for debris witch dimensions are comparable with the reservoir dimensions. For this reason we need to ensure a sort of “soft impact”. It is possible to realise a controlled shoot in order to impress a small thrust to the reservoir in order to ensure a small closing speed, but this seems the main open point of this method.

Figure 68 represents an example of the container scheme. This can be used for both the chameleon tongue and the foam gum, where just the attaching system changes.

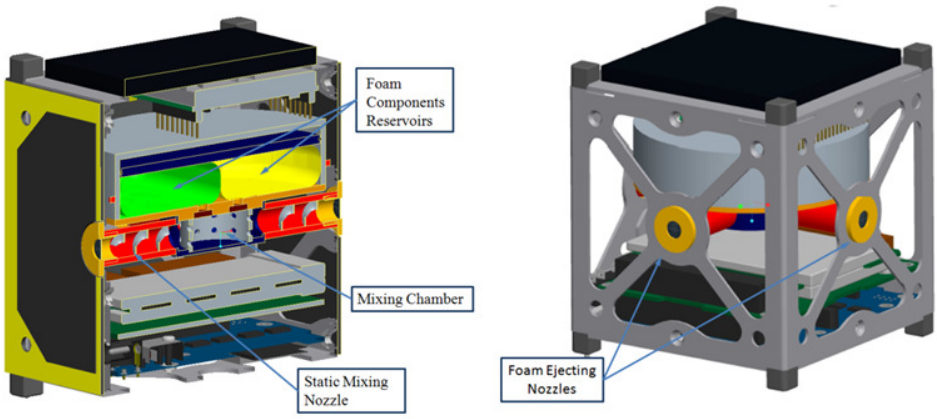

Figure 68: Example of container scheme. On the left a cross section of the rightmost figure is shown in order to display the mixing nozzle, the two reservoir and the mixing chamber.

On the left of Fig. 68 a cross section on the container is shown. Here we can clearly see the two foam components reservoirs, the mixing chamber and the static mixing nozzle. On the right of Fig. 68, instead, an example of the container itself is represented with the foam ejecting nozzles. Figure 69, moreover, is an artistic depiction of the beginning of the foaming process. Obviously this is only a qualitative representation of the process.

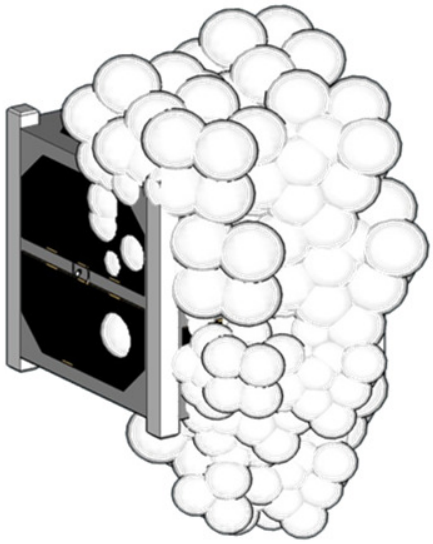

Figure 69: Schematic representation of starting foaming process nucleating from the vessel delivered by the chameleon tongue or the foam gum method.

The main issues of the foam ejection system, instead, are connected with the cone semi-angle shaping the flow and with the dispersion of the "drops" of foam. The opening angle of the cone is connected with the flow speed and with the reaction time of the foam. The higher the flow velocity the smaller the opening angle, while the lower the expansion time the larger the opening angle.

The nozzle here considered is a static mixing nozzle, in the sense that it is a sort of mixing channel into which the two liquids are mixed, like the ones shown in Fig. 70. The length of this chamber is limited by the polymerization time of the foam. In fact, the expansion needs to occur after the foam has been ejected, near the surface of the debris in order to cover it in the best possible way.

Figure 70: Two models of static mixers [108].

In this method, the nozzle is supposed to be mounted on a robotic arm. This arm can be realised as a retractable arm that should be deployed only during the foam nucleation phases and retracted during the transfers. The length is dictated by the radius of foamed debris. In fact, when the spacecraft moves near the debris, for the foam attachment, a remote probability that the foam encloses (at least partially) the spacecraft itself exists. This probability is connected with the relative closeness of debris and platform. As an example, considering 8.2 *tons* debris (one of the largest debris here considered), the dimension of the foamed ball, necessary to its deorbiting (see Sec. 4), would be smaller than 12 *m*. Therefore, 15 *m* as length of the robotic arm is a conservative assumption. This size is used to asses in detail the performance of this system in Sec. 9.4.

Many of the issues related to the foam ejection nozzle are directly applicable to the satellite swarm concept. On one hand, in this method, each satellite is very small, thus it is not possible to mount a robotic arm. On the other hand, their small size allows manoeuvre times smaller than the spacecraft equipped with a single nozzle. With this regard, a possible improvement of the foam ejection nozzle device can be represented by multiple arms or limited manoeuver capabilities of these, both solutions significantly increasing the overall system complication. Considering that the expansion time for the foam in vacuum could be substantial (see Sec. 6) and takes place in some hours, the satellites need to move away after the foam ejection within this time. Generally, we can also argue that, if one or more satellites would remain enclosed into the foam ball, it would not be a catastrophic event, due to the large number of swarm elements and their possible fast replacement.

A common problem, of both the nozzle and satellite swarm mechanisms, is the cleanness of the nozzle. In fact, after the use, it is important to scrape off the polymerised foam in the duct in order to prevent the blockage. The foam ejection velocity could help in this process, however this velocity can not be too high, because it can generate a negative thrust capable to outdistance the spacecraft from the debris, see Sec. 9.4. This issue can be easily faced by considering ventilation of the ducts after the foaming process, e.g. by means of some inert gas, so as to wipe out possible foam incrustations. Furthermore, due to the very low weight of the mixing nozzle, a cold redundancy can be easily conceived.

Dealing with this approach, it is worth mentioning at least another ejector concept; the electrostatic spray. Both the robotic arm and the satellites swarm can be equipped with this kind of device. In an electrostatic spray, the two mixed liquids are negatively charged and accelerated by a potential difference to be created between the liquids and the target debris. With this method it would be possible to direct the foam flow, control the deposition rate, control the pattern size, shape, and density of the spray [109]. This device is largely used for ground-based painting applications, thus it could be developed with state of the art technology. Nevertheless, this solution seems to be too elaborate, heavy and expensive [109] if compared to the nozzle device.

9.3 Characteristics Identification

The aim of this section is to carry out a qualitative analysis to estimate, as first approximation, the best option among the proposed foam attaching devices. The choice is based on the study of the main characteristics necessarily required for the foam-based removal system. These characteristics are:

- *Reliability*: in terms of all risks connected to the mission. Moreover, even if the device reliability influences *Effectiveness*, they have been here separately considered in order to isolate these two aspects.
- *Technological issues*: this characteristic represents the innovation with respect to the state of the art and all the general complications connected to the realization of the system.
- *Flexibility*: with this aspect we refer to the capability of the system to cover debris with different sizes, forms and orientations.
- *Cost*: in terms of launch cost, general cost of the spacecraft, foam nucleating and attaching mechanism.
- *Effectiveness*: here we refer to the efficacy of the foaming process and to how many debris per year it is possible to remove.

All of these characteristics are assumed to have the same relative weight, thus the same importance. At this point it is possible to fill a decision matrix (Pugh Matrix) based on these aspects and the foaming systems proposed. Assigning a grade between 1 and 10 for each characteristic and for each type of ejection devices, it is possible to establish which one of these is the most suitable one, see Tab. 10. The score is assigned so that 1 corresponds to the worst situation and 10 represents the best one. In Tab. 10, the single scores for each ejection device and for each characteristic are shown together with the total score and final ranking.

	Chameleon Tongue	**Nozzle**	**Satellite Swarm**	**Gum**
Reliability	6	7	7	5
Technological Issues and Feasibility	5	8	4	6
Flexibility	4	6	8	4
Cost	7	7	4	7
Effectiveness	6	7	8	5
TOT	**28**	**35**	**31**	**27**

Table 10: Foam ejection decision matrix: main characteristic vs. ejection devices.

According to this qualitative analysis, the best option seems to be the foam ejection nozzle, closely followed by the satellite swarm. Instead, the gum and the chameleon tongue do not represent good choices. Indeed, in terms of capability to cover debris with different forms, orientations and sizes, i.e. in terms of flexibility, they can encounter some difficulties. For the chameleon tongue, the tether aim only a fixed direction, this means that, in order to totally cover a very large debris, are needed more than one manoeuvre. The same occurs for the gum, because the cannon can shoot only on the visible surface of the debris and, also in this case, more manoeuvres are needed.

The foam gum has not a good reliability, due to the risks connected with the impact between the reservoir and the target. As previously said, this kind of device can encounter problems with small

debris, which size is comparable with the reservoir one. The low grade assigned to the technological issues of the chameleon tongue is conservatively assumed due to the not really successful heritage of tethers in space. Concerning the costs, these kinds of technology are not really expensive, in relation to the other devices, like the satellite swarm concept that is considered to be the most expensive one.

Therefore, the nozzle system is here considered to be a good solution in terms of technological issues, costs, reliability and effectiveness. In fact, as previously said, there is no particular technology to develop for this kind of devices. For the same reason it is assumed to have a good reliability and reduced costs. Dealing with the flexibility of this device, it has a smaller score than the other characteristic. This happens because, even if the nozzle is combined with the robotic arm, in presence of large debris, the total coverage of its surface with one single manoeuvre should be almost unlikely. Instead, this problem does not occur with the satellite swarm concept. In fact, the swarm elements can easily surround the debris providing good foam coverage simultaneously. Even in terms of effectiveness the satellite swarm approach has a higher score, due to the presence of more satellites able to work on more small debris at the same time, instead of one satellite that obviously can work only with a single debris at a time. Considering only these two characteristics, the satellite swarm could seem to be a good solution, but, as Tab. 10 shows, this device might have high costs and it is more complicate than the other devices. For these reasons, the choice falls on the foam ejection nozzle. This solution is explored more in detail and roughly sized in the next section.

9.4 Preliminary Design

Since, from the above considerations, the foam ejection nozzle results the best option, the aim of this section is to explore in detail this mechanism. A preliminary design and a rough estimation of its performance are here provided. The idea is to realise the foam ejection nozzle equipped with:

- Two reservoirs, one for each foam component.
- Two ducts, to feed the mixing chamber with the two components.
- One mixing nozzle, acting as static mixing device where the foam nucleates.
- A pumping system, to let the components flowing through the ducts.
- A robotic arm, where the ducts are mounted on and able to reach the target debris.
- A pipe flushing system in order to ensure the cleanness of the nozzle.

The pumping system pushes the two liquid components, which initially are in the reservoirs, through the ducts up to the mixing chamber, at the tip of the robotic arm, where the foam is nucleated and thereafter ejected. The ducts are two flexible pipes mounted on the robotic arm. The arm is conceived as telescopic or articulated in order to be folded during the launch, transfers and non-operative phases. The mixing nozzle is a cylindrical duct in which the two liquids are forced to flow through a tortuous passage, in order to realize a static mixing. The final part of this chamber is an appropriate nozzle-shaped duct. Figure 71 shows a schematic representation of the device.

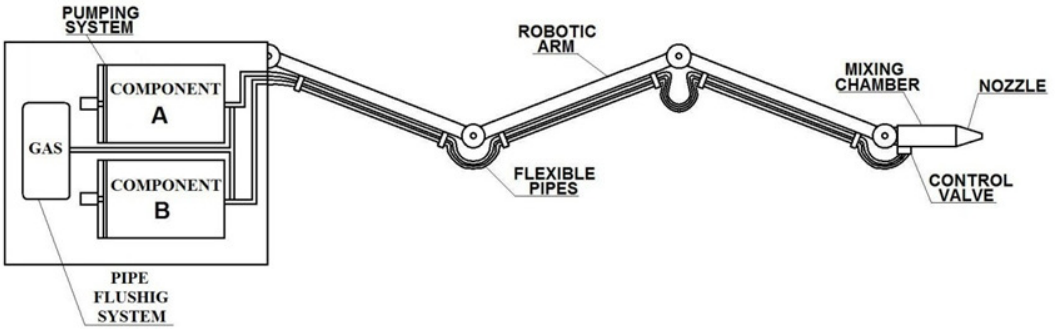

Figure 71: Schematic design of the foam ejection nozzle on the extendible robotic arm.

The static mixing option has been chosen according to the wide selection available for (ground-based) industrial purposes. Examples of the most commercially significant mixers are the SMV, SMX, SMR, KMS, KMX, etc [110]. Each of these is suitable for a specific application, but a detailed description of the main characteristic of each model is far beyond the scopes of this section, thus in the following a generic one is considered. In particular, the one here considered is described as suitable for laminar flows and high viscous fluids [110].

Figure 72 shows the mixing of the two components passing through a static mixer as modelled by a multiphysics software (*COMSOL*) [111]. The phases (blue and red colours in Fig. 72) are forced to mix by the multi-helical structure inside the pipe, represented on the right hand figure, up to obtain a uniform mixture.

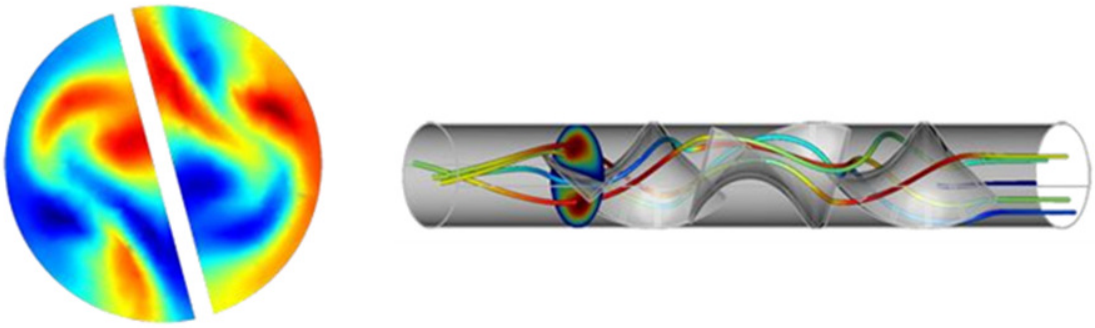
Figure 72: Static mixer working scheme. On the left a cross section showing the two phases (red and blue) mixing at the section plane indicated in the rightmost plot where also streamlines of the two phases are shown [112].

In order to carry out the preliminary sizing of the static mixing chamber, let us consider the equations for the behaviour of fluids in pipes and mixing chambers [110]. The pressure drop in a static mixer of fixed geometry, for laminar and turbulent flow, can be respectively modelled by:

$$\begin{cases} \Delta P_{sm} = K_l \Delta P_{pipe} & \text{laminar flow} \\ \Delta P_{sm} = K_t \Delta P_{pipe} & \text{turbulent flow} \end{cases} \tag{37}$$

Where K_l and K_t are given coefficients (related to the mixer geometry and provided in the mixers data sheets) for laminar and turbulent flow and ΔP_{pipe} is the pressure drop through an open pipe with the same diameter, D, and length, L. The pressure drop in a duct can be generically expressed as function of the velocity V by [110]:

$$\Delta P = 4f\frac{L}{D}\rho\frac{V^2}{2} \tag{38}$$

where f is the friction factor. It is a non-dimensional parameter applied to model fluid friction in pipes. It is related to the pipe diameter, the pressure drops, the fluid kinetic energy, the pipe length and its surface roughness. For laminar and viscous flows it is given by [110]:

$$\begin{cases} f = \dfrac{64}{\mathrm{Re}} & \text{laminar flow} \\ f = \dfrac{0.079}{\mathrm{Re}^{0.25}} & \text{turbulent flow} \end{cases} \tag{39}$$

where *Re* is the Reynolds number.

Let us introduce now the *CoV* coefficient of variation [110,113]. It represents the ratio between the standard deviation of concentration measurement and the mean concentration. This is also called the intensity of mixing or degree of segregation. By way of example, in a typical industrial mixing process, an additive might be considered well mixed at 5% *CoV* [110]. The final *CoV* is usually independent of the amount of components to be mixed, thus the foam quality resulting from the mixing nozzle system is not dependent from the debris size.

As the aim is to define the length-to-diameter ratio of the mixing nozzle, the relative *CoV* reduction coefficient is required. This CoV_r can be, indeed, directly related to the *L/D* ratio [110]. *CoVr* can be both given by the ratio of initial and final *CoV* value ($CoV_r = CoV/CoV_0$) and by a *Ki* coefficient elevated to the *L/D* ratio. Namely [110]:

$$CoV_r = K_i^{L/D} \tag{40}$$

Here K_i is a given coefficient and it depends on the mixer type and laminar or turbulent flow regime. Actually, this coefficient is strictly related to the Reynolds number of the flow, see Fig. 73.

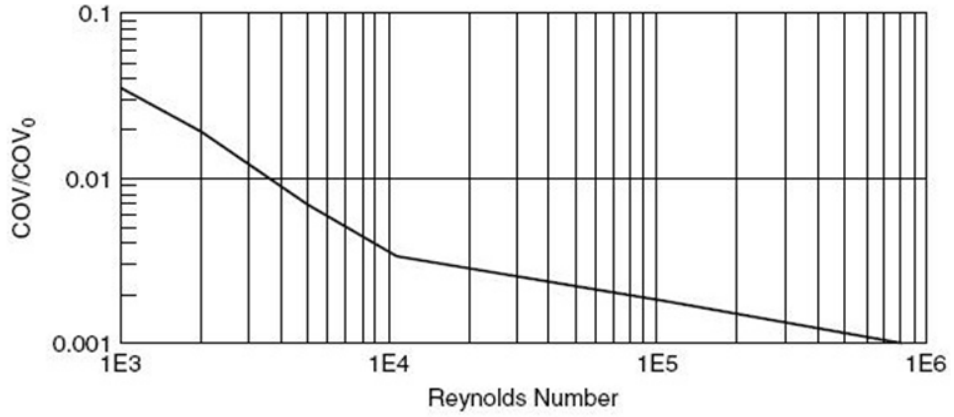

Figure 73: CoV_r trend with respect to the Reynold number [110].

Therefore, from the knowledge of the *Ki* and *CoVr* it is possible to find the *L/D* ratio, by means of Eq.(40). For low Reynolds numbers (less than 1e3) the CoV_r is assumed constant at 0.035 [110]. This is particularly important as the *Re* we expect in our application is below the minimum of the plot of Fig. 73.

In order to apply these relations to the case under consideration, let us consider (as already done in Sec. 6) the ESPAK 90 polymeric foam [116]. The values for the viscosity and density, for the two components are listed in Tab. 11:

	Component A	**Component B**
Viscosity at 25°C (*mPa s*)	670	200
Density at 25°C(*kg/l*)	1,1	1.23

Table 11: Viscosity and density values of the two-components of the ESPAK 90 foam [116].

The nozzle sizes and the exhaust velocity are here assumed in order to have a relatively small nozzle and a reduced foam ejection velocity. As previously mentioned, the exhaust velocity can not be too high, since it can generate a negative thrust and a too large nozzle could cause foam dispersion around the debris.

Considering a diameter for the static mixer of 0.05 m, and an exhaust velocity of 0.3 m/s, the Reynolds numbers for the two components result to be, respectively: Re_A=24 and Re_B=93. This means that the flow is laminar in both cases and the 0.035 value for the coefficient of variation reduction can be assumed. The specific reference static mixer considered is the SMX series [110]. Its K_i and K_l parameters, required to estimate CoV_r and L/D, are [110]: K_i=0.63 and K_l=37.5.
With these values, the pipe length and the resulting pressure drops are:

$$\begin{aligned} L &= 0.36\,m \\ \Delta P_{sm} &= 27269\ Pa \\ \Delta P_{pipe} &= 30067\ Pa \\ \Delta P_{tot} &= \Delta P_{sm} + \Delta P_{pipe} = 57337\ Pa \end{aligned} \tag{41}$$

The ΔP_{tot} directly represents the pressure needed for the pumping system in order to generate the desiderate exhaust foam velocity. A conservative value for ΔP_{tot} could be 100 kPa and by means of a regulating a valve it is possible to control the pressure upstream the mixing pipe.

The length obtained from the sizing, seems to be a feasible value, compared to the state of the art for static mixers already used for several applications and also compared to the robotic arm length assumed (15 m).

The thrust generated by the exhaust foam velocity is lower than 0.2 N and this does not represent a particular issue. Indeed, if the spacecraft is equipped, as conceived, with an electric thruster, it is possible to generate a thrust equal and opposite in order to keep the spacecraft itself fixed during the ejection. By way of example, let us consider the thruster identified in Sec. 8, the PPS-5000. It generates a specific impulse of 3000 s [103] and a corresponding thrust of 0.2 N, as desired.

A very last consideration can be done about the choice of the static mixer. Considering another type of pipe, the values of K_i and K_l change [110] and consequently also the final length of the pipe itself. Implementing the mathematic model, above described, for different mixers, we can see that the pipe length and the total pressure drop change just slightly, indeed they remain in the same order of magnitude of the values here computed.

The static mixers considered here are realized for ground application. For this reason, in future, it can be considered to develop an ad-hoc space version of such devices. This would lead only to an increase of the performance, probably in terms of smaller mixer and/or tank pressure.

10 MISSION ANALYSIS

In this section we apply the assumptions made about the platform design, Sec. 8, and the foam characteristics, Sec. 7, to carry out a preliminary analysis of a mission for active removal of space debris. Focusing on the platform duties, each phase of the mission scenario depicted in Sec. 1.3 is here assessed by means of analytical approximations in order to estimate the velocity increment ΔV needed to acquire a target orbit. The space debris lists presented in Sec. 3 are then used as test-beds, in order to estimate the method capability in terms of number and mass of debris removed, as function of the number of missions needed to completely clean up one of the regions portrayed by those lists.

In order to implement the preliminary low thrust mission analysis among so many objects, some assumptions are adopted:

- At the beginning of each mission, the platform is released by the launcher on the exact orbit of the first target, so no orbital manoeuvre has to be performed. This means that, for the first targeted debris, the only task to be performed is the debris foaming.
- The orbits of debris are considered unchanged for the whole time needed to target each debris, i.e. no drag or Earth oblateness perturbation (J2 effect) is considered during the low thrust transfers neither for the debris nor for the platform.
- Platform orbit is always accounted as circular and, since the orbits of debris listed in Sec. 3 present very small eccentricities, the same assumption also holds for target debris. This motivates to neglect the argument of perigee change manoeuvre.
- No orbit phasing is considered to adjust also the platform true anomaly with respect to the one of the target. This assumption seems reasonable, since a more sophisticated thrusting strategy would definitely allow avoiding further manoeuvers.
- The time needed to encompass the debris with foam is neglected with respect to the time needed for orbital manoeuvres.
- The mass of the spacecraft is considered constant during each orbital manoeuver and its value is obtained as the average between the mass at the beginning and at the end of the thruster operations.
- The platform trajectory is obtained by the semi-major axis and inclination change manoeuvre followed by a RAAN change.
- The natural change of the orbital RAAN, due to J2 effect, is neglected both for the platform and for the debris. This assumption results in a conservative mission profile, since it is always reasonable to assume a thrusting strategy capable of exploiting this perturbation.
- The total manoeuvre cost is obtained as the maximum velocity increment between the one necessary to perform the combined semi-major axis and inclination change and the one for the RAAN change manoeuvre. This assumption still provides reasonable results considering the previous considerations about natural RAAN drift.
- Since the platform is expected to spend most of its lifetime in the highest layers of the atmosphere, the atmospheric drag perturbation is neglected for the purpose of this analysis.

10.1 Mission Profile

Considering the assumptions listed before, it is possible to describe the mission profile as a sequence of predefined manoeuvre, each one assessed by means of a first order approximation to actively remove each target debris. The selection of the debris sequence is based on the comparison of the manoeuvre cost (computed, as already stated, as the maximum velocity increment between the one necessary to perform the combined semi-major axis and inclination change and the one for the RAAN change manoeuvre) for all debris of the list.

In particular, the ΔV required for the combined semi-major axis and inclination change is assessed by means of the analytic Edelbaumm approximation [114]:

$$\Delta V = \sqrt{V_0^2 - 2VV_0 \cos\left(\frac{\pi}{2}\Delta i\right) + V^2} \tag{42}$$

where V_0 and V represent, respectively, the orbital velocity on the initial and final orbit and Δi is the desired inclination change angle. It considers a constant acceleration to compute the low thrust transfer velocity increment between two circular inclined orbits by linearizing the Lagrange Planetary Equations around a nominal circular orbit [114].

The other manoeuvre that can not be neglected deals with the RAAN change. It can be analytically approximated by [115]:

$$\Delta V = \frac{\pi}{2}\sqrt{\frac{\mu}{a}}\left|\Delta\Omega\right|\sin(i) \tag{43}$$

where a is the orbit semi-major axis, i its inclination and $\Delta\Omega$ the desired change in RAAN. This manoeuvre is performed using out-of-plane thrusting with burn arcs centred about the apices (i.e., the maximum and the minimum latitude points) under the assumption of almost circular orbits [115].

Once that these values have been assessed, the mass of propellant needed to perform each of these manoeuvres can be computed by means of the Tsiolkovsky Equation, see Eq.(36).

It is, moreover, possible to assess the time needed to perform each manoeuver, under the assumption of constant acceleration, by means of:

$$\Delta t = \frac{\Delta V}{\bar{a}} = \frac{\Delta V}{T}\bar{m}_{SC} = \frac{\Delta V}{T}\left(m_0 - \frac{m_p}{2}\right) \tag{44}$$

where $\bar{m}_{sc}$ is the average spacecraft mass, m_0 the value of the spacecraft mass at the beginning of thruster firing and $\bar{a}$ the resulting average acceleration on the spacecraft.

For each targeted debris, the mass of foam required to deorbit it can be computed considering the value of the foam density identified in Sec. 7 and the volume of the ejected foam. This value is obtained as the difference between the volume of the debris after and before the foaming process. Since the shape of target debris is unspecified, both the foamed debris and the specific debris are assumed as spherical objects. Under this assumption, the original debris volume, V_D can be estimated as:

$$V_D = \frac{4}{3}\pi\left(\frac{A_D}{\pi}\right)^{\frac{3}{2}} \tag{45}$$

where A_D represents the average exposed area of the target debris. The final volume of the foam ball, instead, is calculated by taking into account the optimal value of the ball radius for the target debris computed in Sec. 4. Once that the ejected foam volume is obtained, assuming for the foam density 1 kg/m^3, see Sec. 7, the foam mass can be estimated and subtracted from the platform mass.

10.2 Results and Considerations

Considering the so far outlined mission analysis approach, the three different lists and the optimum foam ball radii, identified in Sec. 4, have been used to assess the performance of the method in terms of number of debris targeted per year and deorbited mass. The results of this section are definitely not affected by the foam expansion factor but from the foam characteristics point of view, the main relevant factor is the density before and after its expansion. Indeed, the foam expansion factor only affects the platform geometry, see Sec. 10.

The initial value of the platform inclination has been obtained by means of a coarse grid on this value and considering the one resulting in the largest number of debris deorbited per year and the smaller number of missions required. A medium atmospheric density scenario is considered for the three lists (see Sec. 2.2), then the optimum ball radius values corresponding to this scenario are used.

Figure 74 shows the mission profile for the mission applied to the DISCOS debris list.

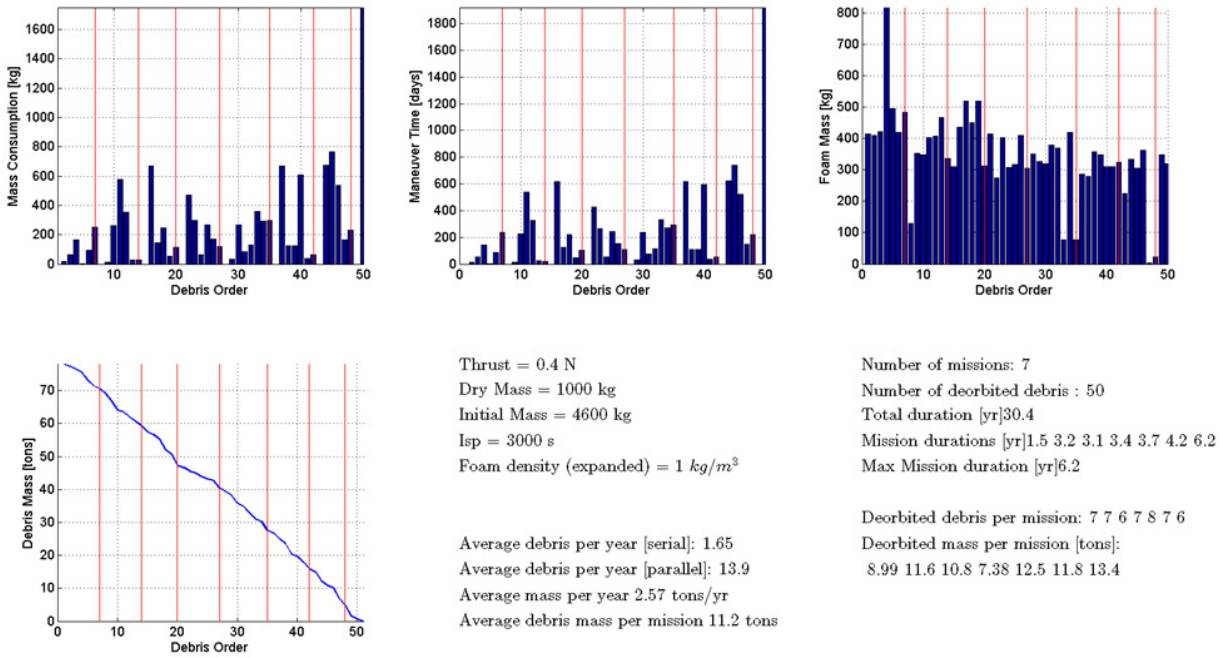

Figure 74: Mission analysis result for the DISCOS list in the medium density scenario. From the upper left corner: platform mass consumption, manoeuver time, foam mass and total mass of debris to be still deorbited trends with respect to the debris index number.

The plots in the upper row of Fig. 74 show the mass consumption due to electric thruster operations (left), the time needed to perform the required manoeuvre (centre) and the foam mass needed to foam each debris (right). The plot in the lower row shows the mass of debris still in orbit with respect to the mission profile. The vertical red lines in each plot show the separation between a mission and the next one. A mission is intended to be over if the sum of propellant and foam used has reached the total amount allocated for the two quantities, i.e. 3.6 *tons*. Since the beginning of each mission there are more debris to target, the propellant mass cost is typically lower than the foam mass cost. For this reason some missions, especially the first ones, present higher values of foam mass consumption and small values of propellant mass consumption. On the contrary, last missions present higher values of the propellant mass consumption and require much more time to be completed due to the small number of debris yet to target. Considering the DISCOS list, 7 missions are sufficient to target 50 debris in about 30 *years*. This value can be much smaller (6 *years*) if all the missions are performed at the same time, i.e. in parallel with multiple deorbiting platforms. On average each mission reaches 11.2 *tons* of debris with an average value of 2.57 *tons/year*. Assuming to start each mission at the end of the previous one, slightly less than 2 debris are targeted during one year. This value strongly increases, up to about 14, if we consider to perform all the missions at the same time.

The same approach can be, thus, applied to the other two lists. Figure 75 shows the results of the mission analysis applied to the proprietary SSO list.

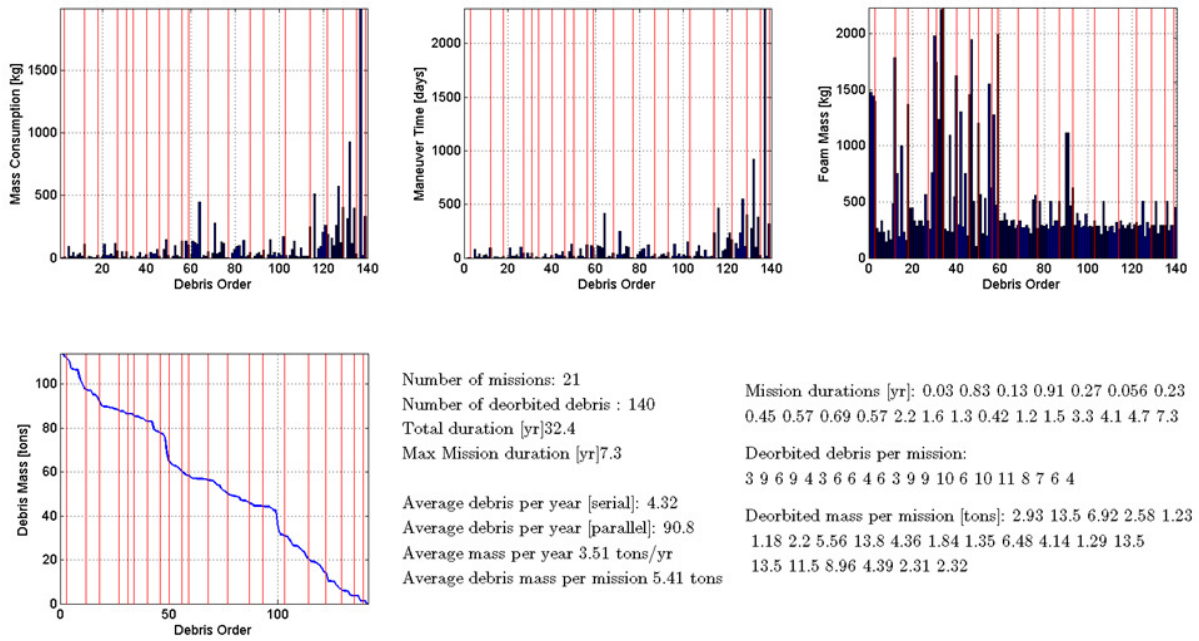

Figure 75: Mission analysis result for the proprietary SSO list in the medium density scenario. From the upper left corner: platform mass consumption, manoeuver time, foam mass and total mass of debris to be still deorbited trends with respect to the debris index number.

In this case 21 missions are required to target 140 debris. Every year, assuming to perform the mission in series, 4.32 debris are targeted on average with an average mass value of 3.51 *tons* of deorbited debris. Each mission on average targets 5.41 *tons* of debris. Also in this case some missions show large values of the foam mass required, while some others require more propellant mass and time to be completed. It is worth noting, once again, that if several parallel missions are carried out at the same time, the average number of debris targeted per year grows up to 90.8 and 7.3 *years* could be sufficient to complete all the necessary missions.

In this case the high number of targeted debris per year is mainly due to the large number of debris available in the list and their relatively close orbital element values. Actually this represents a complete SSO-tailored active debris removal mission.

Of course, the same methodology can be applied to the last list described in Sec. 3.1, the UCS one. The results are shown in Fig. 76.

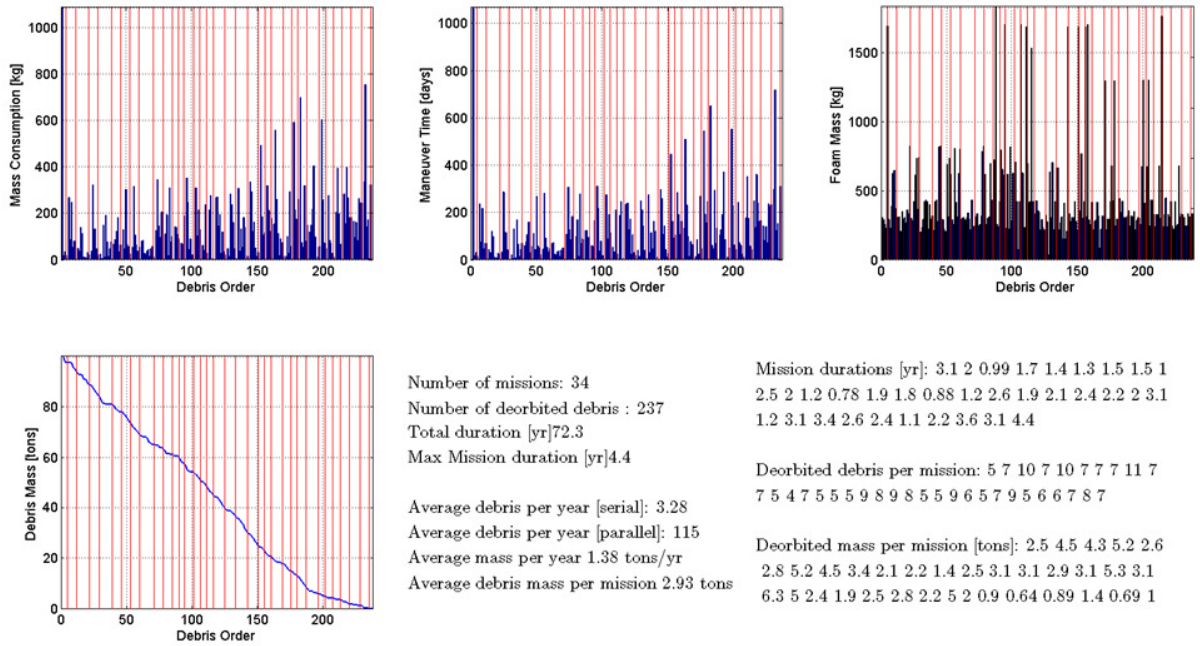

Figure 76: Mission analysis result for the UCS list in the medium density scenario. From the upper left corner: platform mass consumption, manoeuver time, foam mass and total mass of debris to be still deorbited trends with respect to the debris index number.

The more crowded UCS list, requires 34 missions in order to reach all the 237 debris. Assuming again to perform one mission after the other, 3.28 debris can be targeted each year on average with a corresponding value of the debris mass per year of 1.38 *tons/year*, so each mission is sufficient to target 2.93 *tons* of debris. On the contrary, considering several (34) parallel missions carried out at the same time, the number of foamed debris per year becomes 115 and all missions would be completed within 4.4 *years*. This list, contrary to the previous ones, presents a wide range of semi-major axis and inclination values, then much more propellant and time is needed to perform each removal mission.

Indeed, each mission on average performs a velocity increment on the order of 12 *km/s*. Most of the time is required to move from a debris to the next one and changing the specific thruster here assumed (or the power level) would reduce this time increasing the mission performance. In general, the electric thruster, the foam density, the initial platform orbit and its mass, the atmospheric model and the specific list considered are the fundamental factors resulting in these specific numbers. All in all, these cases represent average (and rather conservative) situations where the deorbiting platform is always able to deorbit at least some debris per year reducing the debris mass at least of 1 *ton/year*.

11 HAZARDS AND RISKS

After the foam characteristics analysis and their applications for deorbiting purposes, let us focus on the possible troubles arising in this approach. Some of the most critical phases to focus on, for the definition of hazards and risks of the foam-based deorbiting method, are the ground handling phase, the launch phase, the foam ejection phase and the deorbiting phase. Each of these phases presents its own issues and these have to be carefully faced to avoid any harm or injury and to have the highest probabilities of success for the mission.

In this section, starting from the previously stated assumptions and implementing few low order models, each phase is considered together with the steps that can be taken to reduce the associated risks. Obviously, since there are very few experiences of foam expansion in space, these considerations have to be intended as first guess efforts to describe the way to handle the problems related with this approach before, during and after the mission.

11.1 Ground Handling

Concerning the handling of components of polymeric foam, as identified in Sec. 5, it is reasonable to assume that there is not any additional hazard arising from the integration of these substances in the spacecraft or from the interaction with any part of the spacecraft.

The safety documents provided by the foam producer of the foam identified in Sec. 6 (ESPAK 90) are here used as reference for the identification of potential hazards related with the handling of the two components needed to generate such foams, polyol (A-component: *compounds with N-[3-(dimethylamino)propyl]tall-oil amides*) and diisocyanate (B-component: *Methylene diphenyl diisocyanate*) [116].

For handling and storage of both components, it is strongly recommended to avoid the contact of the substances with eyes and skin using appropriate protections as rubber gloves and protective glasses. It is also recommended to avoid for the B-component, that the local value of the vapour concentration exceeds the 0.005 mg/m^3. Both components have to be stored at a maximum temperature of 50 $°C$ while the temperature of the B-component must not reach temperature below 5 $°C$ (thus a thermal control system is mandatory). Both the components have to be dumped not into any sewers, or on the ground. They should be treated as hazardous waste according to the EC Directive 91/689/EEC [116] and to any national disposal practices governing hazardous waste. The transport of both components has to take place within the acceptable temperature range and away from foodstuffs, although it is absolutely considered not hazardous.

It is reasonable to assume that these specific values change form foam to foam, but the related hazards are easy to mitigate in similar fashions. Furthermore, in general, most polymeric foams do not present specific human hazards and they are quite easy to handle also in ground applications [61].

11.2 Launch

During the launch phase, a wide range of different mechanical and thermal stresses takes place. The storage of the two components listed in Sec. 11.1 inside the spacecraft, together with the accommodation of the spacecraft itself inside the launcher, has to be designed in such a way to constantly satisfy the storage temperature of the substances. It is also clear that any part of the foam components tank and of the foam distribution system has to tolerate all the forces acting on the spacecraft during this phase, avoiding any undesired contact between the two components (however assumed to flow in different circuits, see Sec. 9).

In case of accidental leakage in one of the foam feeding circuit, it is very likely that the contact between one component (A-component) and the on-board electronics could result in serious damages and consequently a spacecraft malfunctioning could occur. In the unlikely case of multiple failures and contact between the two components, the heat generated by the chemical reaction could damage some of the spacecraft subsystems strongly compromising the spacecraft operations and the whole mission. It is expected that neither the launcher nor any other (possibly present) payload will suffer from the loss of functionality of the deorbiting spacecraft considering that the foam generated by the accidental reaction of the two components will remain contained within the spacecraft and its structure, much more firm than the expanded foam, borders the reaction.

11.3 Foam Ejection

The ejection of the foam from the spacecraft through the foam nucleating system, see Sec. 9, is without any doubt the most critical part of the mission. During each step of this phase, see Sec. 1.3, a potential fault could occur leading to a wide range of possible consequences for the mission and for the spacecraft operations. In case the foam ejected from the spacecraft does not reach or it does not stick to the target debris, it will be very likely that it starts orbiting. The initial non-zero relative velocity of the foam with respect to the spacecraft causes this orbit to be different both from the one of the deorbiting spacecraft and the one of the target debris. This malfunctioning, however, does definitely not generate new significant orbital debris: the very high value of the area-to-mass ratio of these orbiting foam, causes its rapid descent even from high orbital region. By way of example, a small ball of foam of 0.1 *kg* of mass would deorbit from 900 *km* of altitude within 4 months and from 600 *km* in less than two weeks.

If during the foam ejection, the reaction is somehow prevented or stopped, the two components would start to flow out from the spacecraft representing potential hazards both for the spacecraft itself than for other orbiting objects. It is very important, for this reason, to continuously control the density and viscosity of the obtained foam both at the exit of the foam nucleating system and at some stages of the foam formation before its expansion outside the spacecraft. This could even result in a malfunctioning or blockage of the foam ejection device, so it is necessary to provide fault-tolerant designs and redundant components.

Some issues may also arise from a non-spherical distribution of the foam around the target debris. Actually, it is more likely to observe an asymmetrical shape for the foam around the target, given its possible complex shape and uncertain nature. For this reason, it is reasonable to assume that the spacecraft has to be provided with an autonomous system for the formation flying control with respect to the target, in order to cover, as much as possible, any side of the target with foam. It

should then wait for the foam expansion and then proceed again with its ejection to refine the geometry of the foam ball.

In case of malfunctioning of the foam nucleating system, it is reasonable to assume that the foam does not succeed to encompass the debris. The worst situation that can take place is the foam ejection only on a single debris surface. This event leads to a balloon-shaped debris composed of the actual debris and a foam ball attached to a single face only by a small quantity of foam, see Fig. 77. In order to assess the behaviour of the foam, it is worth analysing this worst (and very conservative) case scenario to understand what should be the minimum contact area between the foam and the debris.

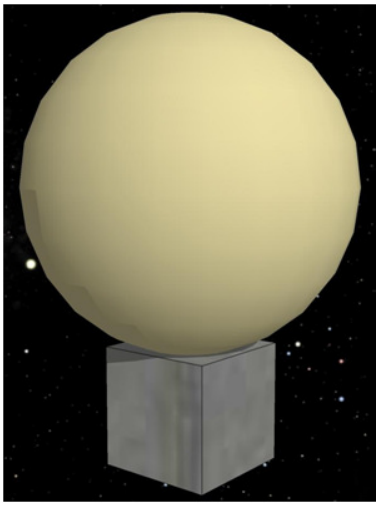

Figure 77: Artistic representation of a worst case result of a foam nucleating system malfunctioning.

Considering the previously described scenario, it is possible to schematize the foam and debris relative position as represented in Fig. 77. In this simplified configuration, the debris is considered as a cube (any other shape would not affect the following considerations) and the foam is completely expanded next to the debris with just a small quantity of foam acting as adhesive. In this situation it is very likely that, given the particular shape and the unbalanced mass distribution, the system happens to be in rapid rotation during the re-entry. Nevertheless, this scenario is here conservatively analysed considering the forces distribution shown in Fig. 78 as a worst case condition with respect to the resulting stresses at the foam-debris interface. Among the possible stress conditions, the one here represented is the one in which the cross sectional area is minimum with respect to the tension distribution.

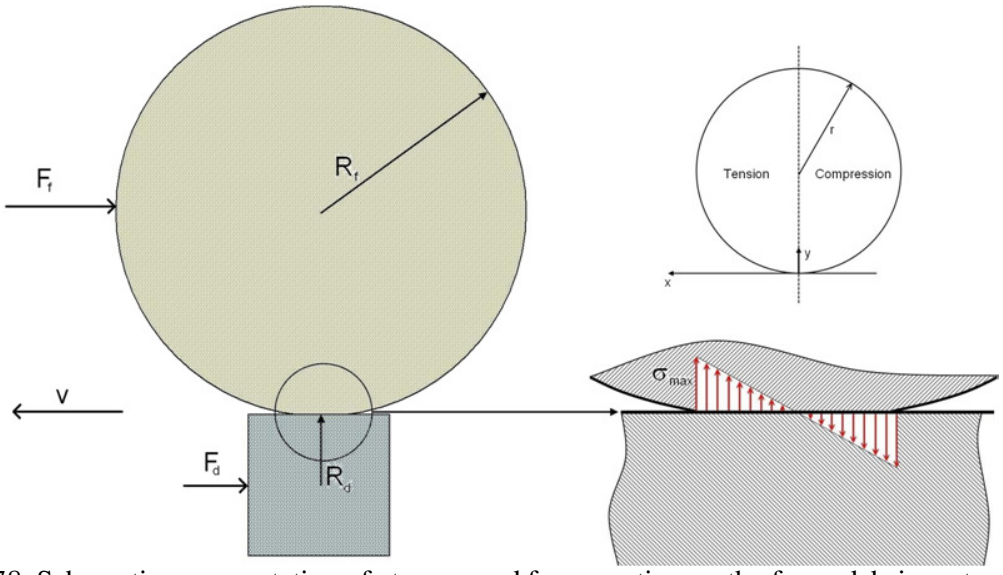

Figure 78: Schematic representation of stresses and forces acting on the foam-debris system at the materials interface. The forces shown on the left lead to the stress shown in the right plots.

As it is clear from Fig. 78, it has been considered that half of the contact surface is compressed by the moment acting on the system, and the rest of the region is oppositely loaded. This latter region is the one considered as critical for the strength of the bond. The torque acting on the system, causing bending moment, is due to the different atmospheric drag force acting on the two elements according to their different area-to-mass ratio.

To obtain the most conservative result for the described scenario, the system has been supposed to be on a 300 *km* altitude circular orbit. This orbit is, indeed, one with the highest value of the atmospheric density, and then the highest drag resistance force. Considering even that at lower altitudes the debris would, in case of separation from the foam ball, deorbit by itself in any case. For higher altitude values, the foam-debris system would definitely deorbit spinning as described before, since the forces acting on the system would be exponentially smaller.

Considering the nomenclature of Fig. 78, the bending moment, applied in the centre of the contact area, acting on the system is given by:

$$T = F_f R_f - F_d R_d \tag{46}$$

In order to assess the minimum contact area between the foam and the debris, the moment resulting on the system has to be related with the resulting stresses, supposed distributed as shown in Fig. 78. In the scheme of Fig. 78, stresses are assumed to grow linearly with the distance from the centre of the contact area, i.e. the *x* coordinate, up to the maximum allowable value, σ_{max}. The σ_{max} value has been obtained considering the tensile strength value of a commercial elastic polyurethane resin adhesive ($\bar{\sigma}$=2.5 N/mm^2) [117] and applying a pejorative factor ($k = 1000$) that would take into account the presence of voids and the non-perfect foam adhesion to the debris surface, so $\sigma_{max} = \bar{\sigma}/k$. Thus the actual tensile strength value here assumed is σ_{max} =2.5e-3 N/mm^2. Under these assumptions, the tension distribution, linear with the *x* coordinate shown in Fig. 78, is:

$$\sigma(x) = \frac{\sigma(r) - \sigma(0)}{r - 0} x = \frac{\sigma_{max} - 0}{r} x = \frac{\sigma_{max}}{r} x \tag{47}$$

It is now possible to identify the relationship between the radius of the foam–debris contact surface (r), and the moment due to the atmospheric drag forces acting on the two different parts of the system. This is done in order to size the minimum contact area. In particular, one half of the bending moment, T, has to be balanced by the integral of the tension distribution over one half of the contact area. Assuming a circular contact area, this relation can be analytically solved as follows:

$$\frac{T}{2} = \int_{A/2} \sigma(x)\, x dA = \iint_{A/2} \sigma(x)\, x dx dy = \iint_{A/2} \frac{\sigma_{max}}{r} x^2 dx dy = \int_0^r \frac{\sigma_{max}}{r} x^2 \sqrt{r^2 - x^2}\, dx = \sigma_{max} \frac{\pi r^4}{16} \tag{48}$$

Thus, solving with respect to the radius, the minimum acceptable r value is:

$$r = \sqrt[3]{\frac{8T}{\pi} \frac{1}{\sigma_{max}}} \tag{49}$$

At this point of the analysis, it is possible to use Eq.(49) with the optimum foam ball radius values obtained in Sec. 4. Considering the DISCOS list described in Sec. 3, three debris with the highest value of the foam ball-debris area ratio have been identified for the minimum, medium and maximum atmospheric drag model (see Figs. 25-27). The resulting bending moment has been evaluated for these three cases, and then the minimum value of the foam-debris contact area has been obtained by means of Eq.(49). The results of this analysis are described in Tab. 12.

Atmospheric density model	Minimum	Medium	Maximum
Debris Number	23	9	9
R_f [m]	7.83	4.43	4.38
A_f [m^2]	193.03	61.72	60.31
Area Ratio [-]	85.37	34.81	34.01
A_d [m^2]	2.26	1.77	1.77
R_d [m]	0.75	0.67	0,67
F_f [N]	0.10	0.08	0.15
F_d [mN]	1.19	2.22	2.52
T [Nm]	0.79	0.34	0.67
r [cm]	9.32	7.03	8.8
A [m^2]	0.027	0.016	0.024

Table 12: Bending moment and minima foam-debris contact area for debris with the highest value of the foam ball-debris area ratio in the three different atmospheric density scenarios.

The minimum radius of the contact area is always smaller than 15 *cm* for the three cases. For the sake of completeness, the debris considered for the minimum density case is not equal to the one of the other two cases (see debris number row in Tab. 12). For debris number 9, indeed, in the minimum density case the area ratio is slightly smaller (77.5) than the highest one (85.4), leading to a minimum radius value of 8.88 *cm*, instead of 9.32 *cm*.

All in all, this analysis shows that even in this very unlikely configuration the contact area is rather small and it can be reasonably realized also in case of foam nucleating device malfunctioning. Thus, the foam-based method, although with reduced performance, can work anyway.

11.4 Re-entry Behaviour

During the deorbiting phase the foam balls could definitely hit or be hit by other debris or even by still active spacecrafts and satellites. This non-negligible impact possibility is obviously due to their large exposed area. Impacts with active spacecrafts can be avoided simply tracking the foam ball as any other debris and, as the ball is not controlled during the re-entry, it will be care of the controllable satellites to avoid the impact. In case of impact trajectory between the foam ball and one or more orbital debris, the impact is most probably unavoidable but may still not be critical depending on their relative size.

Using again the NASA90 model described in Sec. 2, it is possible to estimate the debris impact flux for an hypothetical 7.5 *m* radius foam ball on a 900 *km* altitude circular orbit inclined at 110 *deg*. Considering 1 *mm*, 1 *cm* and 10 *cm* as minimum debris diameters, it is possible to estimate the total number of impacts per year for the given ball, being respectively 7.5, 0.03 and 9.9e-4. For a foam ball lifetime of 10 *years*, these values lead to a total number of impacts respectively of 75, 0.3 and 0.0099. None of these values is compliant with NASA Guidelines for Limiting Orbital Debris described in Sec. 3. The latter one, however, represents a very small number of potential impacts that do not result in catastrophic collisions. As a matter of fact, a collision with a space object larger than 10 *cm* in diameter could even end in an impact with the debris encompassed by the foam, potentially without generation of new debris that would in case remain encompassed by the foam, or in the separation of some foam from the foam ball. In this latter case, the foam debris resulting from this collision will deorbit in a small time due to their high area-to-mass ratio as described in Sec. 11.3.

Concerning impacts with objects smaller than 10 *cm* in diameter, given the peculiar property of porous solids as foams and aerogels, it is possible to consider that the behaviour of the foam ball during an impact event, will be similar to the one described for aerogels. Since 1995, aerogel and polyimide foam dust collectors have been developed for the intact capturing of micro debris on the Micro Particle Capturer on-board the Russian Service Module of the International Space Station [118]. Moreover the same material has been also used to develop the thermal insulator of the 2003 Mars Exploration Rovers [119].

Silica aerogels are highly porous solids and they are nowadays, the lowest density solids known. So far, they have been widely used in space due to their superior performances at capturing hypervelocity projectiles as already pointed out in Sec. 1. The primary effect of this low density material is to reduce the shock stress subsequent to impact in such a way that impacting objects survive the collision neither vaporizing nor melting [120].

In order to describe the behaviour of the foam ball during an impact event, an ad-hoc developed model is described in the following subsection.

11.4.1 IMPACT MODEL

Some simple estimates of the kinematics of these impacts have been performed since 1990 but the cratering process in such porous media is still not well understood. The feasibility of capturing hypervelocity projectiles using aerogels, together with the scaling of impact cavity dimensions [121,122,123] and the projectile track length inside aerogels [121] has been widely empirically studied. Accordingly, simple drag and ablation models have been used to describe the decrease in track length and capture projectiles size for high velocity impacts. Most of the examination of the track length and diameter did not succeed in obtaining a systematic correlation with the size of the projectile and its velocity [124]. Most recently, Dominguez et al. [125] proposed and tested a quantitative model of compaction driven impact cratering in porous solids mostly to reach a better understanding of the functioning of aerogel based impact detectors.

In this model [125], the impact between the hypervelocity projectile and the target is described as an initial shock pressure P_{shock} ($P_{shock} \approx \rho_t v_i^2$,with ρ_t the target density and v_i the impact velocity) that, due to the very low value of the target density, does not result in the destruction of the projectile. The high value of the projectile-to-target density ratio strongly influences this phenomenon consenting the projectile to slow and penetrate, losing energy and momentum and generating a shock wave within the medium.

The slowing of projectile in hydrocarbon foams has already been described by Trucano and Grady [126] who defined the hydrodynamic force, F_h, within an ideal porous medium as:

$$F_h = \frac{1}{2}\left(\frac{1+k}{2}\right)\rho_0 v^2 A \tag{50}$$

where ρ_0 is the medium density, A the impactor area and k the porous materials compressibility, defined as:

$$k = 1 - \frac{\rho_0}{\rho_1} \tag{51}$$

The two density values of Eq.(51) are respectively the density value of the uncompressed medium (ρ_0) and high density states (ρ_1) of porous solids leading, in the ideal case of infinite expansion, to a compressibility equal to one [127].

The compression reaction force, F_c, slowing down the projectile in the porous medium is given by [125]:

$$F_c = P_c A \tag{52}$$

where P_c represents the crushing pressure of the medium, and A is again the impactor area. This value can be expressed as function of the critical velocity for crushing v_c as [125]:

$$P_c = \frac{1}{2}\rho_0 v_c^2 \tag{53}$$

Thus, the projectile momentum decreases according to:

$$\frac{dp}{dx} = -\frac{1}{v}\left(F_h + F_c\right) = -\frac{C_d}{2}\rho_0 v_c^2 A - P_c A \tag{54}$$

where for the second equality Eqs.(50)-(53) have been exploited. Assuming that the radius of the incident projectile, subscript *p*) is constant for the entire path within the medium, Eq.(54) can be solved for the projectile velocity leading to :

$$v_p\left(x\right) = v_0 e^{-x/2\lambda}\left[1 + \frac{1}{C_d}\left(\frac{v_c}{v_0}\right)^2\left(1 - e^{x/\lambda}\right)\right]^{1/2} \tag{55}$$

where the term λ is given by:

$$\lambda = \frac{1}{C_d}\frac{4}{3}\frac{\rho_p}{\rho_0} r_p \tag{56}$$

Therefore, neglecting projectile erosion or material deposit on the projectile, the penetration depth can be obtained solving Eq.(55), i.e. integrating it in time [125]:

$$L_T = \lambda \ln\left(1 + \left(\frac{v_0}{v_c}\right)^2\right) = \frac{4 r_p}{3 C_d}\left(\frac{\rho_p}{\rho_0}\right)\ln\left(1 + \left(\frac{v_0}{v_c}\right)^2\right) \tag{57}$$

The projectile density found in Eq.(57) can be expressed as function of the projectile (assumed spherical) characteristic dimension, d_p, and its area-to-mass ratio $\left(A/m\right)_p$:

$$\rho_p = \frac{m_p}{V_p} = \frac{A_p}{\left(A/m\right)_p}\frac{1}{V_p} = \frac{\pi d_p^2}{4}\frac{1}{\left(A/m\right)_p}\frac{3}{4\pi}\frac{8}{d_p^3} = \frac{3}{2}\frac{1}{d_p\left(A/m\right)_p} \tag{58}$$

Exploiting Eq.(58), it is now possible to obtain a new form of Eq.(57):

$$L_T = \frac{4}{3}\frac{d_p}{2}\frac{1}{C_d}\left(\frac{3}{2}\frac{1}{d_p\left(A/m\right)_p}\frac{1}{\rho_0}\right)\ln\left(1 + \left(\frac{v_0}{v_c}\right)^2\right) = \frac{1}{C_d}\frac{1}{\left(A/m\right)_p}\frac{1}{\rho_0}\ln\left(1 + \left(\frac{v_0}{v_c}\right)^2\right) \tag{59}$$

The crushing velocity v_c can be obtained from the value of the crushing strength of the foam. This value can only be experimentally determined, so for the purpose of the present work we consider for the crushing strength value, P_c (*kPa*), the scaling law obtained for aerogels [125]:

$$P_c\left(\rho\right) \cong \left(\frac{\rho}{14}\right)^{2.04} 1e-3 \tag{60}$$

Applying this relation to Eq.(53), it is then possible to obtain:

$$v_c = \sqrt{\frac{2P_c}{\rho_0}} = \sqrt{\frac{2\cdot 10^3}{\rho_0}\left(\frac{\rho_0}{14}\right)^{2.04}} \tag{61}$$

The low order model described is used in the following section to assess the consequences of small debris impact with the foam ball. In particular, given the debris size and its impact energy, the possibility to reduce its velocity to zero within a foam ball diameter is addressed.

11.4.2 SMALL DEBRIS IMPACT

The probability of accidental collisions with debris smaller than 10 *cm* obtained in Sec. 11.4 gives a considerable total number of impacts for the entire life of the foam ball. These impacts have to be considered taking into account the population of small orbital debris and the characteristics expected for the foam identified in Sec. 7. The impact model described in Sec. 11.4.1 can now be used to assess the vulnerability of the foam-based method with respect to these impacts, as well as the capacity of the foam-based method to intercept several minor debris and drag them into the foam or stuck to its surface, as a sort of *domino effect*. In order to estimate these effects, and in particular this sort of additional cleaning process, a preliminary analysis of the population of small debris is carried out.

The debris population resulting from the collision of the *Cosmos 2251* and the *Iridium 33* satellites is here assumed as representative sample of the whole debris distribution. Observational data from the U.S. Space Surveillance Network on the collision fragments are available for debris with size larger than about 10 *cm* [128]. The NASA Breakup Model has been used in [128] to obtain, starting from the dry masses of the satellites, the number of fragments for different minimum sizes. Table 13 shows the number of fragments deriving from the collision with respect to their dimension.

	Catalogued fragments	**Estimated >10 cm**	**Estimated >1 cm**	**Estimated >1 mm**
Cosmos 2251	1142	840	43220	2.22e6
Iridium 33	490	580	30100	1.54e6
Sum	1632	1420	73320	3.76e6

Table 13: Number of catalogued and estimated fragments from *Iridium 33* and *Cosmos 2251* satellites. The projected quantities have been estimated using the NASA breakup model [128].

Each fragment resulted from the satellites breakup has its own energy and momentum, therefore a non-zero relative velocity with respect to the one of the satellite before the impact. Given the wide range of materials and shape of fragments, each element of the distribution has also its own area-to-mass ratio value.

A very similar analysis can be carried out also for a couple of other remarkable orbital impact events: the *Fengyun 1C* Chinese anti-satellite test of the 2007 and the *SOLWIND* anti-satellite test carried out by the United States Air Force in the 1985. In Fig. 79, the velocities of these fragmentation debris for the three collisions are shown with respect to their area-to-mass ratio.

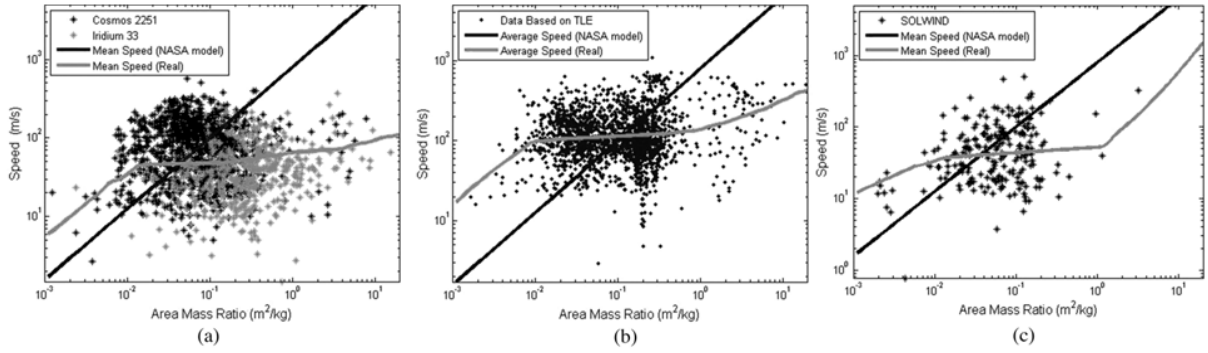

Figure 79: Area-to-mass ratio and relative speed values for the fragments distribution (a) *Cosmos 2251* and *Iridium 33* collision, (b) *Fengyun 1C* breakup and (c) *SOLWIND*.

Values reported in Fig. 79 only relate to the actual fragments data obtainable by radar observations. It is then necessary to assume for the small (not traceable) debris population, that the relative velocity and area-to-mass distribution are not dissimilar to the one of the debris larger than 10 *cm*.

It is now possible to use these values to assess the behaviour of a foam ball placed on the same orbit of one of the satellites involved in the collision, with respect to the impact with small fragments of given area-to-mass ratio and relative velocity. The density of the foam is assumed to be 1 kg/m^3 and the drag coefficient $C_d = 2$. The analysis pertains fragments with relative velocity ranging from 1 to 1000 *m/s* and area-to-mass ratios from 0.05 to 0.75.

11.4.3 RESULTS

In this section the impact model described in Sec. 11.4.1 is applied to small debris described in Sec. 11.4.2 and the results of this analysis are reported in Fig. 80. Each line in the plot represents the foam stopping capabilities for different values of the debris area-to-mass. The three horizontal lines in the plot at 5, 10 and 15 *m* represent three hypothetical thresholds for the size of a foam ball. It is then clear that a 5 *m* radius foam ball is capable of stopping all debris with an area-to-mass ratio from 0.5 to 0.75 regardless from their velocity, and all debris with an area-to-mass ratio of 0.25 and a relative velocity below 160 *m/s*. For even smaller values of the area-to-mass ratio, the maximum relative velocity value of the captured debris is 25 *m/s*.

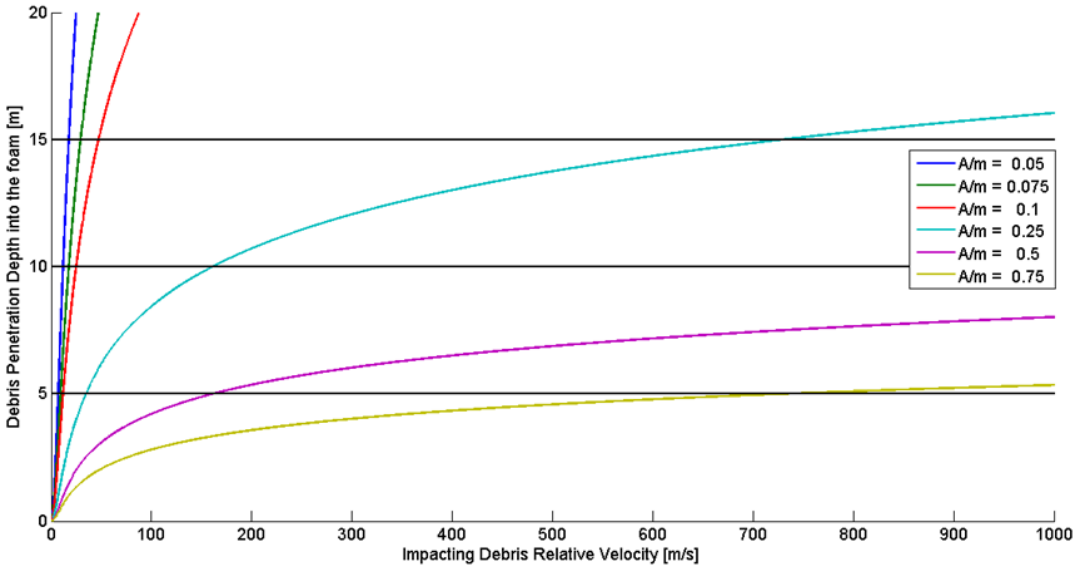

Figure 80: Impactors relative velocity vs. penetration depth for a range of different debris area-to-mass ratios. Three hypothetical thresholds for the debris path are highlighted with the horizontal lines.

It is worth recalling that these three threshold have to be compared with the ball diameter and all are compliant with the 10 *m* radius so for assumed. The results of this global analysis may be better understood if compared to the debris velocity and area-to-mass ratio distribution provided in Sec. 11.4.2.

Considering the previously listed thresholds, it is actually easy to identify the regions of the plots of Fig. 79 that may benefit from the *domino effect* described in Sect. 11.4.2. These regions represent indeed those debris which will be captured by the foam ball in case of direct collision.

Figure 81 shows that even with just 5 *m* of debris path within the foam ball, more than half of the debris resulting from the *Iridium 33* satellite (the grey dots) would be absorbed by the foam in case of collision without breaking the foam-ball structure. Considering a larger value of 15 *m* for the debris path, almost all debris of the *Iridium 33* satellite and half of the *Cosmos 2251* ones would be halted by the foam. An average value of 10 *m* still provides good results with most of the total debris captured and, thus, deorbited by a foam ball nucleated to target another (larger) debris.

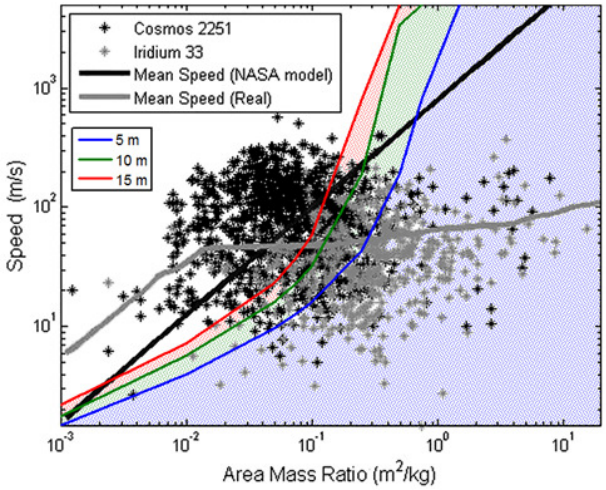

Figure 81: Fragments distribution from the *Cosmos 2251* and *Iridium 33* collision. The shadowed regions highlight the debris that could be captured by the foam ball for different values of the maximum debris path within the foam.

It is worth mentioning that the debris with the highest area-to-mass ratio values should deorbit by themselves in a rather short time, so they have even less probabilities to hit the foam ball with respect to the others. However, in case of impact of any of these with the foam, they would be captured and swept along with the foam ball.

Carrying out the same analysis also on the other two debris distributions shown in Fig. 79, Fig. 82 shows the fraction of fragments from the *Fengyun 1C* destruction captured thanks to the described *domino effect*.

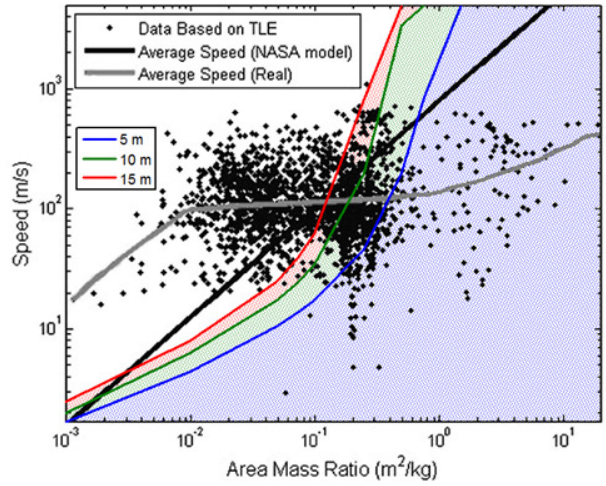

Figure 82: Fragments distribution from the *Fengyun 1C* destruction. The shadowed regions highlight the debris that could be captured by the foam ball for different values of the maximum debris path within the foam.

Observing the distribution of debris of Fig. 79(b), it is possible to note that most of fragments are situated in the left part of the plot, and then they have smaller area-to-mass ratio values if compared to the ones of the *Cosmos-Iridium* collision. This difference may be due to the different ways the two fragments populations originated (the *Fengyun 1C* destruction, indeed, was caused by a Chinese ballistic missile) or due to the time interval elapsed between the two events.

For this reason, it is clear from the plot of Fig. 82 that for 5 *m* of debris path, the number of captured fragments is not considerable as in the previous case. However, higher values of the path length give better results enabling the catching of almost half of the total debris population consequent to the *Fengyun 1C* destruction.

The *SOLWIND* breakup, finally, originated by a anti-satellite test carried out by the United States Air Force in the late 80s, has left in orbit just few debris since it took place and most of debris present relatively small area-to-mass ratios. This distribution can then be illustrative for what should happen to debris originated by the two events previously mentioned. Figure 83 shows the fraction of *SOLWIND* debris captured by a foam ball with respect to the ball radius.

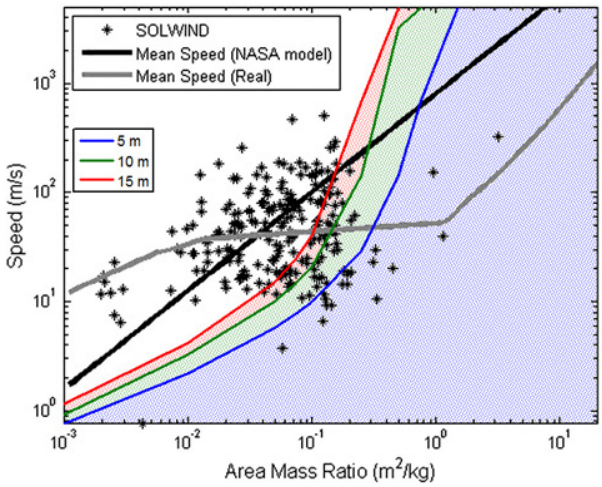

Figure 83: Fragments distribution from the *SOLWIND* destruction. The shadowed regions highlight the debris that could be captured by the foam ball for different values of the maximum debris path within the foam.

The very small population resulting from the *SOLWIND* destruction still orbiting, does not allow to highlight meaningful results. Also in this case it is possible to notice that the 5 *m* threshold is actually not an effective limit for the path length since the foam results to be able to capture more or less 10% of the total debris population. Nevertheless, in the other two cases almost 25%, 10 *m*, and nearly 33%, 15 *m*, of the remaining debris would, upon impact, be encompassed by the foam ball.

12 CONCLUSIONS

The expanding-encompassing-foam concept here proposed aims to augment the drag acceleration acting on a given debris such that an uncontrolled re-entry can take place with the complete burn up of the object in the atmosphere within a given time frame.

The specific foam kind is demonstrated to be the key aspect to assess the mission performance. Conservative analyses led to consider 1 kg/m^3 expanded foam density. This approach does not require any additional manoeuvre to be performed by the debris during the deorbiting lifetime (although these can be planned), and the foaming of a single debris do not requires any docking with it. The deorbiting duration remains the actual free choice to size the foam quantity to eject on the target debris. Such duration has been here addressed considering a good compromise with the impact probability, but it might be also sized considering a fixed deorbiting duration and/or additional constraints.

The foam nucleating and ejection system is here assumed to be a robotic arm equipped with a static mixing nozzle. This solution, based on the state of the art for industrial foaming processes, does not require any moving part and has been chosen among few other options.

The proposed platform is a 4.6 *tons* spacecraft to be launched in LEO or SSO by means of a medium-class launcher (like Soyuz). The electric propulsion system allows a significant propellant mass saving and a reasonable increment in the transfer times from a debris to the next. This scenario requires a large total impulse, thus the electric propulsion options can easily overcome chemical solutions. Coupling such a kind of foam with a 5 *kW* Hall effect thrusters allows complete mission assessments on different debris lists. No particular technological issues arose in the power and mass budgets assessment.

The performance demonstrated by the method in the proposed missions depends on the object lists, the space region they cover and the number of targets considered. In general, up to several tons debris can be deorbited with an average saving of the order of 80% of the original deorbiting time. Considering heavy debris, however, the foam mass required could even overcome the debris mass making this method not the preferred choice. At this point, a couple of remarks are mandatory. First of all the foam mass depends, besides on the foam density, on the ball radius. It has been computed, for each debris, as the minimum of the curve given by the sum of non-dimensional deorbiting time and impact probability (derived by the NASA90 model). In general, allowing a larger impact probability, the foam ball radius increases augmenting accordingly the foam mass, and the deorbiting time decreases. On the contrary, reducing the allowed impact probability and allowing a lower gain in the deorbiting time, the foam ball radius can be reduced, thus the foam mass decreases and even more massive debris can be targeted by this method. A second remark deals with the nature of such heavy debris. These are typically well tracked objects such as launcher upper stages or dead satellites. For these specific debris sets, ad-hoc single-target missions can be conceived due to their relatively low number and to the possibility of standard docking interfaces.

12.1 Development Roadmap

Concerning the technical feasibility for a 2025 timeframe of the proposed method requires a more detailed analysis both of method performance and relevant key aspects.

One of the first key tasks to realize in the near future is the development of one or more benchmark lists of debris. These lists, indeed, might represent a sort of test bed for active deorbiting methods and, in particular, for the foam-based one allowing the identification of the most suitable debris removal method with respect to debris physical and orbital characteristics.

The physical characteristics of the foam clearly represent driving factors for the method performance. So far, these characteristics have been here derived considering state of the art foams for ground-based applications. From a technological point of view, the improvement of the foam characteristics or, even better, the development of ad-hoc foams, represents an essential step in the development of the method. Since a foam with tailored physical characteristics may significantly enhance mission performance, its development is highly recommended. . As way forward, the candidate foam can be ground tested in vacuum facilities and, once in orbit, the only phase to take care of is its deposition on the debris.

This leads to the second main issue to address in order to have this concept working is the foam ejection. This process has to be carefully studied in order to have the debris surface covered as uniformly and spherically as possible. Several issues may arise during this phase, thus the foam ball nucleating system shall be studied in depth.

Once the candidate foam has been identified, a test campaign can be carried out in order to test the method in a relevant environment (e.g. vacuum, microgravity, UV radiation). Subsequently, a first possible demonstration mission over the next 15 *years* could be represented by a nanosatellite (e.g. a CubeSat), filled with this foam, able to deorbit itself. Thus it should just be equipped with a small foam reservoir, a static mixer and some crevices from where the foam can expand covering the CubeSat surface. As second step, a nano- or micro-satellite should be used to target and deorbit another debris, at least of the same size or mass. At this point the foaming strategy to cover another object should have been defined and tested in space.

BIBLIOGRAPHY

1. D. Wright, *Space Debris*, Physics Today, Volume 60, Issue 10, pp. 35-40, 2007
2. H. Klinkrad, *Monitoring Space-Efforts Made by European Countries*. International Colloquium on Europe and Space Debris, France, 2002
3. H. Klinkrad, P. Beltrami, R. Walker, C. Martin, H. Stokes, J. Wilkinson, H. Sdunnus, S. Hauptmann, *Update of the ESA Space Debris Mitigation Handbook*, 2002
4. URL:http://www.esa.int/esaMI/Space_Debris/SEMQQ8VPXPF_0.html
5. J. C. Liou, N. L. Johnson, *Instability of the Present LEO Satellite Populations*. Advances in Space Research, Volume41, Issue 7, pp. 1047-1056, 2008
6. J. C. Liou, N. L. Johnson, *A sensitivity study of the effectiveness of active debris removal in LEO*. Acta Astronautica, Volume64, Issue 2-3, pp. 236-243, 2008
7. B. Bastida, H. Krag, *Strategies for Active Removal in LEO*. 5th European Conference on Space Debris, Germany, 2009
8. H. Klinkrad, N. L. Johnson, *Space Debris environment remediation concepts*. 5th European Conference on Space Debris, Germany, 2009
9. D. J. Kessler, B. G. Cour-Palais, *Collision Frequency of Artificial Satellites: The Creation of a Debris Belt*. Journal of Geophysical Research, Volume 83, Number A6, pp. 2637-2646, 1978
10. D. J. Kessler, N. L. Johnson, J. C. Liou, M. Matney, *The Kessler Syndrome: Implications to Future Space Operations*. 33rd AAS Guidance and Control Conference, AAS 10-016, Colorado, 2010
11. D. McKnight, *Pay Me Now or Pay Me More Later: Start the Development of Active Orbital Debris Removal Now.* Advanced Maui Optical and Space Surveillance Technologies Conference, Hawaii, 2010
12. Nasa Standard (NASA-STD) 8719.14, *Handbook for limiting orbital debris*. Nasa-Handbook 8719.14, 2008
13. URL:http://www.esa.int/gsp/ACT/ariadna/Ariadna%20Projects/ARI_study_10-CfI.html
14. H. Krag, H. Klinkrad, T. Flohrer, E. Fletcher, N. Bobrinsky, *The European Space Surveillance System-Required Performance and Design Concepts*. 8th US/Russian Space Surveillance Workshop, Space Surveillance Detecting and Tracking Innovation, Hawaii 2010
15. S.P. McManus, F. C. Wessling, J. T. Matthews, D. N. Patek, K. Emoto, D. T. Howard, T. S. Price, *Production of Polyurethane Foams in Space: Gravitational and Vacuum Effects on Foam Formation*. Polymer Research in Microgravity. ACS Symposium series 793, 2001
16. I. Coccorullo, L. Di Maio, S. Montesano, L. Incarnato, *Theoretical and experimental study of foaming process with chain extended recycled PET*. eXPRESS Polymer Letters, Volume 3, Number 2, pp. 84-96, 2009
17. D. Vallado, *Fundamentals of Astrodynamics and Application*. Space Technology Library, 2nd edition, 2001
18. Von J. F. Encke, *Berliner Astronomisches Jahrbuch für 1857*. Gedruckt in der Druckerei der Königlichen Akademie der Wissenschaften. Ferd. Dümmler's Verlags-Buchhandlung, Berlin, 1854

19. T. Fukushima, J. Astron, *Generalization of Encke's Method and its Application to the Orbital and Rotational Motions of Celestial Objects*. Astronomical Journal, Volume 112, pp. 1263-1277, 1996
20. D. E. Gaylor, *Analysis of low thrust orbit transfers using the Lagrange planetary equations*. ASE 388P.2 Celestial Mechanics I Project, 2000
21. A. E. Roy, A. Hilger, *Orbital Motion*. Planetary and Space Science, Volume 37, Issue 5, pp. 631-631, 1988
22. W. Gander, W. Gautschi, *Adaptive Quadrature-Revisited*. BIT Numerical Mathematics, Volume 40, Number 1, pp. 84-101, 2000
23. D. Vallado, D. Finkleman, *A Critical Assessment of Satellite Drag and Atmospheric Density Modeling*. AAS/AIAA Astrodynamics Specialist Conference, Hawaii, 2008
24. A. C. Long, J. O. Cappellari Jr., C. E. Velez, A. J Fuchs, *Goddard Trajectory Determination System (GTDS) Mathematical Theory (Revision I)*. Goddard Space Flight Center: National Aeronautics and Space Administration, 1989
25. H. Klinkrad, *On the Use of Atmosphere Models in Re-Entry Predictions*. ESA Symposium Proceedings on Environment Modelling for Space-based Applications, pp. 287-298, 1996
26. U. Walter, *Astronautics*. Physics Textbook, Wiley-VCH, 2008
27. A. Tewari, *Atmospheric and Space Flight Dynamics: Modeling and Simulation with MATLAB® and Simulink®*. Birkhäuser Boston, 1st edition, 2007
28. B. J. Anderson, *Review of Meteoroids/Orbital Debris Environment*. NASA SSP 30425, Revision A, 1991
29. H. Sdunnus, P. Beltrami, H. Klinkrad, M. Matney, A. Nazarenko, P. Wegener *Comparison of debris flux models*. Advances in Space Research, Volume 34, Issue 5, pp. 1000-1005, 2004
30. N. Johnson, E. Christiansen, R. Reynolds, M. Matney, J. Zhang, P. Eichler, A. Jackson, *NASA/JSC Orbital Debris Models*. 2nd European Conference on Space Debris, Germany, 1997
31. S. Fukushige, Y. Akahoshi, Y. Kitazawa, T. Goka, *Comparison of Debris Environment Models; ORDEM 2000, MASTER 2001 and MASTER 2005*. IHI Engineering Review, Volume 40, Number 1, 2007
32. URL:http://www.spenvis.oma.be/help/background/metdeb/metdeb.html
33. R. Jehn, S. Vinals-Larruga, H. Klinkrad, *DISCOS-The European Space Debris database*. 44th International Astronautical Congress, Austria, 2003
34. *UCS satellite Database*. Union of Concerned Scientists, 2009 (URL:http://www.ucsusa.org/nuclear_weapons_and_global_security/space_weapons/technical_issues/ucs-satellite-database.html)
35. B. McCormick, *Collision probabilities in geosynchronous orbit and techniques to control the environment*, Advances in Space Research, Volume 6, Issue 7, pp. 119-126, 1986
36. M. Hechler, *Collisional probabilities at geosynchronous altitudes*. Advances in Space Research, Volume 5, Issue 2, pp. 45-57, 1985
37. J. N. Opiela, E. Hillary, D. O. Whitlock, M. Hennigan, *Debris Assessment Software Version 2.0 User's Guide*. NASA Lyndon B. Johnson Space Center, 2007
38. J. C. Liou, M. J. Martney, P. D. Anz-Meador, D. Kessler, M. Jansen, J. R. Theall, *The New NASA Orbital Debris Engineering Model ORDEM2000*, NASA/TP, 2002

39. J. R. Wertz, W. J. Larson, *Space Mission Analysis and Design*. 3rd edition, Microcosm, 1999
40. A. Kumar, R. K. Gupta, *Fundamentals of Polymer Engineering*. 2nd edition, Marcel Dekker, 2003
41. URL:http://www.getpacked.com.au/pdfs/Instapak%20Flagship%20brochure.pdf
42. Fire Fighting and Fire Protection Systems Standards, *Engineering Standard for Foam Generating and Proportioning Systems*, IPS-E-SF-140
43. M. Meier, *Non-metallic solid foams-a non-exhaustive overview*. Foam Group, Brandenburgische Technische Universität Cottbus, Germany
44. P. Bárczy, J. Szőke, B. M. Somosvári, P. Szirovicza, T. Bárczy, *FOCUS: Foam evolution and stability in microgravity*. Colloids and Surfaces A: Physicochemical and Engineering Aspects, In Press, Corrected Proof, 2011
45. URL:http://www.plasticsportalasia.net/wa/plasticsAP~en_GB/portal/show/common/plasticsportal_news/2006/06_494
46. M. K. Williams, E. S. Weiser, J. E. Fesmire, B. W. Grimsley, T. M. Smith, J. R. Brenner, G. L. Nelson, *Polyimide Foam Insulation Materials for Aerospace Vehicles and Spaceport Applications*. 41st Space Congress, Cape Canaveral, 2004
47. P. S. Schenker, L. F. Sword, A. J. Ganino, D. B. Bickler, G. S. Hickey, D. K. Brown, E. T. Baumgartner, L. H. Matthies, B. H. Wilcox, T. Balch, H. Aghazarian, M. S. Garrett, *Lightweight rovers for Mars science exploration and sample return*. Intelligent Robotics and Computer Vision XVI, Pennsylvania, 1997
48. D. E. Brownlee, P. Tsou, J. D. Anderson, M. S. Hanner, R. L. Newburn, Z. Sekanina, B. C. Clark, F. Hörz, M. E. Zolensky, J. Kissel, J. A. M. McDonnell, S. A. Sandford, A. J. Tuzzolino, *STARDUST: Comet and interstellar dust sample return mission*. Journal of Geophysical Research, Volume 108, Number 10, 2003
49. URL:http://stardust.jpl.nasa.gov/tech/aerogel.html
50. S. Lee, C. B. Park, N. S. Ramesh, *Polymeric Foams: Science and Technology*. Taylor & Francis Group, LLC, 2007
51. Steven Winter Associates, Inc., *Appropriate applications for open-cell and closed-cell foam insulation in residential construction*. Building System Consultants, 2008
52. J. Hurley, *A UK Market survey for foam glass*. The Waste and Resources Action Programme, 2003
53. URL:http://www3.imperial.ac.uk/materials/facilities/em/jsm5610lv
54. E. Kreidl, *Foam Glass*. The Glass Industry, pp. 304-318, 1942
55. D. Solomon, M. Ros, *Foamed Glass Manufacture*, U.S. Patent 5516351, 1996
56. L. Biasetto, *Functional Ceramic Foams from Preceramic Polymers*, Ph.D. Thesis, University of Bologna, University of Padova, 2005
57. URL:http://www.busytrade.com/products/213306/ceramic-foam-filter.html
58. D. Weaire, S. J. Cox, J. Banhart, *Methods and models of metallic foam fabrication*. 8th Conference on Composites Engineering, D. Hui, pp.977-978, 2001
59. V. C. Srivastava, K. L. Sahoo, *Processing, stabilization and applications of metallic foams. Art of science*. Materials Science-Poland, Volume 25, Number 3, 2007
60. A. Rabiei, A. T. O'Neill, B. P. S. Neville, *Processing and Development of a New High Strength Metal Foam Materials for Space Applications*. Materials Research Society Symposium Proceedings, Volume 851 pp. 517-526, 2005
61. D. A. Kantz, *Polymers*, 1998 (URL:http://www.chymist.com/Polymers.pdf)

62. R. M. Patel, P. Jain, B. Story, S. Chum, *Polyethylene: An Account of Scientific Discovery and Industrial Innovations*. Innovations in Industrial and Engineering Chemistry, pp. 71-102, 2008
63. W. J. Nauta, *Stabilisation of low density, closed cell polyethylene foam*. Thesis, University of Twente, 2000
64. *Styrene Polymers*. M. F. Herman, Encyclopedia of Polymer Science and Technology, 3rd edition, John Wiley & Sons, Volume 4, 2004
65. *Expanded Polystyrene*. Australian Urethane & Styrene, Technical Data
66. *Vinyl Chloride Polymers*. M. F. Herman, Encyclopedia of Polymer Science and Technology, 3rd edition, John Wiley & Sons, Volume 8, 2004
67. D. Eaves, *Polymer Foams: Trends in Use and Technology*. Rapra Technology, 2004
68. *Additives*. M. F. Herman, Encyclopedia of Polymer Science and Technology, 3rd edition, John Wiley & Sons, Volume 1, 2004
69. L. H. Sperling, *Introduction to Polymer Science*. John Wiley & Sons, 2006
70. G. M. Gladysz, K. K. Chawla, A. R. Boccaccini, *Syntactic and Composite Foams*. Journal of the Material Science, Volume 44, pp. 1425-1426, 2009
71. *Composite Foams*. M. F. Herman, Encyclopedia of Polymer Science and Technology, 3rd edition, John Wiley & Sons, Volume 9, 2004
72. C. Gruau, *Metric generation for anisotropic mesh adaption with numerical applications to material forming simulation*. Ph. D. Thesis, L'école Nationale Supérieure des Mines de Paris, 2004
73. J. Bruchon, *Etude de la formation d'une structure de mousse par simulation directe de l'expansion de bulles dans une matrice liquide polymère*. Thesis, L'école Nationale Supérieure des Mines de Paris, 2004
74. K. A. Brakke, *The Surface Evolver*. Experimental Mathematics, Volume 1, Number 2, pp. 141-165, 1992
75. R. Valette, B. Vergnes, T. Coupez, *Multiscale simulation of mixing processes using 3D-parallel, fluid-structure interaction techniques*. International Journal of Material Forming, Volume 1, pp. 1131-1134, 2008
76. J. Bruchon, T. Coupez, *A numerical strategy for the direct 3D simulation of the expansion of bubbles into a molten polymer during a foaming process*. International Journal for Numerical Method in Fluids, Volume 57, Number 8, pp. 977-1003, 2008
77. J. Kizito, R. Balasubramaniam, H. Nahra, J. Agui, D. Truong, *Vapor-Gas Bubble Evolution and Growth in Extremely Viscous Fluids Under Vacuum* NASA/TM-215606, 2009
78. C. E. Brennen, *Bubble growth and collapse*. Fundamentals of Multiphase Flow, Cambridge University Press, 2005
79. S. L. Everitt, O. G. Harlen, H. J. Wilson, D. J. Read, *Bubble dynamics in viscoelastic fluids with application to reacting and non-reacting polymer foams*. Journal of Non-Newtonian Fluid Mechanics, Volume 114, pp. 83-107, 2003
80. J. Bikard, T. Coupez, *Simulation of bread making process using a direct 3D numerical method at microscale: Analysis of foaming phase during proofing*. Journal of Food Engineering, Volume 85, Issue 2, pp. 259-267, 2008
81. L. W. Schwartz, R. V. Roy, *A mathematical model for an expanding foam*. Journal of Colloid and Interface Science, Volume 264, pp. 237-249, 2002

82. J. E. Mark, *Physical properties of polymers handbook*. Springer Science, 2nd edition, 2007
83. L. Jourquin, E. DuPrez, R. Mortelmans, *Method for the manufacture of flexible polyurethane foam*. U.S. Patent 5194453, 1993
84. URL:http://www.prochima.it/pages/res_poliure.htm#RP-491
85. J. P. Downey, J. A. Pojman, *Polymer Research in Microgravity*. ACS Symposium series 793, 2001
86. G. W. Horgan, *Mathematical morphology for soil image analysis*. European Journal of Soil Science, Volume 49, Issue 2, pp.161-173, 1998
87. D. Klempner, V. Sendijarevic, R. Mikhaĭlovna Aseeva, *Handbook of polymeric foams and foam technology*. Hanser Gardner Publications, 2004
88. D. Gerald, C. Jean, *Open celled low density foam and method of making such an open celled foam*. U.S. Patent 5900440, 1999
89. C. M. Lisse, A. F. Cheng, N. L.Chabot, N. Dello Russo, J. H. Satcher, M. E. Zolensky, M. J. Cintala, D. P. Glavin, S. A. Sandford, *Development of Improved Aerogels for Spacecraft Hypervelocity Capture*. 39th Lunar and Planetary Science Conference, 2008
90. URL:http://www.masterbond.com/wbarticles/wbuv.html
91. Basotect UL, BASF Safety data sheet, 2011
92. D. Schmitt, L. Laurent, *Launch vehicles in service or in development, Ariane 5—Program status*. Acta Astronautica, Volume 66, Issues 5-6, pp. 871-882, 2010
93. *Ariane 5 User's Manual*. Arianespace, Issue 5, 2008
94. *Soyuz from the Guiana Space Centre User's Manual*. Arianespace, Issue 1, 2006
95. *Vega User's Manual*. Arianespace, Issue 3, 2006
96. R. G. Jahn, *Physics of Electric propulsion* McGraw-Hill, 1968
97. R. G. Jahn, E. Y. Choueiri, *Electric Propulsion*. Encyclopedia of Physical Science and Technology, 3rd Edition, Volume 5, 2002
98. C. R. Koppel, O. Duchemin, D. Valentian, *High Power Electric Propulsion System for Nep*. 1st Symposium on Potentially Disruptive Technologies And Their Impact in Space Programs, France, 2005
99. I. J. E. Jordan, *Electric Propulsion: Which One For My Spacecraft?*. Space Systems I course at JHU, Whiting School of Engineering, 2000
100. G. Saccoccia, J. Gonzalez del Amo, D. Estublier, *Electric Propulsion: A Key Technology for Space Missions in the New Millennium*, ESA bulletin, 2000
101. D. Estublier, G. Saccoccia, J. Gonzales Del Amo, *Electric propulsion on SMART-1 - a technology milestone*. ESA Bulletin, Number 129, pp. 40-46, 2007
102. O. Duchemin, P. Dumazert, D. Estublier, F. Darnon, *Testing the PPSX000 Plasma Thruster at high discharge voltage*. 4th Spacecraft Propulsion Conference, Italy, 2004
103. F. Darnon, D. Arrat, E. Chesta, S. d'Escrivan, N. Pillet, *Overview of Electric Propulsion Activities in France*. 29th International Electric Propulsion Conference, Princeton University, 2005
104. A. J. Petro, D. L. Talent, *Removal of Orbital Debris*. Progress in Astronautics and Aeronautics, Volume 121, pp. 169-182, 1989
105. G. Visentin, *Space Robotics*, Climbing and Walking Robots, Proceedings of the 8th International Conference on Climbing and Walking Robots and the Support Technologies for Mobile Machines, pp. 27-37, 2006

106. C. Contant-Jorgenson, P. Lála, K. Schrogl, *Space Traffic Management*. International Academy of Astronautics (IAA), 2006
107. M. A. Minor, C. R. Hirschi, R. O. Ambrose, *An Automated Tether Management System for Microgravity Extravehicular Activities*. IEEE Conference on Robotics and Automation, Washington, Volume 3, pp. 2289-95, 2002
108. URL:http://www.stamixco.com/index.php
109. URL:http://www.istc.illinois.edu/info/library_docs/manuals/coatings/appltech.htm#General%20Description%205
110. E. L. Paul, V. A. Atiemo-Obeng, S. M. Kresta, A. W. Etchells III, C. F. Meyer, *Mixing in Pipelines*. Handbook of Industrial Mixing: Science and Practice, 2004
111. B. A. Finlayson, *Use of Comsol Multiphysics in Undergraduate Research Projects to Solve Real-life Problems*. 2007 American Institute of Chemical Engineers, Utah, 2007
112. URL:http://www.comsol.com/products/multiphysics/
113. S. Hirschberg, R. Koubek, F. Moserc, J. Schöckd, *An improvement of the Sulzer SMX static mixer significantly reducing the pressure drop*. 13rd European Conference on Mixing, England, 2009
114. T. N. Edelbaum, *Propulsion Requirements for Controllable Satellites,* ARS Journal, pp. 1079-89, 1961
115. J. E. Pollard, *Simplified Analysis of Low-Thrust Orbital Maneuvers*. The Aerospace Corporation, 2000
116. ESPAK, Prochima Safety data sheet, 2008
117. SikaBond T2, SIKA Technical data sheet, 2001
118. Y. Kitazawa, A. Fujikawa, T. Kadono, T. Noguchi, R. Yamanaka, Y. Kimoto, M. Suzuki, *Overview of MPAC Experiment–development of dust collectors, hypervelocity impact experiment and post flight analysis*. International Symposium on "SM/MPCA&SEED Experiment", Japan, 2008
119. S. M. Jones, *Aerogel space exploration application*. Journal of Sol-Gel Science and Technology, Volume 40, Numbers 2-3, pp. 351-357, 2006
120. J. Trigo-Rodriguez, G. Domìnguez, M. J. Burchell, F. Hörz, J. Llorca, *Bulbous tracks arising from hypervelocity capture in aerogel*. Meteoritics & Planetary Science, Volume 43, Issue 1-2, pp. 75-86, 2008
121. R. A. Barrett, M. E. Zolensky, F. Hörz, D. J. Lindstrom, E. K. Gibson, *Suitability of silica aerogel as a capture medium for interplanetary dust*. Proceedings of the Lunar and Planetary Science Conference, pp. 203-212, 1992
122. M. J. Burchell, J. A. Creighton, M J, Cole, J. Mann, A. T. Kearsley, *Capture of particles in hypervelocity impacts in aerogel*. Meteoritics and Planetary Science, Volume 36, pp.209-221, 2001
123. M. J. Burchell, R. Thomson, H. Yano, *Capture of particles in hypervelocity impacts in aerogel: in ground laboraty and low Earth orbit*. Planetary and Space Science, Volume 47, pp.189-204, 1999
124. F. Horz, M. E. Zolensky, R. Bernhard, T. See, J. Warren, *Impact features and projectile residues in aerogel exposed on Mir*. *Icarus147*, pp.559-579, 2000
125. G. Dominguez, A. J. Whestpal, S. M. Jones, M. L. F. Phillips, *Energy loss and impact cratering in aerogels: theory and experiment*. Elsevier Inc., 2004
126. T. Trucano, D. Grady, *Impact Shock and Penetration Fragmentation in Porous Media*. Hypervelocity Impact Symposium, Santa Fe, 1994

127. Y. B. Zel'dovich, R. P. Yu, *The Physics of Shock Waves and High Temperature Hydrodynamic Phenomena*, Academy Press, New York, Volume 2, 1967
128. T. Wang, *Analysis of Debris from the Collision of the Cosmos 2251 and the Iridium 33 Satellites*. Science & Global Security, 2010

INDEX OF FIGURES

INDEX OF TABLES